Stony Brook University

Diffuse Correlation and Optical Spectroscopies for the Monitoring of Spinal Cord Hemodynamics

A Dissertation Presented

by

Angela Sofia Kogler

to

The Graduate School

in Partial Fulfillment of the

Requirements

for the Degree of

Doctor of Philosophy

in

Biomedical Engineering

Stony Brook University

May 2016

Stony Brook University

The Graduate School

Angela Sofia Kogler

We, the dissertation committee for the above candidate for the

Doctor of Philosophy degree, hereby recommend

acceptance of this dissertation.

Thomas F. Floyd, MD – Dissertation Advisor
Professor, Department of Anesthesiology

Yingtian Pan, Ph.D - Chairperson of Defense
Professor, Department of Biomedical Engineering

Wei Lin, Ph.D – Committee Member
Associate Professor, Department of Biomedical Engineering

Arjun Yodh, Ph.D – External Committee Member
Professor, Department of Physics and Astronomy, University of Pennsylvania

This dissertation is accepted by the Graduate School

Charles Taber
Dean of the Graduate School

Abstract of the Dissertation

Diffuse Correlation and Optical Spectroscopies for the Monitoring of Spinal Cord Hemodynamics

by

Angela Sofia Kogler

Doctor of Philosophy

in

Biomedical Engineering

Stony Brook University

2016

Spinal cord ischemia, caused by a prolonged loss of blood flow to the spinal cord, can occur as a result of direct trauma to the spinal cord or as a complication of major vascular, spine and spinal cord surgery, and surgeries for the stabilization of spinal cord trauma, often resulting in partial or complete paresis/paralysis. Current electrophysiological methods employed to detect spinal cord ischemia, namely somatosensory and motor evoked potentials, are indirect, temporally insensitive, nonspecific, and cumbersome. There is no technology currently available that can directly and immediately detect the onset of spinal cord ischemia, nor provide immediate feedback on the efficacy of interventions aimed at ameliorating spinal ischemia by improving flow and oxygen delivery.

The goal of this dissertation involves the development of a prototypical optical device, based on the principles of Diffuse Correlation Spectroscopy (DCS) and Diffuse Optical Spectroscopy (DOS), that would allow for the immediate detection and continuous monitoring of changes in spinal cord blood flow and oxygenation and testing it in a sheep model. DCS and DOS are diffuse optical techniques that utilize near-infrared light to continuously measure changes in blood flow and oxyhemoglobin/ deoxyhemoglobin concentrations respectively. A thin, flexible fiber optic probe was designed to enable minimally invasive percutaneous placement on to the sheep spinal cord. A series of proof-of-concept experiments tested and proved the hypothesis that the optical device would indeed detect changes in spinal cord blood flow and oxygenation, induced both pharmacologically and mechanically. Since DCS is a relatively novel technique, the blood flow changes detected by DCS were correlated with changes detected by an established method of blood flow measurement, isotope-labeled microspheres and a relatively good correlation was observed. The safety associated with the fiber optic probe, in terms of placement and laser heating, was evaluated through neurological monitoring of the sheep and histological assessment of spinal cord tissue. The hypothesis that the optical device could detect spinal cord ischemia earlier than evoked potential monitoring was tested by simultaneously comparing the time taken by the two technologies to detect a loss in blood flow upon aortic occlusion. This monitoring tool potentially represents an important step forward, offering a new level of accuracy and immediacy that could assist surgeons in pre-surgical planning, in intraoperative detection of spinal cord ischemia, and in postoperative monitoring in the cardiothoracic and neurological critical care settings.

Table of Contents

List of Figures

List of Tables

Acknowledgments

The text of this dissertation in part is a reprint of the materials as it appears in “Fiber-optic Monitoring of Spinal Cord Hemodynamics” by Angela Kogler et al., *Anesthesiology,* 2015. The co-authors listed in the publications directed and supervised the research that forms the basis for this thesis or dissertation.

Throughout my PhD research, I have received tremendous support from many people and would like to express my gratitude for their contributions towards my research and my graduate student career.

My sincerest thanks to my advisor and mentor, Dr. Thomas Floyd, without whose guidance and advice my research accomplishments would not have been possible. Through his mentorship, he has taught me to think critically and from the perspective of a physician as well as an engineer. He has fostered my confidence to take more of a leadership role with my experiments and pushed me to exceed my expectations of what I am capable of. For his generosity and guidance with my research, I will be forever grateful.

As Dr. Floyd provided me a great basis for the understanding of the medical relevance of this research, my transition into the field of diffuse optics would not have been nearly as rewarding without the help and advice I have received from Arjun Yodh and Rickson Mesquita at the University of Pennsylvania. I would like to thank Dr. Yodh for providing me unlimited access to the resources available in his lab - both in terms of seeking advice from his graduate and postdoctoral students, as well as the vast of amount of information I have learned about Diffuse Optical theory and instrumentation. My visits to his lab were crucial in providing me with the skills I needed to build the optical monitor we have used in our experiments at Stony Brook and in understanding diffuse optical principles.

Rickson Mesquita, formerly a postdoc in Arjun Yodh's lab at the University of Pennsylvania and currently an Assistant Professor at the University of Campinas in Brazil, has provided me with his invaluable knowledge of diffuse optics and helped me every step of the way. He has been my go-to person whenever I needed clarification or help with optics and I would like to thank him for his guidance and friendship through this journey.

I would like to thank Yingtian Pan, Professor of Biomedical Engineering at Stony Brook, for chairing my PhD committee and providing me with his valuable advice throughout my dissertation research.

Thanks to Wei Lin, Associate Professor of Biomedical Engineering, for advising me with my dissertation research as a committee member and for assisting with the real-time monitoring applications of our optical monitor.

I would be remiss if I didn't thank our collaborators at Stony Brook. My thanks to Dr. Thomas Bilfinger, Dr. Robert Galler and Dr. James Barsi for taking time off from their busy schedules and assisting us with our sheep surgeries. Their collaboration and surgical expertise has been critical to this research.

Thanks to the veterinary technicians at the Division of Laboratory Animal Resources (DLAR) at Stony Brook University: Nicole Motta, Joan Pashinsky and Jean Rooney, who have assisted us with the experimental set up and monitoring of the sheep. Thanks to Cecille Just, an Electroencephalography Technician at Stony Brook University, who assisted us with the collection of the neuromonitoring data. Thanks to John Tuominen for helping us set up this collaboration. We are thankful to Dr. James Davis, a histopathologist at Stony Brook University Hospital, who has provided us with his expertise in the histological analysis of the spinal cord tissue samples. Thanks to the Research Histology Core for processing and fixing our spinal cord tissue samples for histology. I would also like to thank Steven Schenkel and Meeri Kim, who work in Dr. Yodh's lab at the University of Pennsylvania - Steven, for assisting us with our initial sheep experiments and Meeri, for helping me understand the instrumentation of the optical monitor.

Last but certainly not least, I would like to acknowledge my family for providing me with their unconditional support and encouragement throughout my life and my graduate career. My parents and sisters who have always been there for me and made my education possible, and my in-laws for being my second family on Long Island. My husband Adam has been by my side for most of my PhD study, and without his patience, love, and support, the process would have been far more difficult. And to my newborn son, Ian, who has brought me so much joy, I dedicate this work and all of my future endeavors. My graduate career has been educational and fulfilling, and for all the people who have contributed towards it, my deepest gratitude.

Chapter 1

Introduction

The main objective of the research described in this dissertation was to develop a novel optical monitor and fiber-optic probe, based on the principles of Diffuse Correlation Spectroscopy (DCS) and Diffuse Optical Spectroscopy (DOS), that would be capable of detecting the blood flow and oxygenation concentration of the spinal cord. The ability of the device to detect immediate spinal cord blood flow and oxygenation changes was tested in sheep model. This chapter will elaborate on the need for the monitoring of spinal cord hemodynamics and its clinical relevance. While there is no tool available for directly and accurately monitoring spinal cord blood flow and oxygenation, other methods have been used in the operating room and in research that monitor spinal cord integrity. This chapter will provide an overview of the technique that is currently the gold standard in monitoring spinal cord integrity in the operating room, i.e. evoked potential monitoring, and other methods that are being researched for monitoring of spinal cord hemodynamics. Lastly, an introduction into diffuse optical monitoring methods and the various applications in which they have/are being currently used will be provided.

1.1. Need for monitoring of spinal cord hemodynamics

Spinal cord trauma, which can result from motor vehicle accidents, falls, violence, and sports-related injuries, is a global problem. The rates of spinal cord injuries vary from 12-60 cases per million individuals (*2-5*), with annual costs in the United States approaching $10,000,000,000/yr. The frequency of spinal cord ischemia as a complication after descending thoracic and thoracoabdominal aortic aneurysm repair remains intolerably high (*6, 7*), in spite of options for stenting (*8*), staged repair (*9*), distal perfusion (*10*), collateral vessel re-implantation (*11*), and CSF drainage (*12*). Secondary neurological injuries can also occur as a complication of surgeries involving vascular procedures (*13, 14*), spinal cord tumor resection (*15*), and correction of spinal cord deformities such as scoliosis (*16-21*). The quality of life and financial issues related to long-term care are daunting (*22-24*). Thus, development of tools for *in-situ* assessment of spinal cord ischemia is desirable.

The initial spinal cord injury (SCI) may be propagated by local and systemic factors such as neurogenic shock, vasospasm, inflammation, edema, hemorrhage, hypoxia and hypotension (*25*). Figure 1.1 below provides a brief summary of the underlying mechanism of spinal cord injury. Spinal ischemia can be prevented by monitoring for the initial ischemic event, and then limited by preventing secondary ischemia.

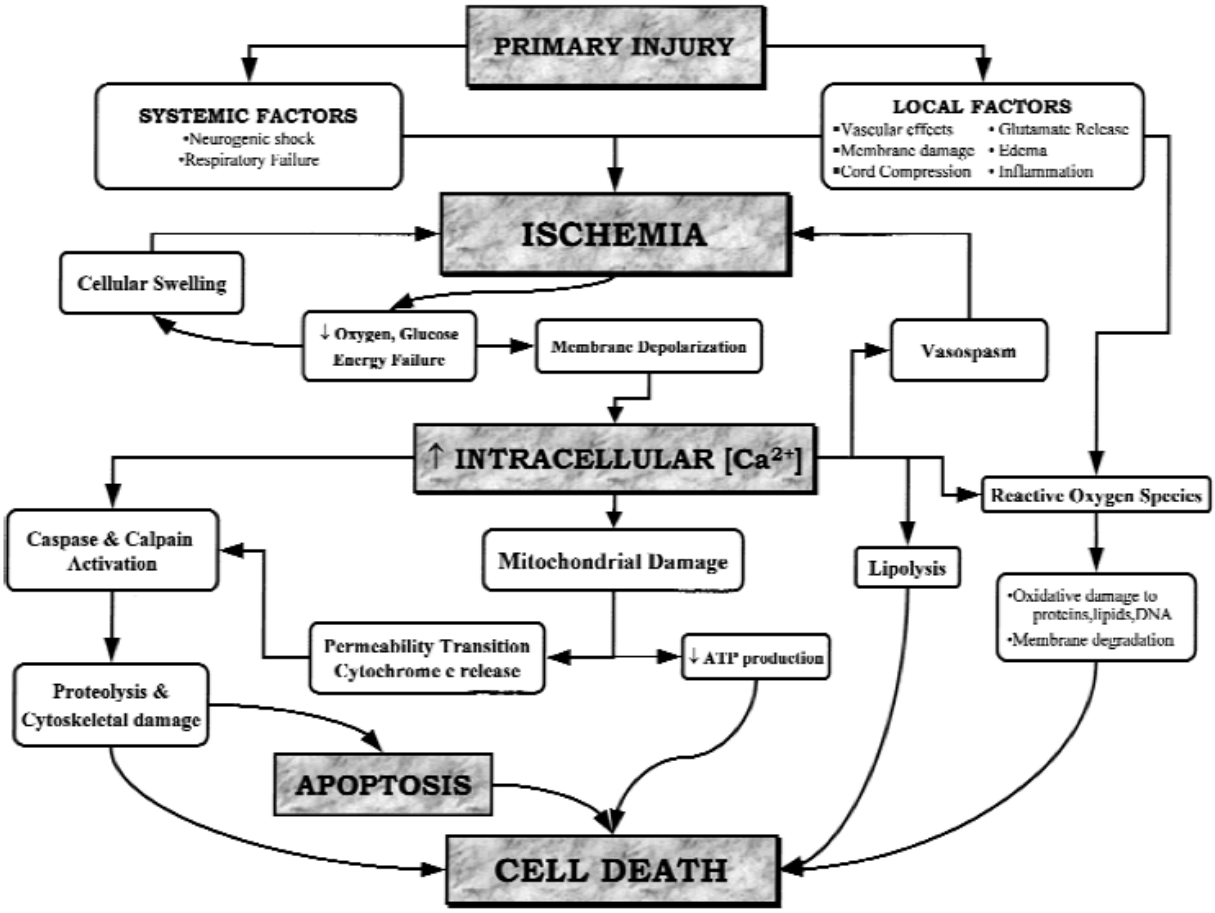

Figure 1.1: Schematic showing the mechanism underlying secondary injury after spinal cord trauma (Dumont et al (*26*))

Sixty-five percent of those who present with SCI can have salvageable function with timely and proper intervention (*27*), as only 35% of all SCIs are complete. Prevention of secondary injury to the spinal cord is critical to limit patient disability. Preventing secondary injury to the spinal cord, as with the brain, requires continued hemodynamic support and often, early surgical intervention (*28-30*). Preservation or restoration of spinal cord blood flow and oxygenation are the primary modalities used to prevent the onset of secondary injury (*31, 32*). However, there is no method currently available to

monitor the effects of interventions aimed at ameliorating spinal ischemia on blood flow and oxygenation. Spinal cord injury is associated with a marked decrease in life expectancy (*33, 34*), and a marked loss of quality of life and disability (*35, 36*). Long-term care costs related to these injuries are staggering (*37, 38*).

Major vascular surgeries such as descending thoracic and thoracoabdominal aortic aneurysm (TAAA) repairs require clamping of the descending aorta. Clamping over prolonged periods of time could lead to spinal ischemia or infarction in 8-28% of the cases (*39, 40*), and paralysis or paresis in 4-21% (*41*). Intra-aortic stent-grafting (closed repair) has advantages over open repair since it doesn't require aortic cross clamping or re-implantation of segmental arteries, but still results in perioperative spinal cord ischemia in 3-12% as critical vessels from the aorta which feed the spinal cord are covered (*42-46*). Spinal cord injury during open or closed aortic repairs largely depends on the extent of the aneurysm resected or covered and the existence of a collateral blood supply outside the aneurysm to the spinal cord (*47-49*).

Surgical techniques employed to protect the spinal cord include re-implantation of segmental arteries (*50*), epidural cooling (*49*), CSF drainage (*51*), and pharmacological interventions aimed at increasing mean arterial pressure. Although CSF drainage has shown promise in reducing the risk of ischemia induced paraplegia during the repair of types 1 and 2 TAAAs by increasing the spinal cord perfusion pressure (SCPP) (*52, 53*), no clinical studies show its effect on types 3 and 4 TAAAs (*54*). CSF drainage has been shown to decrease the incidence of paraplegia during open repairs (*55*); however, its

effect in an endovascular repair setting is yet to be determined. Since there is no device currently available to directly monitor spinal cord blood flow and oxygenation, the impact of surgical interventions upon spinal cord blood flow cannot be known in a clinically relevant time frame (*56*).

In spine stabilization surgery for trauma or for repair of congenital or acquired disorders, injury occurs from both ischemia and mechanical stretch of nerve fibers (*57, 58*). Ischemic injury occurs earlier than mechanical injury, and again, there is no monitor available to directly monitor for ischemia.

Figure 1.2 below summarizes the various applications where neuromonitoring for spinal cord ischemia can be useful in preventing post-surgical paralysis. Some examples are spinal cord tumor resection surgeries, surgeries for the stabilization of spinal cord trauma, surgeries for the correction of scoliosis and thoracic aortic aneurysm surgeries.

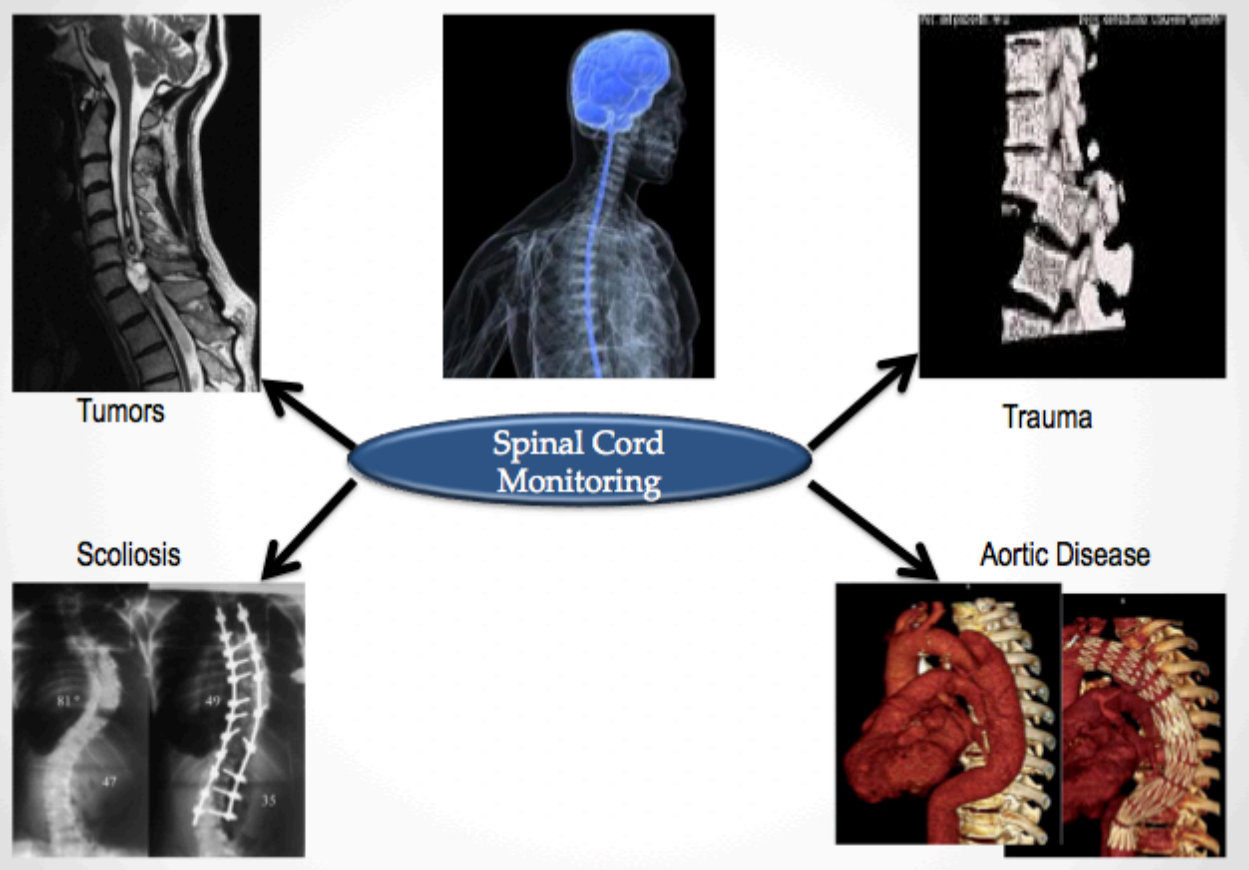

Figure 1.2: Some applications where neuromonitoring for spinal cord ischemia could be used: surgeries for spinal cord tumor resection, stabilization of spinal cord trauma, correction of scoliosis and treatment of thoracic aortic aneurysms.

1.2. Current techniques for monitoring of spinal cord ischemia

Current methods available for the monitoring and assessment of spinal cord ischemia are based upon neuroelectrophysiological techniques such as somatosensory and motor evoked potentials (SSEP, MEP) (*59-62*). While SSEPs monitor the

functional integrity of posterior spinal sensory pathways, MEPs monitor the integrity of anterior and lateral spinal motor tracts (*63*). And while the combination of SSEP and MEP can help identify spinal injury as well as provide information on the impact of interventions (*64, 65*), they have their disadvantages. In addition to spinal cord ischemia, evoked potentials can be influenced by the anesthetic used (*66, 67*), mechanical mechanisms, patient temperature (*68*), and limb ischemia. Furthermore, the technology cannot discriminate between the different factors that may influence the signal integrity, making correcting the signal problematic. "False negatives", where patients awaken with important deficits in spite of "normal" evoked potentials, as well as "false positives", where patients have awakened without deficits in spite of loss or degradation of signal, have been reported with both SSEP (*69*) and MEP (*70*) monitoring, even when used in a complimentary fashion (*71*).

Since MEPs use trans-cranial electrical stimulation, they can only be used in heavily sedated patients due to the pain associated with the stimuli. While SSEPs can be performed in awake patients, the electrical stimulation is still painful. Evoked potentials have also been documented to be temporally insensitive relative to the inciting event in certain cases (*50, 72, 73*), with the delayed signal often costing the surgeon valuable time in rescuing the threatened spinal tissue. Figure 1.3 shows an example of a case where there was an approximately twenty minute delay in the loss of MEP and SSEP signal amplitude.

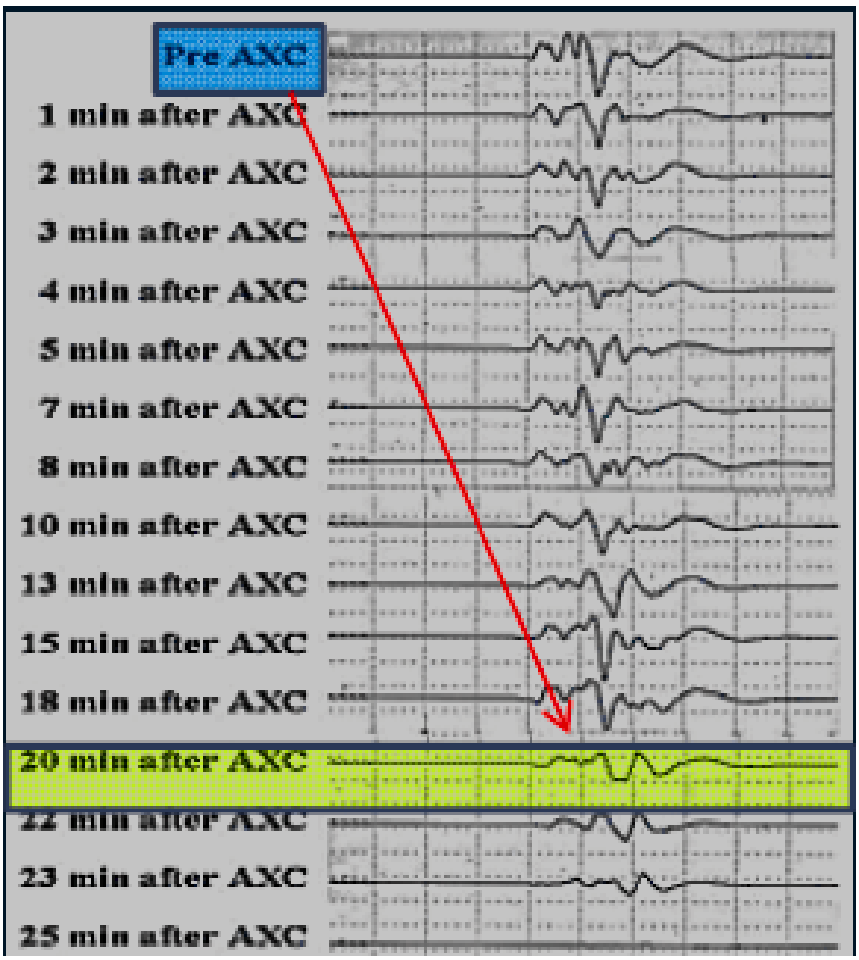

Figure 1.3: An example showing that evoked potentials can be temporally insensitive relative to the inciting event. The figure shows a case where, after aortic clamping, there was an approximately twenty minute delay in the loss of motor evoked potential signal amplitude (Kakinohana et al (*74*)).

Despite these caveats, MEP and SSEP monitoring remain the "gold standard" for functional monitoring of the spinal cord for spine and spinal cord surgery. Thus, the current "gold standard" for intraoperative monitoring of spinal ischemia, neurophysiological monitoring, has serious disadvantages and there is an unmet need for a device that can immediately and reliably monitor spinal cord hemodynamics.

Tools available to allow for the measurement of spinal cord blood flow are extremely limited. The ability to measure spinal cord blood flow with laser Doppler Flowmetry (LDF) has been demonstrated in both animal and human studies (*75-80*). LDF uses the Doppler shift of light – the frequency change that light undergoes when it reflects off of moving red blood cells – to measure flow in superficial volume under the probe (*81*). It consists of a low power laser source and detector placed a small distance apart that can only penetrate tissue depths of about 1.5 mm – 2 mm (*82*), which requires the probe to be placed in close proximity to the tissue. These devices measure flow in a very limited tissue volume, in close proximity to the probe tip. LDF sampling volumes are estimated at 0.3 -0.5 mm^3 (*83*). Additionally, positioning of the rigid probe is troublesome, the probes are prone to fracture, and they cannot be left in place for an extended period of time.

Non-invasive methods such as Single Photon Emission Computed Tomography (SPECT) (*84*) and Arterial Spin Labeled Magnetic Resonance Imaging (ASL-MRI) (*85*) have also been superficially explored as technologies for spinal cord blood flow measurement. While SPECT and ASL-MRI have superior spatial sensitivity, they are not feasible for continuous intra-operative monitoring. None of these modalities is currently practical for continuous or frequent monitoring.

1.3. Diffuse Optics for monitoring Spinal Cord Hemodynamics

An optical monitor capable of measuring spinal cord blood flow and or oxygenation does not exist. In this dissertation research, we proposed the development and testing of an optical monitoring device, employing DCS and DOS principles, for the real-time and continuous measurement of blood flow and oxygenation in the spinal cord respectively. Devices based on the diffuse optical principles of DCS and/or DOS have been extensively evaluated in other tissues, to include brain and muscle, using grossly similar probes, by our collaborators in the laboratory of Dr. Arjun Yodh at the University of Pennsylvania. Since DCS/DOS monitoring had not been previously used to evaluate spinal cord tissue hemodynamics, we proposed the designing of a novel fiber-optic probe for placement on spinal cord tissue in our sheep animal models. The probe would be lightweight, highly portable, thin, and flexible. This would enable the monitor to measure blood flow and oxygen as close to the site of injury as possible, due to the ability to place the probe within the spinal subdural or epidural space, with minimal or no intervening tissue to impair sensitivity, spatial, or temporal resolution. Furthermore, we proposed the probe design such that it could be placed via methods and approaches currently in clinical use and with proven safety (*86-92*). Safety of the materials used in manufacturing the probe was also considered; to make sure that there would be no adverse effects even after prolonged probe placement.

While intraoperative monitoring of spinal hemodynamics can help detect ischemia and assess the efficacy of interventions aimed at ameliorating ischemic conditions (*93*), it would be optimal to be able to identify preoperatively those individuals at greatest risk for spinal ischemia. Attempts to identify major feeding arteries have been published (*94*) yet such attempts are technically challenging and have not been widely adopted. There is no method currently available to determine the effect of a pre-identified “critical” vessel ligation upon cord function preoperatively. What is needed is a tool that can be deployed preoperatively to assess spinal cord blood flow response to a “test” occlusion. This would greatly assist surgical planning and risk assessment. We suggest that the proposed device could be place preoperatively, and the impact of aortic resection or stenting tested via “test” inflation of an intra-aortic balloon or test deployment of a retrievable stent “phantom”, a veritable spinal cord “stress-test”.

The ability to measure spinal cord blood flow and oxygenation would: 1) aid in the ability to expeditiously diagnose and monitor the progress of spinal cord ischemia, 2) offer an enhanced opportunity to prevent secondary injury, 3) allow the assessment of the efficacy of interventions aimed at ameliorating ischemia, 4) assist in early surgical stabilization of spinal trauma, 5) allow for the continuous assessment of spinal cord blood flow and oxygenation for several days after surgery, and 6) assist in the laboratory and clinical assessment of the efficacy of novel therapeutic approaches to ameliorate ischemia.

We have developed a near-infrared optical device that can accurately monitor and immediately detect the occurrence of spinal cord ischemia (*95, 96*). The device is based on the principles of Diffuse Correlation Spectroscopy (DCS) and Diffuse Optical Spectroscopy (DOS), which have previously been employed successfully in research to measure cerebral hemodynamics, in cancer diagnostics, and muscle perfusion studies (*97, 98*). The technique uses near-infrared light to probe deep tissues (up to a few centimeters), has a high temporal resolution (~ 2 - 3 sec), is non-invasive, and is portable (*99*).

Chapter 2

Theory of Diffuse Optics

This chapter elaborates on diffuse optics, which is the theoretical basis of our optical monitoring system. Diffuse optical spectroscopy (DOS), also known as diffuse reflectance spectroscopy (DRS) or near-infrared spectroscopy (NIRS), measures variations in the absorption and scattering of biological tissues due to changes in the concentrations of tissue chromophores. Diffuse Correlation Spectroscopy (DCS) provides a measure of relative blood flow by measuring the fast intensity fluctuations of light scattered off of the movement of red blood cells in tissue.

Common biological tissues have a “therapeutic window” wherein the absorption of light is low (*100*). This therapeutic window lies in the near-infrared range, typically from 650 nm to 900 nm, between the visible absorption bands of hemoglobin and the near-infrared absorption band of water (figure 2.1). The lack of absorption allows light within this window to penetrate up to a few centimeters deep into the biological tissues to probe the concentrations of the tissue chromophores.

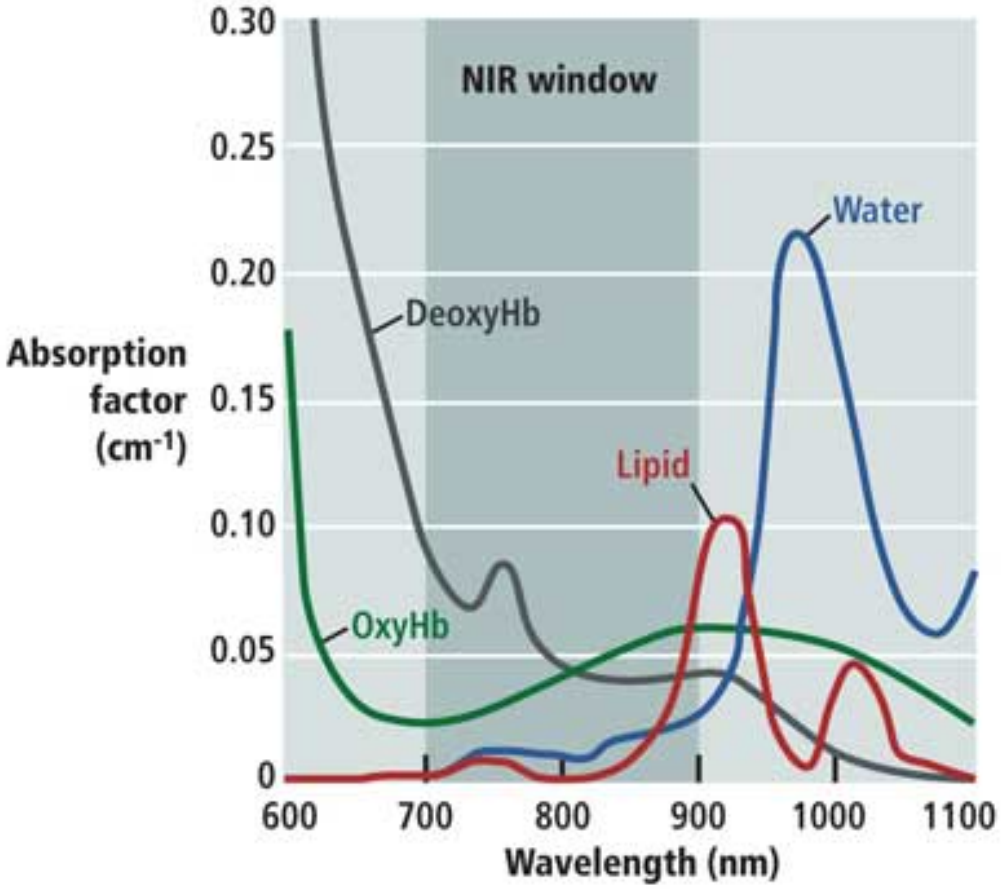

Figure 2.1: The therapeutic window of common biological tissues lies in the near-infrared range, typically from 650 nm to 900 nm, where the absorption of tissue chromophores is relatively low. $\boldsymbol{\mu_a}$ is the absorption coefficient which quantifies absorption. (http://www.vision-systems.com).

Two optical properties that are important in diffuse optics are the absorption coefficient $\boldsymbol{\mu_a(\lambda)}$ and the reduced scattering coefficient $\boldsymbol{\mu_s'(\lambda)}$. The absorption coefficient $\boldsymbol{\mu_a(\lambda)}$ is the reciprocal of the absorption length, which is the typical distance traveled by a photon before it is absorbed. This optical property characterizes the tissue medium, since it depends on the concentrations of the main chromophores in the tissue such as oxyhemoglobin ($\boldsymbol{HbO_2}$), deoxyhemoglobin ($\boldsymbol{Hb}$), water, and lipid.

The wavelength-dependent scattering length, which is the scattering equivalent to the absorption length, is defined as the typical distance traveled by a photon before being scattered. The reciprocal of this scattering distance is called the scattering coefficient $\boldsymbol{\mu_s(\lambda)}$. The reduced scattering coefficient $\boldsymbol{\mu_s'(\lambda)}$ is used to characterize the scattering and is defined as the distance a photon travels before its direction becomes randomized. This is the reciprocal of one photon random walk step. It depends on two factors: the scattering coefficient $\boldsymbol{\mu_s}$ and the degree of forward scattering anisotropy of a typical scattering event.

2.1. Diffuse Optical Spectroscopy (DOS)

DOS is a widely used diffuse optical technique applied in both pulse and cerebral oximetry (*98, 101*). The wavelength-dependent differential absorption of near-Infrared light can be quantitatively related to the concentrations of tissue chromophores such as oxy-hemoglobin (HbO_2) and deoxy-hemoglobin (Hb) in the microvasculature (*102*).

The differential pathlength method was used to measure the temporal changes in the concentration of tissue chromophores (*103*). This method calculates the light intensity variation for each source-detector pair at each wavelength to find temporal changes in tissue optical properties and measure changes in absorption. The Beer-Lambert law, which is used to derive the differential pathlength method, relates

absorption of light to the concentration and thickness properties of an optically thin sample through which different wavelengths of light travel. The equation below calculates the optical density of the sample:

$$OD(\lambda) = -\ln(\frac{I(\lambda)}{I_0(\lambda)}) = -\mu_a(\lambda)L$$

Here $OD(\lambda)$ is the optical density of the sample,

$I_0(\lambda)$ is the intensity of the light incident on the sample,

$I(\lambda)$ is the transmitted intensity,

$\mu_a(\lambda)$ is the absorption coefficient,

L is the sample thickness or light pathlength.

By extracting values of $\mu_a(\lambda)$ from the equation above, we can calculate the concentration of chromophores in the sample. The changes in absorption can be related to the changes in chromophore concentration as follows:

$$\Delta\mu_a(\lambda) = \sum_i \epsilon_i\,(\lambda)\Delta C_i$$

Here ΔC_i is the change in concentration of the ith chromophore in the sample, and their corresponding wavelength-dependent extinction coefficients are ϵ_i.

Biological tissue is highly scattering, and in turbid media, the intensity can be attenuated by both scattering and absorption. Photon pathlengths are also distributed from source to detector rather than being a single pathlength. Since one of the conditions of the Beer-Lambert law to hold is that the material must not scatter light, we cannot use the law directly for our application. We use the modified Beer-Lambert law that accounts for changes due to the scattering and absorption of light (*104*). This method is differential as it derives changes in chromophore concentrations from changes in light transmission.

We assumed that the brain and spinal cord tissue have similar hemodynamics. Since scattering changes are typically small in brain hemodymanics studies, we used $\Delta\mu_s' \approx 0$ and $\Delta\mu_a \approx 10$. To account for the increased distance that light must travel from source to detector because of the scattering and absorption effects, a unitless wavelength-dependent factor, the differential pathlength factor (DPF) has to be considered (*105*). With no scattering, the DPF would be one. Using these approximations, the modified Beer-Lambert Law is given below:

$$\Delta\mathrm{OD}(\lambda) = \Delta\mu_a(\lambda) L l_{DPF}(\lambda)$$

Here $\Delta\mathrm{OD}(\lambda)$ is the change in optical density at a given wavelength,

$\Delta\mu_a(\lambda)$ is the change in absorption coefficient,

L is the source-detector separation,

$l_{DPF}(\lambda)$ is the differential pathlength factor.

In the case of spinal cord tissue, the main chromophores that absorb light are oxyhemoglobin ($\Delta \boldsymbol{HbO_2}$) and deoxyhemoglobin ($\Delta H_b$). The modified beer-Lambert law can then be re-written as follows:

$$\Delta \mathrm{OD}(\lambda) = \left[\epsilon_{\boldsymbol{HbO_2}}(\lambda)\boldsymbol{\Delta HbO_2} + \epsilon_{Hb}(\lambda)\Delta Hb\right] L l_{DPF}(\lambda)$$

Where $\epsilon_{\boldsymbol{HbO_2}}(\lambda)$ and $\epsilon_{Hb}(\lambda)$ are the wavelength-dependent extinction coefficients for oxy- and deoxyhemoglobin.

To calculate changes in oxy- and deoxyhemoglobin using two wavelengths, the following equations would be used:

$$\boldsymbol{\Delta HbO_2} = \frac{\epsilon_{Hb}(\lambda_1)\Delta\mu_a(\lambda_2) - \epsilon_{Hb}(\lambda_2)\Delta\mu_a(\lambda_1)}{\epsilon_{Hb}(\lambda_1)\epsilon_{\boldsymbol{HbO_2}}(\lambda_2) - \epsilon_{\boldsymbol{HbO_2}}(\lambda_1)\epsilon_{Hb}(\lambda_2)}$$

$$\Delta \mathrm{Hb} = \frac{\epsilon_{\boldsymbol{HbO_2}}(\lambda_2)\,\Delta\mu_a(\lambda_1) - \epsilon_{\boldsymbol{HbO_2}}(\lambda_1)\,\Delta\mu_a(\lambda_2)}{\epsilon_{Hb}(\lambda_1)\epsilon_{\boldsymbol{HbO_2}}(\lambda_2) - \epsilon_{\boldsymbol{HbO_2}}(\lambda_1)\epsilon_{Hb}(\lambda_2)}$$

The total hemoglobin concentration change can then be calculated as follows:

$$\Delta \mathrm{THC} = \boldsymbol{\Delta HbO_2} + \Delta \mathrm{Hb}$$

Where $\Delta \mathrm{THC}$ is the total hemoglobin concentration change.

For our experiments, light intensity variation for each source-detector pair at each wavelength was processed to derive chromophore concentration changes, and therefore changes in oxy- (ΔHbO_2) and deoxy-hemoglobin (ΔHb), by using the modified Beer-Lambert law with a differential pathlength factor (DPF) of 4 for all three wavelengths (*106*). The values of the differential pathlength factor depend on source-detector separation, tissue geometry, wavelength of light, and baseline optical properties (*107*). The DPF value was chosen based on the previous experiences of Dr. Yodh's group with other tissues such as brain (*108*), since no values are available for spinal cord in the literature. Tissue oxygen saturation ($S_tO_2(t)$) was determined as the ratio of $HbO_2(t)/[HbO_2(t) + Hb(t)]$. Changes in S_tO_2 (ΔS_tO_2) were calculated relative to a baseline period. The absolute baseline hemoglobin concentration was determined independently with a homemade white-light spectrometer system (*99, 109*), yielding a mean (standard error) of 27.2 (7.8) μmol and 10.5 (1.7) μmol for HbO_2 and Hb, respectively.

2.2. Diffuse Correlation Spectroscopy (DCS)

DCS is a novel optical technique used to measure blood flow in deep tissues by quantifying the temporal intensity fluctuations of the detected light (*98, 99*). These fluctuations arise mainly from moving light scatterers in tissue, e.g., red blood cells (RBCs). In practice, these fluctuations are quantified by the decay rate of the temporal intensity autocorrelation function of the detected light. The decay rate of the

autocorrelation function is dependent on the “average” flux of red blood cells in the vasculature. Changes in spinal cord blood flow were estimated from the experimental DCS data by fitting the measured intensity autocorrelation function $g_1(\tau)$ to the solution of the photon correlation diffusion equation in the semi-infinite geometry (figure 2.2) (*110*).

Diffuse Correlation Spectroscopy (DCS) is a relatively novel technique compared to DOS, and uses near-infrared light for continuous non-invasive measurement of relative blood flow in deep tissues. The technique aims to quantify the fluctuations of the detected light that occur due to the motion of scatterers in tissue, mainly red blood cells (*101, 111*). The temporal intensity autocorrelation function is the mathematical approach used to measure these fluctuations. Briefly, the autocorrelation function is designed to measure the degree of similarity of the light intensity measurements taken over short periods of time. The strength of the correlation between the DCS signal taken at two different time points will depend on the amount of fluctuation in the intensity of light that occurs within that time interval. Over time, as red blood cells diffuse further away, it is expected that the value of the autocorrelation will decay in a non-linear fashion. The faster the red blood cells are moving, the greater the fluctuations in light intensity, and the faster the decay of the autocorrelation function. Therefore, DCS has the ability to detect relative changes in the rate of blood flow. Its high temporal resolution (~100ms) enables it to immediately detect changes in blood flow in tissue.

The technique has been extensively validated, both in animals and in humans. Measurements in brain and muscle have been compared with perfusion measurements acquired with arterial spin-labeled MRI (*102, 112*), Xenon-CT (*113*), laser Doppler flowmetry (*99*), and transcranial Doppler ultrasound (*114, 115*). The technique has been successfully applied in to the study of cerebrovascular diseases (*112-116*), muscle physiology (*117-119*), and tumor physiology (*120-122*). DCS shares all the features of DOS, including portability, non-invasiveness, and the ability to probe deep tissues. However, it provides a qualitatively different physiological signal. In DOS, the signal is related to the hemoglobin concentration changes via optical absorption. By contrast, the DCS signal is due to the motion of scatterers in the tissue. No significant cross-talk between DOS and DCS, allows for continuous relative measurements of both blood flow and tissue oxygenation

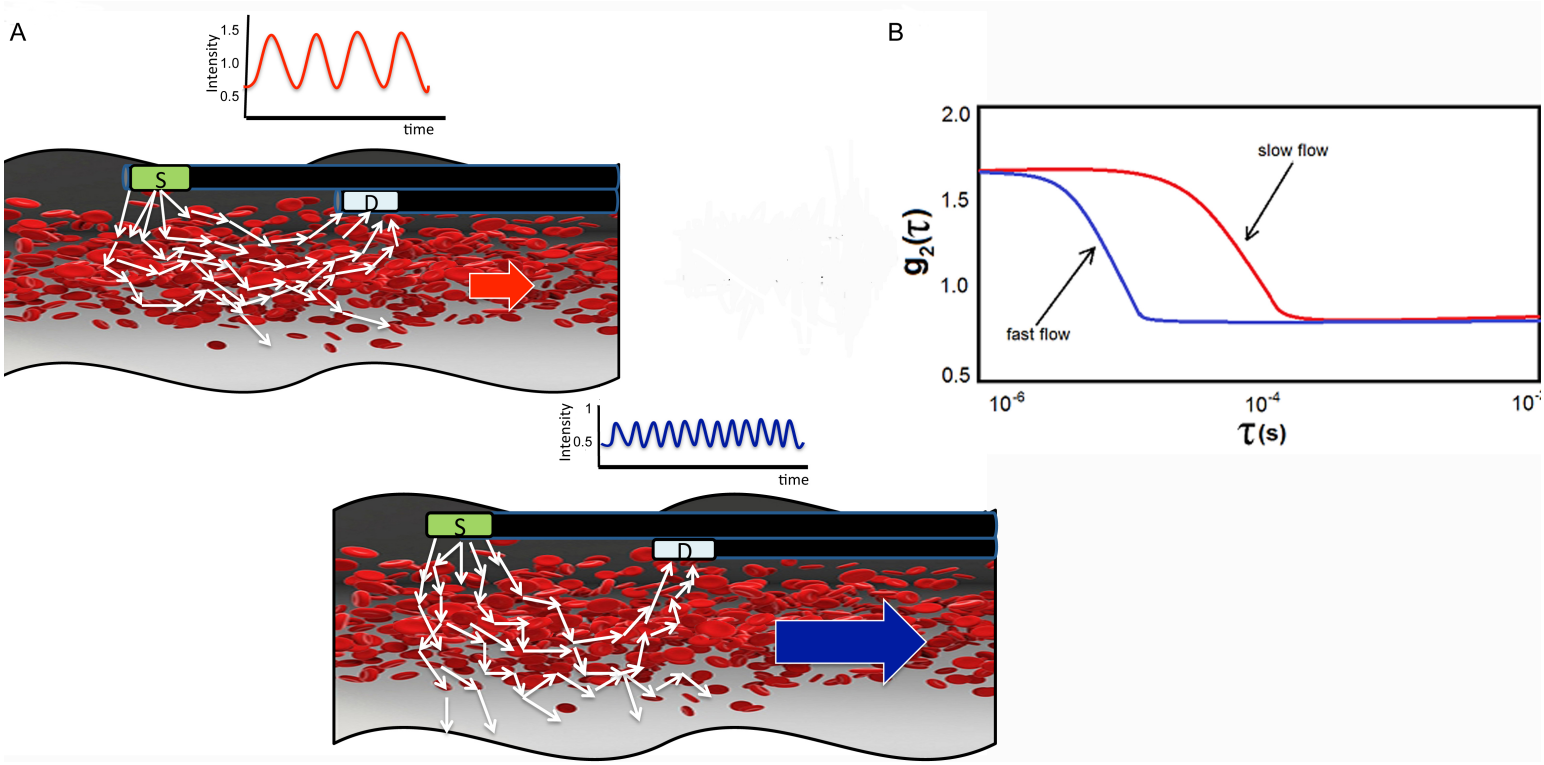

Figure 2.2: Schematic of the diffuse correlation spectroscopy (DCS) measurement. (A) DCS measures the fluctuations of detected light intensity, which occur due to the motion of scatterers such as erythrocytes. The strength of the correlation in DCS signal between two time points depends on the movement of erythrocytes. Thus, higher blood flow (faster displacement of the erythrocytes, indicated by the blue arrow) leads to greater fluctuations in signal intensity and lower correlation of the DCS signal with itself, resulting in the faster decay of autocorrelation of the intensity detected at the output fibers. Lower displacement of erythrocytes (indicated by the red arrow) leads to a slower decay of the intensity autocorrelation function. (B) The fluctuations in light intensity detected by the avalanche photodiode detectors are fed to an autocorrelator that computes the normalized temporal intensity autocorrelation function g2 (τ) from photon arrival times. τ(s) represents the autocorrelation function time delay. D = detector fiber; S = source fiber.

Measures of spinal cord blood flow were estimated from DCS data by fitting the measured intensity autocorrelation function g2(τ) to the solution of the photon correlation diffusion equation in the semi-infinite geometry with extrapolated zero boundary conditions (*101, 123*). The solution of the photon correlation diffusion equation is given below:

$$\nabla.\left(D(r)\nabla G_1(r,\tau)\right) - v\left(\mu_a(r) + \frac{\alpha}{3}\mu_s' k_0^2 \langle \Delta r^2(\tau)\rangle\right) G_1(r,\tau) = vS(r,t)$$

Here,

G1(r, t) = ⟨E*(r, t)E(r, t + t)⟩ is the unnormalized temporal electric field (E(r, t)) autocorrelation function in the medium at position r and time t;

t is the autocorrelation function time delay, and the brackets represent time and/or ensemble averages.

$D \cong {}^{1}/_{(3\mu_s')}$ is the light diffusion coefficient in the medium;

μ_a is the absorption coefficient;

μ_s' is the reduced scattering coefficient (i.e. the inverse of the photon random walk step-length);

v is the speed of light in the medium,

S(r, t) represents the light source.

α represents the fraction of photon-scattering events that occur from moving particles in the medium (e.g. red blood cells; RBCs);

$\langle \Delta r^2(\tau) \rangle$ is the mean-square particle displacement in time τ (i.e. in tissue, the mean-square displacement factor could characterize the motions of RBCs in the tissue vasculature);

$k0 = 2\pi/\lambda$ is the wavenumber of the light diffusing through the medium.

We assume a semi-infinite geometry with extrapolated zero boundary conditions. The Brownian motion model is used to approximate the mean-square particle displacement of the moving scatterers in the tissue (eg. RBCs), as described below:

$$\langle \Delta r^2(\tau) \rangle = 6D_B\tau$$

where D_B represents the effective diffusion coefficient of the moving scatterers.

Similar to traditional dynamic light scattering, we measure the intensity autocorrelation function in our experiments instead of the field correlation function. The Siegert relation can be used to relate measurements of the intensity autocorrelation function to the theory for the electric field autocorrelation function, without direct measurement of phase information. (*124*).

The measurement of the normalized intensity autocorrelation function

$$g_2(\tau) = \langle I^*(\tau = 0)/(\tau)\rangle / \langle I(\tau = 0)\rangle^2$$

can be related to the normalized electric field correlation function,

$$g_1(\tau) = \langle E^*(\tau = 0)E(\tau)\rangle / |E(\tau = 0)|^2$$

by the Siegert Relation:

$$g_2(r, t, \tau) = 1 + \beta |g_1(r, t, \tau)|^2$$

Here, β is a parameter that depends on the source coherence, detection optics, and other external factors.

In order to estimate relative blood flow from the DCS data, we fit the measured intensity autocorrelation functions to the Siegert relation, to extract both β and a blood flow index (*BFI*), defined as:

$$BFI(t) \equiv \alpha D_B(t)$$

Typically, best fits to either $g_1(\tau)$ or $g_2(\tau)$ are employed to derive a best estimate for the dynamical tissue factor, $a\langle\Delta r^2(\tau)\rangle$. Figure 2.3 below shows an example of sample autocorrelation curves.

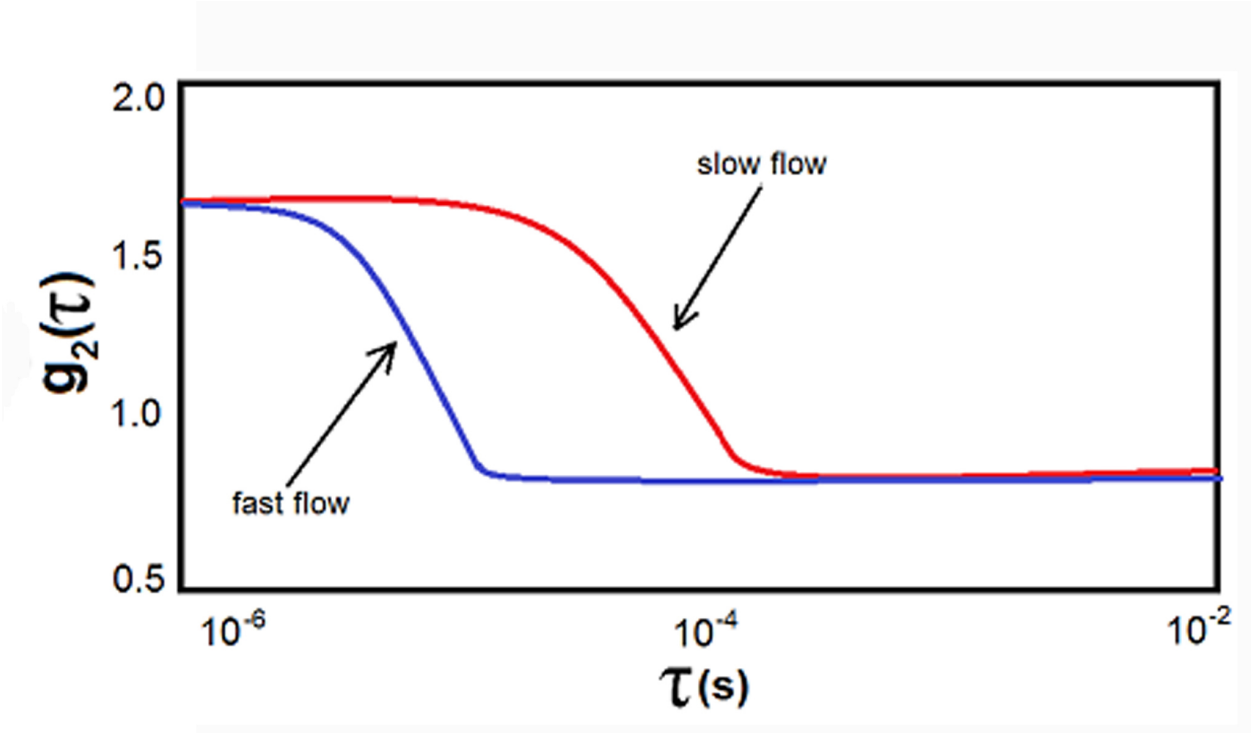

Figure 2.3: The autocorrelation curves decay faster with increasing flow, and increased source-detector separation. The slope and/or the decay rate provide information about the optical properties of the tissue and the motion of the scatterers, mainly red blood cells.

For the case of random ballistic flow, $\langle\Delta r^2\tau\rangle = V^2\tau^2$,

where V^2 is the second moment of the cell velocity distribution.

For the case of diffusive motion, $\langle\Delta r^2(\tau)\rangle = 6D_B\tau$,

where D_B is the *effective* Brownian diffusion coefficient of the tissue scatterers.

The Brownian motion model was used to approximate the mean-square particle displacement of the moving scatterers in the tissue, and thus to derive a spinal cord blood flow index (BFI) (*123*). Relative changes in blood flow (ΔBF) were calculated by:

$$\Delta BF(t) = \Delta BFI(t) = \left(\frac{BFI(t)}{BFI(t_0)} - 1\right) \times 100\%$$

where t_0 denotes the baseline period, taken as the average BFI over two-minutes before the interventions.

It is important to note that DCS measures the relative changes in blood flow characterized by a blood flow index. All subsequent references in this dissertation to changes in blood flow measured by DCS indicate relative percent changes in blood flow, and not absolute blood flow (ml/min).

Chapter 3

Instrumentation of the DCS/DOS Monitor

This chapter focuses on developing an optical monitor by integrating DCS and DOS principles and designing a fiber-optic probe that would be capable of successfully monitoring immediate changes in spinal cord blood flow and oxygenation as hypothesized. The DCS module was custom built at our lab in Stony Brook. Since DOS has been extensively used in research and clinical settings, we decided to purchase a commercially available oximetry device (Imagent, ISS Inc., IL) and integrated the home-built DCS module with the commercially available DOS module. We also designed a prototypical linear optical probe based on our requirements for monitoring blood flow and oxygenation in the sheep spinal cord. While similar DCS modules have been used by our collaborators in Dr. Arjun Yodh's group at the University of Pennsylvania for monitoring blood flow in tissues such as breast (*125, 126*), muscle (*127-129*), brain (*130-133*), etc. and the Imagent device from ISS has been used primarily in brain research (*134-138*), the use of these devices for monitoring spinal cord hemodynamics is novel and undocumented.

3.1. DOS Module

For our experiments, we have used two DOS modules, both utilizing the same components and principles. The DOS data for our initial experiments was collected using a DOS module built by our collaborators in Dr. Arjun Yodh's laboratory at the University of Pennsylvania. Since DOS has been extensively used in research and clinical settings, for our subsequent experiments we decided to purchase a commercially available oximetry device (Imagent, ISS Inc., IL) and integrated the home-built DCS module with the commercially available DOS module. The system consists of three laser diodes in the near-infrared range (685 nm, 785 nm, and 830 nm), modulated at high frequency (70 MHz - 110 MHz) by a 1 x 8 RF splitter (ZFSC-8-1, Mini-Circuits, NY). The output light from the lasers goes through two optical switches (DiCon, CA) before travelling through the source fibers. The first switch ensures that only one wavelength is delivered at a time, while the second helps direct the light to different positions on the spinal cord. Photomultiplier tubes (PMT, R928, Hamamatsu, Japan) are used to detect the signal from the tissues. An in-phase/ quadrature (I/Q) demodulator (MIQY-70D; Mini-Circuits, NY) extracts the amplitude and phase information from the RF signal. Low pass filters of 100 Hz on each channel and a 16-bit analog-to-digital converter board (PXI-6251, National Instruments, TX) are used for data acquisition.

We employ the frequency-domain technique for DOS measurements, wherein the light source is modulated with a radio-frequency (RF) sinusoidal signal. Information about the optical properties of the turbid medium is extracted from both the amplitude attenuation and phase shift of the input light from the laser sources versus the detected light, as shown in figure 3.1 below.

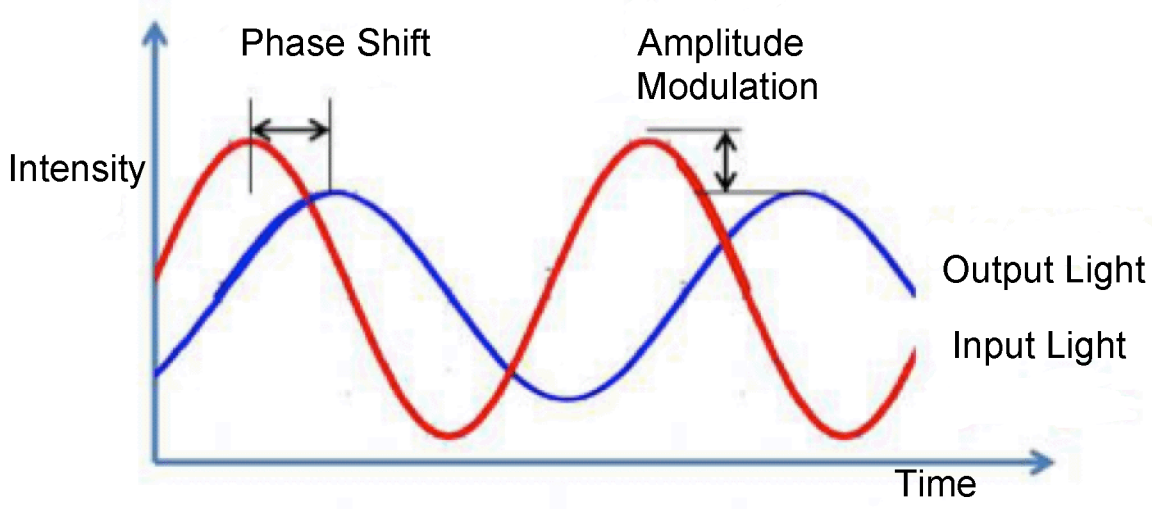

Figure 3.1: For our Diffuse Optical Spectroscopy (DOS) measurements, we use a frequency-domain technique where the input light from the laser source is sinusoidally modulated. The information about the optical properties of the medium is extracted from both the subsequent amplitude attenuation and the phase shift of the detected light.

Our DOS module uses a homodyne detection technique. Light is detected, translated into an electronic signal by the detector, then amplified and sent to an in-phase/in-quadrature (IQ) demodulator. The outputs of the IQ demodulator, i.e., the in-phase and in-quadrature parts, are the sine and cosine components of the signal respectively.

The RF oscillator provides a sinusoidal reference signal for both the laser diode and IQ demodulator on the detection side. This intensity-modulated light is transmitted to a turbid medium through a multimode optical fiber on the source side. Light that has traveled through the medium and reaches the APD or PMT detector is then amplified and put through the IQ demodulator.

In the IQ demodulator, both the reference signal from the oscillator ($A_{ref}\ \sin\omega t$) and the signal from the detector ($A_{det}\sin(\omega t + \theta)$) are split in two. Here, θ represents the phase shift with respect to the reference. One of the reference signal arms is shifted by $90°$, while the other is not. Neither of the detected signal arms is phase-shifted. The non-shifted reference and detector signals are multiplied for the in-phase component:

$$I(t) = \frac{1}{2}A_{ref}\sin\omega t \cdot A_{det}\sin(\omega t + \theta) + I_{off}$$

$$= \frac{1}{8}A_{ref}A_{det}[\cos\theta - \cos(2\omega t + \theta)] + I_{off}$$

where I_{off} is the in-phase DC offset term.

Similarly, when the reference signal that has been shifted by $90°$ and the detector signal are multiplied, they create the in-quadrature component:

$$Q(t) = \frac{1}{2} A_{ref} \cos \omega t \cdot A_{det} \sin(\omega t + \theta) + Q_{off}$$

$$= \frac{1}{8} A_{ref} A_{det} [\sin \theta + \sin(2\omega t + \theta)] + Q_{off}$$

where Q_{off} is the IQ DC offset term.

After the IQ modulator, low pass filters remove the high frequency components of the signal, i.e. the $2\omega t$ components in the equations above, resulting in two DC signals:

$$I_{DC} = A \cos \theta + I_{off}$$

$$Q_{DC} = A \sin \theta + Q_{off}$$

where $A = \frac{1}{8} A_{ref} A_{det.}$

I_{DC} and Q_{DC} then travel by RF-shielded cables to a digital-to-analog data acquisition board, which is then recorded by a computer. The amplitude (A) and phase (θ) of the detected signal can then be calculated from I_{DC} and Q_{DC} and their DC offsets for each frame of data using our analysis software:

$$A = \sqrt{[I_{DC} - I_{off}]^2 + [Q_{DC} - Q_{off}]^2}$$

$$\theta = arctan\left[\frac{Q_{DC} - Q_{off}}{I_{DC} - I_{off}}\right]$$

I_{off} and Q_{off} are measured by obtaining values of I_{DC} and Q_{DC} while blocking input light. Since the levels may change over the course of an experiment, it is best to have values of offset for every frame of data. A and θ can then be used to obtain optical properties of the medium using the approach described in Chapter 2.

3.2. DCS Module

This section focuses on the DCS module of the optical monitor, the component that is responsible for collecting blood flow data. I built the DCS module in our lab based on the modules that have been used by our collaborators in Dr. Arjun Yodh's group at the University of Pennsylvania. The components required to put together the DCS module will be described in detail, followed by the assembly and testing of the DCS component.

3.2.1. Components

There are three primary components within the DCS module: lasers, detectors and a correlator. The light source comprises of two narrowband, continuous wave, diode lasers, in the near- infrared range (785 nm), with long coherence length (> 20 m) as light source (CrystaLaser inc., NV). A long coherence laser is needed in order to preserve the coherence of photons that migrate through the tissues. The light beam is delivered to the tissue through an optical fiber, with an output power of approximately 5-15 mW. The light intensity fluctuations within a single speckle area are detected using a single-mode fiber ($\sim 6\,\mu m$). Eight fast single photon-counting Avalanche Photodiodes (SPCM-AQR-14-FC, Pacer Components Inc., UK) are used as detectors. An eight-channel multi-tau correlator board (Flex03OEM-8CH, Correlator.com, NJ) facilitated measurements of blood flow by taking the TTL output of the photon arrival times from the APDs and calculating the normalized temporal intensity autocorrelation functions of the detected signal.

The laser source (DL785-100-SO, CrystaLaser Inc., NV) used in our DCS module employs a continuous-wave, single longitudinal mode, 785 nm wavelength in the near-infrared range, enabling the probing of deep tissue up to a few centimeters. The long coherence length of >20 m is required to preserve the coherence between fields from both the shortest and longest path lengths through the tissue. The 100 mW power of the laser provides a satisfactory correlation curve and is relatively low enough to prevent damage to the spinal cord tissue due to laser heating. TTL modulation turns the laser on and off; this option enables the switching between DCS and DOS

acquisition by turning the DCS laser off during the DOS acquisition cycle. TTL modulation is preferable to using an optical isolator where there is the potential for loss of light and hence output power from the laser.

The lasers have good output stability of <1% over 24 hours. However, it is advisable to test the laser stability using a power meter before wiring the DCS components. The power should match the company specifications when tested directly out of the laser output and through the 65μm FC-FC fibers provides through the company. Next, we have to make sure that the TTL pulse will be able to turn the laser on (TTL HIGH) and off (TTL LOW) when the laser is connected to the data acquisition (DAQ) digital output. To make sure there is no leakage, the power should be tested straight out of the laser output when the TTL is low and it should be only a few microwatts or less. Finally, an overnight stability test should be performed to record the analog output from the power meter and there should be minimal deviation. Figure 3.2 shows an example of the DCS laser power output where there was no large jump in power and the percent standard deviation was minimal.

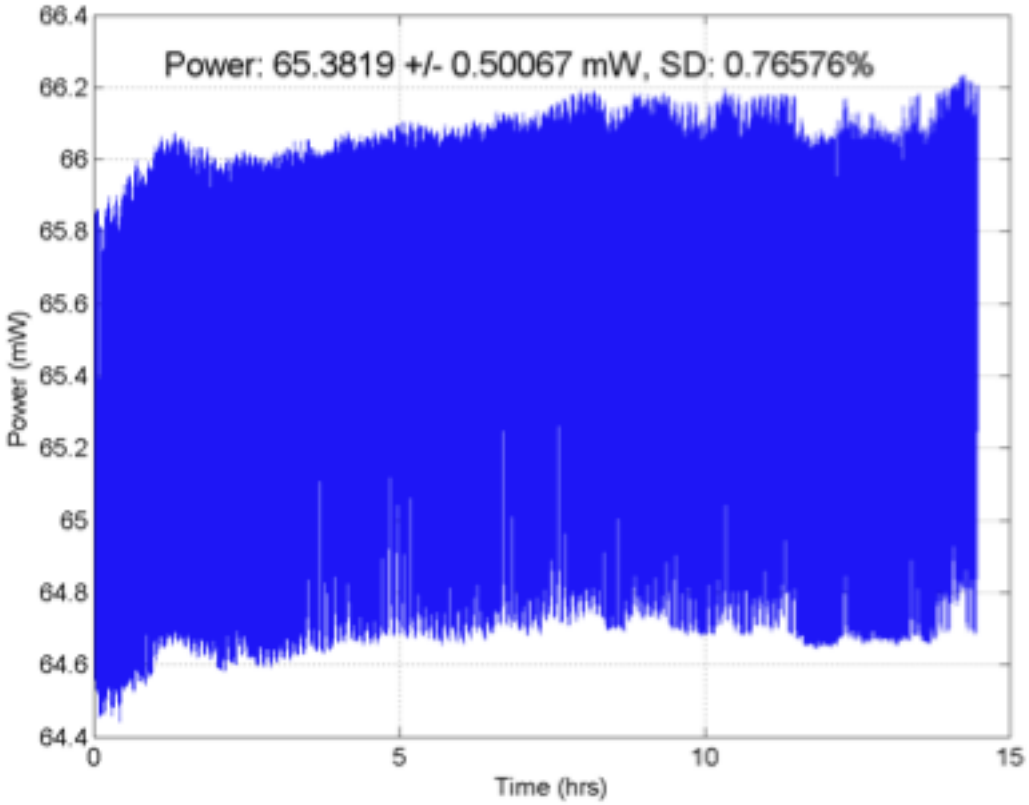

Figure 3.2: Example of results from an overnight stability test showing good stability of the output power of a Diffuse Correlation Spectroscopy (DCS) laser.

The DCS module uses single-photon counting avalanche photodiodes (APDs) as detectors. Factors to be taken into consideration to ensure adequate detection include single-photon detection capability, good photon detection efficiency in the near-infrared range, and compactness to minimize the size of the DCS box and make it portable. For our DCS module, we used four channel APD arrays as detectors (SPCM-AQ4C, PerkinElmer Inc., Quebec, CA), with a photon detection efficiency of approximately 50% at 785 nm. Interface boards (SPCM-AQ4C-IO, PerkinElmer Inc., Quebec, CA) facilitate the power and signal connections to the APD array.

The APD array requires three power supplies at three different voltages of +2 V, +5 V and +30 V, as summarized in table 3.1 below. The power supplies must be well regulated and have low ripple noise of <50 mV p-p. The +2 V power supply is required to provide cooling for the APDs. The cooler circuit will compensate for the APD card heating up as the count rates increase, by transferring heat from the detector to a heat sink. The +5 V power supply is for the TTL pulses.

Voltage	Min. Voltage	Max. Voltage	Typical Current	Max. Current	Power (for 2 Arrays)
+2 V	1.95 V	2.05 V	1.0 A	4.0 A	2×6 W = 12 W
+5 V	4.75 V	5.25 V	0.20 A	1.0 A	2×5 W = 10 W
+30 V	29 V	31 V	0.01 A	0.04 A	2×1.2 W = 2.4 W

Table 3.1: Power Supply Requirements for the Avalanche Photodiode Detector Arrays

The SPCM-AQ4C-IO interface board has two rows of four BNC connections each. The bottom row of BNC connectors is the TTL signal output of photon counts from the APDs, which gets sent directly to the hardware correlator board. The top row is a gate input that controls the APD function through a digital input. When there is no gate input or floating gate input, the APDs are ready to count photons. The channels will be gated off through an applied TTL HIGH signal. For our current DCS box configuration, we control the APD power using toggle switches within the circuit. We have not applied the gate input feature of the interface board yet; the software control of the APDs instead of using toggle switches could be useful in future DCS modules.

The TTL signal output for each photon from the APDs is sent to a “multi-tau” hardware correlator board (Correlator.com, Bridgewater, NJ). The correlator then calculates various parameters that are sent via USB connection to a computer. The hardware correlator experimentally performs the photon correlation measurement by performing four basic tasks, as stated in the technical manual provided by Correlator.com:

1. Counting the arrival of input pulses over sampling intervals spaced on a grid defined by the sampling time Δt_0.

2. Delaying the count sequence for a lag time, $k\Delta t_0$ (k being number of channels), and storing this sequence.

3. Multiplying the two count sequences.

4. Accumulating the products, or calculating their sum.

Multi-tau correlation refers to the multiple sample times (taus) that are processed simultaneously by the correlator (*139*). This approach greatly reduces the computational load and allows users to access both small and large taus, as required. The eight-channel correlator we use in the DCS box has the layout as shown in figure 3.3 below.

Since the bin width doubles every sixteen registers, registers 1-16 comprise the first tier with bin width t_0 = 200 ns. The next eight registers of the second tier have t_0 = 400 ns, the next eight registers of the third tier have t_0 = 800 ns, and so on.

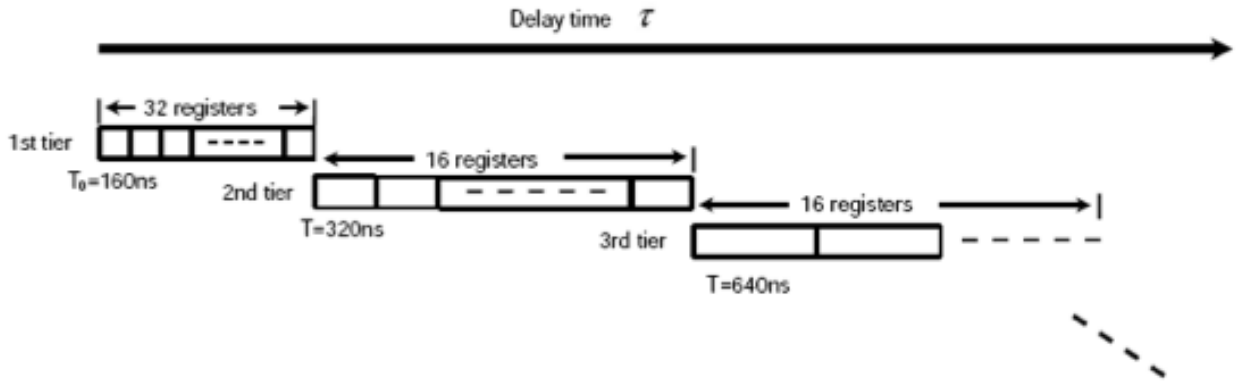

Figure 3.3: Diagram showing the multi-tau correlation scheme employed by the hardware correlator board used in the DCS module to compute the normalized temporal autocorrelation function g_2. [Figure adapted from the technical specifications manual for the correlator purchased from Correlator.com]

At the start of a measurement, the digital counter reports photon counts within each bin time of the first register. Those values in the first register shift to the next register as a new value comes in from left. This goes on until all registers are filled. Before each shift, temporal autocorrelation functions (G_2) are calculated

$G_2(\tau_i) = \langle n_i \cdot n_0 \rangle$

where n_i is the photon count in i^{th} register,

n_0 is the photon count in the register for zero delay time (τ = 0),

τ_i is the delay time between n_i and n_0.

The autocorrelation functions are then normalized in a separate register to create the normalized temporal autocorrelation function g_2. An average of these g_2 traces are calculated over the entire duration to produce a final, averaged g_2 curve. The duration is preset to 3 seconds for our experiments. This g_2 is a single data point in time and DCS uses g_2 values from every subsequent time point to compute the relative blood flow.

3.2.2. Assembling the DCS Module

I built the DCS module at our lab in Stony Brook University, with the same specifications as the DCS boxes used by our collaborators at the University of Pennsylvania. The novelty of our experiments is the application of DCS to monitor the blood flow and oxygenation in the spinal cord of sheep. To accommodate monitoring of the spinal cord tissue in sheep, the fiber-optic probe design had to be novel. Therefore, the DCS box we built can be used to collect blood flow information from any tissue, such as brain, breast, spinal cord, etc. The fiber-optic probes used for measurement are designed variably to match the application it will be used for.

Although we only use the one laser source and two APD detectors configuration for our spinal cord blood flow measurements, we built a DCS box with two laser sources and eight APDs to allow realization of our long-term goal of measuring multiple vertebral levels of the spinal cord. Figure 3.4 below shows the front panel of a standard DCS module. Each laser source has an input (top left) and a corresponding power supply (bottom left). The two four-channel APD arrays on the right are turned on and off using toggle switches. In the configuration that we currently use, the upper toggle switch turns on channels 1-4, while the lower toggle switch controls channels 5-8. The APDs cannot be turned on individually.

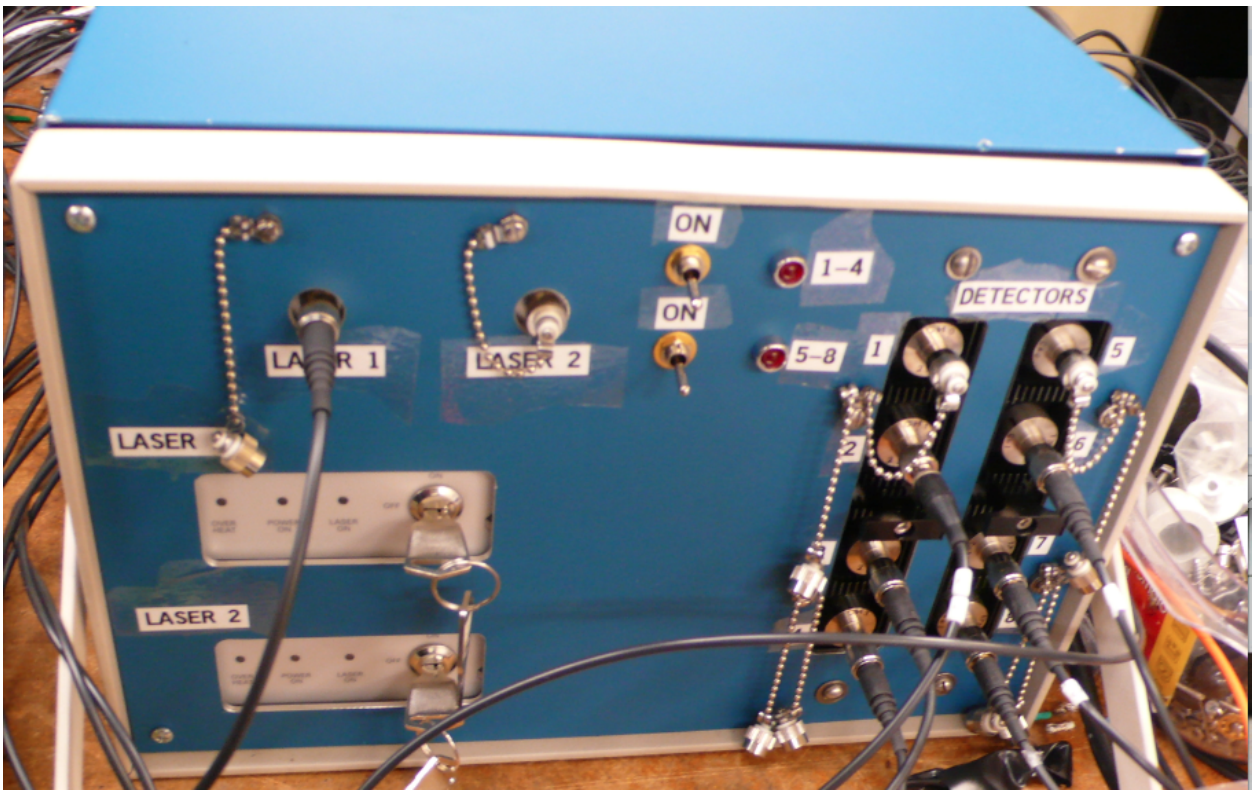

Figure 3.4: The front panel of the DCS module built in our lab at Stony Brook, showing two laser input sources (top left) and their power supplies (bottom left), and eight avalanche photodiode detectors (right) that are turned on and off using two toggle switches (center).

The back panel comprises of two BNC inputs that are used for turning the laser sources on and off through TTL pulses, a USB cable that connects the hardware correlator board to a computer, and a power cord that supplies power to the DCS module. There is also a fan on top of the box to provide cooling of the internal DCS components.

Figure 3.5 shows an internal view of the DCS components. The APDs also require three power supplies of +2 V, +5V and +30 V to operate, as described in section 3.2.1. above. Figure 3.6 below shows the electrical connections from the APDs to the

power supplies. While the grounds of the power supplies connect directly to the APDs, the voltages must go through the toggle switches. The 5 V power supply also controls indicator lights that are turned on as the APDs turn on. BNC cables connect the APDs to the correlator board. A USB cable sends the correlator board output to a computer.

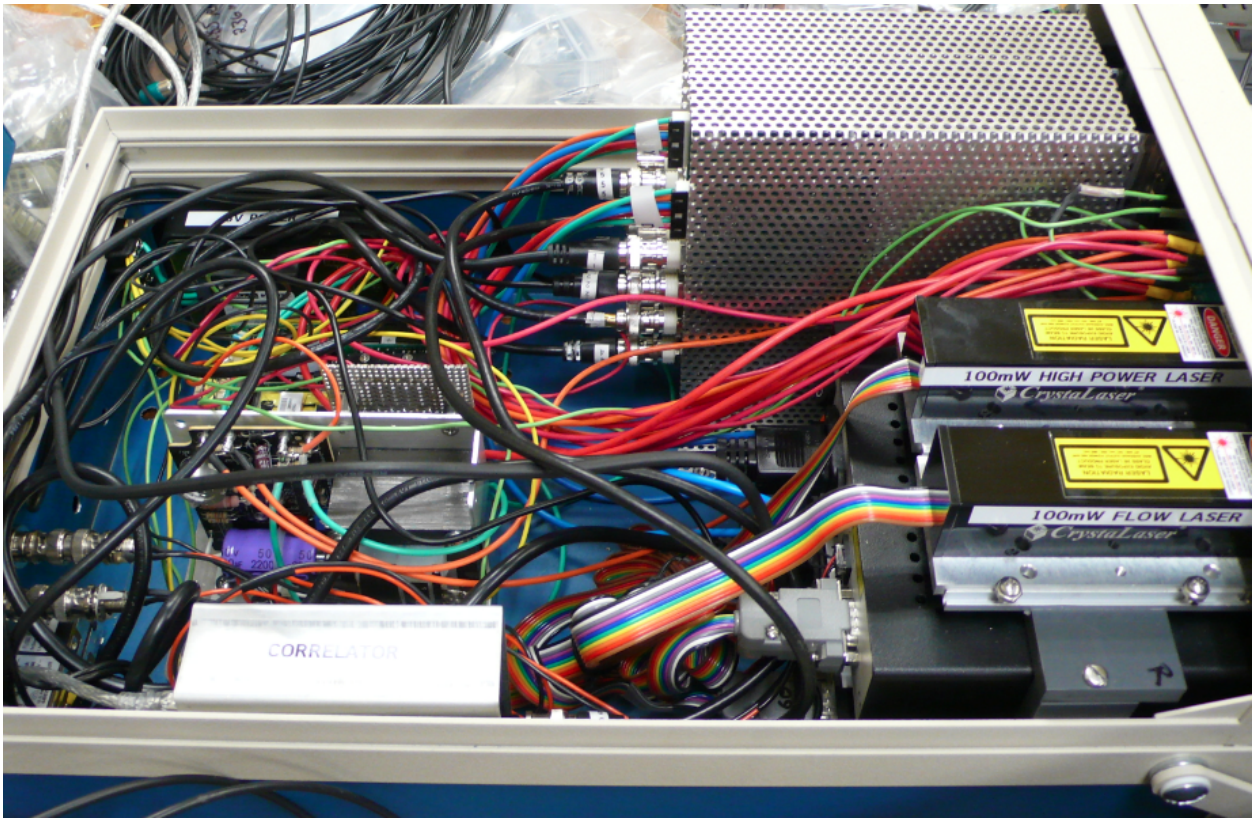

Figure 3.5: Inside view of the DCS components.

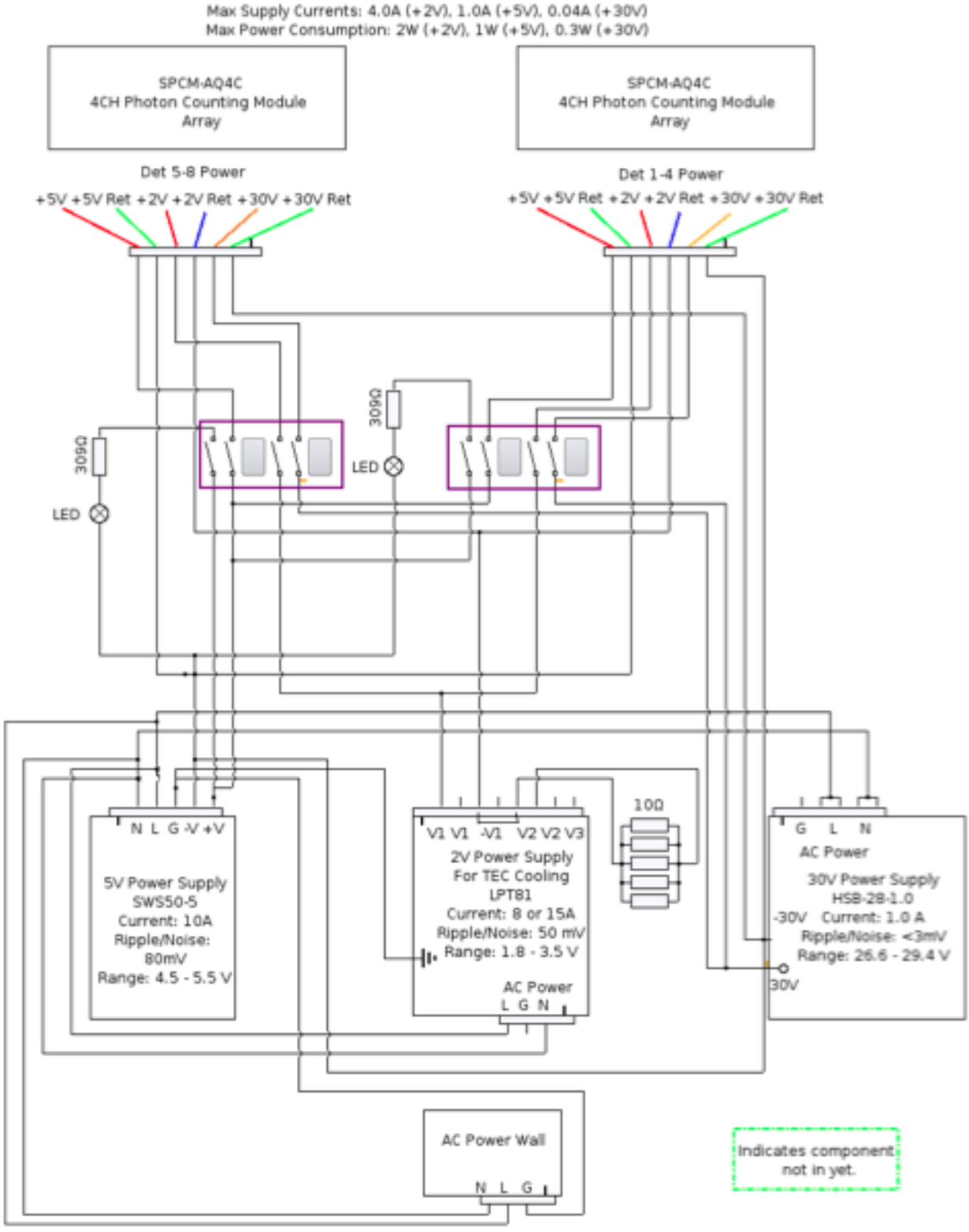

Figure 3.6: Electrical connections of the power supplies to the avalanche photodiode detectors. (Figure from the dissertation of Meeri Kim, University of Pennsylvania, 2013).

3.3. Fiber-optic probe for spinal cord monitoring

From diffusion theory, in the reflection geometry, the maximum penetration depth of diffuse light in tissue depends on the optical properties of the tissue and the source-detector (S-D) separation. For the spinal cord tissue optical parameters we typically encounter, this mean depth is roughly one-half of the S-D separation, with a width of the same order (*140, 141*). Therefore, different S-D separations predominately provide the information about particular tissue regions. Analysis of the relative physiological changes at different levels of the tissue can be separated by measuring light absorption and the electric field temporal autocorrelation function at different source-detector separations. Thus, the S-D separation plays an important role in determining the depth of tissue penetrated by the laser light, with greater S-D separation leading to greater optical penetration of tissue.

We designed a thin (less than 1mm in diameter), linear fiber optic probe (manufactured by Fiberoptic Systems Inc., CA) with two S-D separations at 1.0 cm and 2.0 cm (figure 3.7 and 3.8). Since we have measured the sheep spinal cord to be approximately 1 cm in diameter, we assumed the above source-detector configuration would work as it would interrogate sheep spinal cord tissue depth of ~0.5 – 1.0 cm. The probe consists of silica glass fibers covered with Teflon. Since Teflon has been widely used in catheters and vascular grafts, and its safety profile as a fiber-optic probe enclosure has been well documented (*142, 143*), we hypothesized that the optical probe would be biocompatible and could be used for continuous monitoring over long periods

of time. The probe materials and dimensions are similar to those of epidural catheters, which are routinely placed onto the spinal cord of patients in the operating room using an epidural Tuohy needle. Thus, we predict minimally invasive placement of the optical probe on to the spinal cord would be possible using an approach similar to that of epidural catheter placement. The probe is 3 m long, allowing the optical device to be positioned distant to the surgical site.

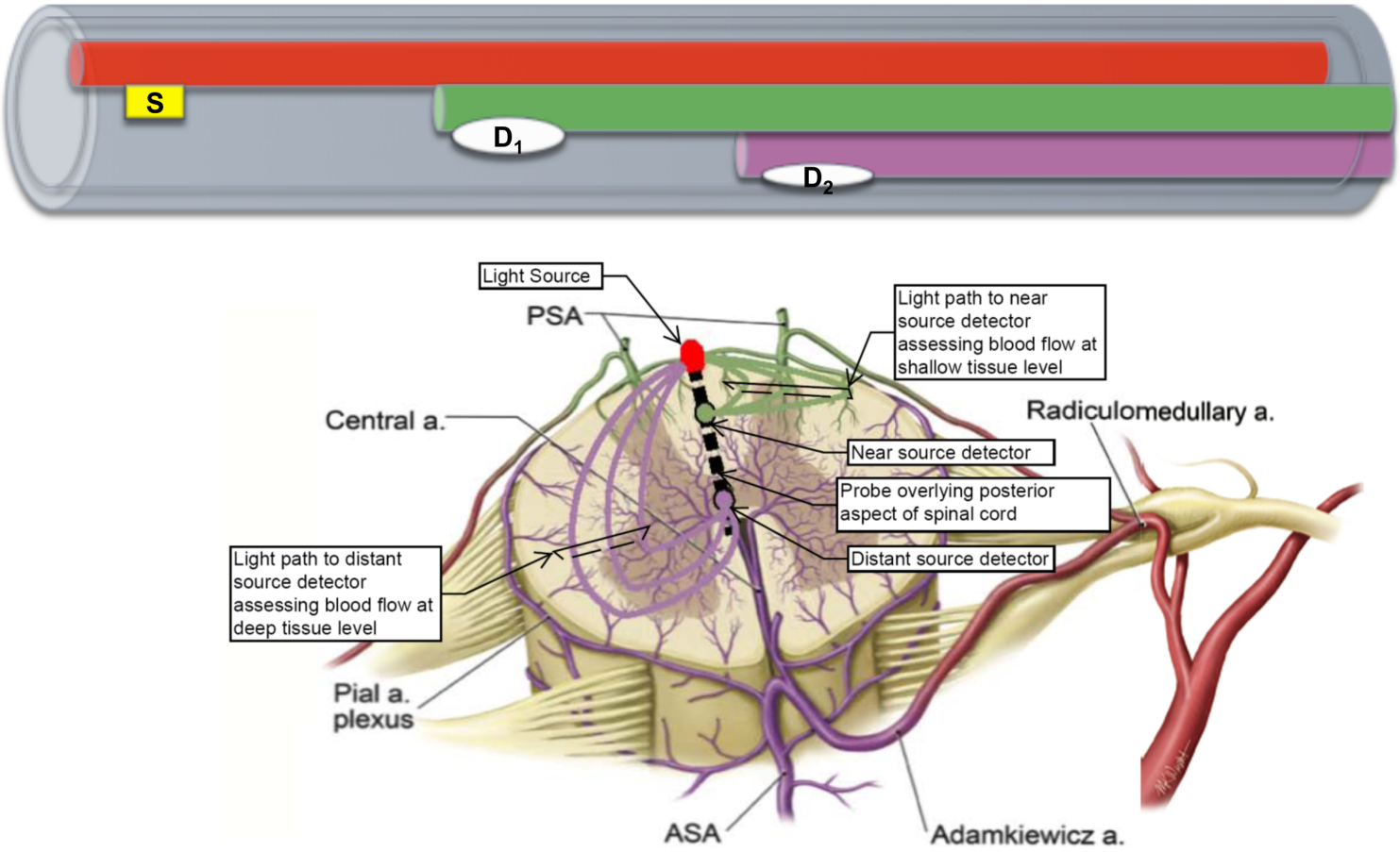

Figure 3.7: The fiber-optic probe consists of one source (S) and two detectors at a separation of 1.0 cm (D1) and 2.0 cm (D2) from the source. The probe is placed overlying the posterior aspect of the spinal cord and can interrogate tissue depth of ≈ 0.4 – 1.0 cm. The detector closer to the source (D1, represented in green) interrogates more shallow tissues (bias toward posterior cord), while the farther detector (D2, represented in purple) measures blood flow in deeper tissues (bias toward anterior cord). ASA = Anterior Spinal Artery; PSA = Posterior Spinal Artery. (Illustration showing vascularization of the lumbar spinal cord is modified and used with permission from Dr. Nicholas Theodore, MD, Barrow Neurological Institute).

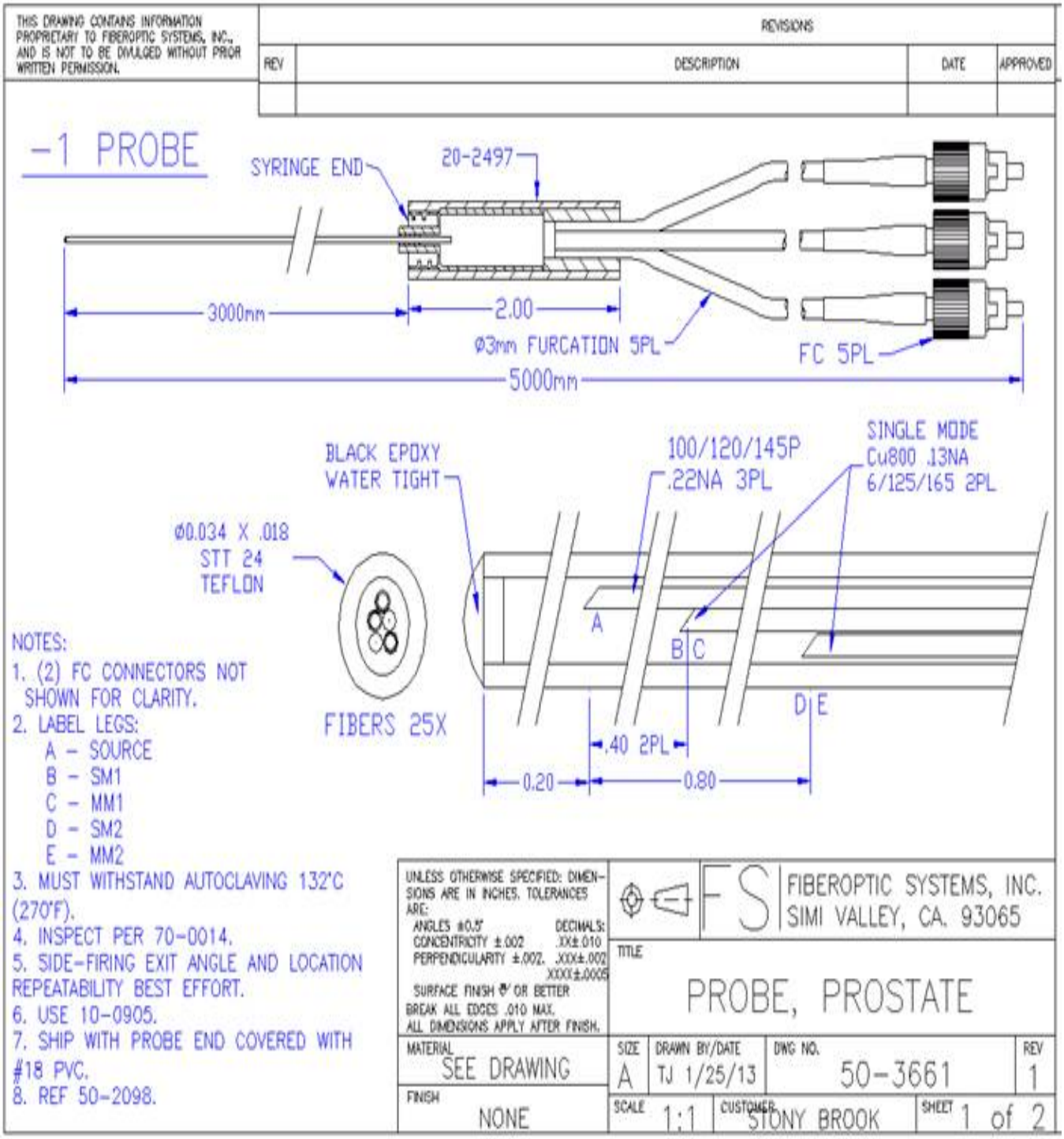

Figure 3.8: CAD drawing of the fiber optic probe design with source-detector separations of 1.0 cm and 2.0 cm

Chapter 4

Fiber-Optic Probe Placement in Sheep Model

This chapter focuses on the different approaches for the fiber-optic probe placement in sheep. The first section elaborates on our rationale for choosing sheep as our animal model over other large animal models. Since monitoring of spinal cord hemodynamics in sheep is a novel application of the DCS/DOS monitor and the fiber-optic probe has been specifically designed for this application, the following sections provide a detailed description of the surgical procedures performed for the placement of our fiber-optic probe onto the sheep spinal cord. We also performed a set of experiments to determine if the location or method of the probe placement would affect the measured changes in spinal cord blood flow and oxygenation, the methods and results of which comprise the final parts of this chapter.

4.1. Animal Justification

Adult Dorset sheep, approximately 2 years of age and weighing 60-70 kg, were chosen as the animal model for this study. Since the fiber optic probe is approximately the same size as an epidural catheter used clinically in humans, we need an animal model with roughly the same spinal anatomy as humans. This would help us assess the safety and efficacy of probe placement since we would face similar potential for interference from surrounding tissues.

A number of reports exist for the testing of the epidural approach for anesthesia and for attempts at protecting against spinal ischemia in sheep (*144-146*) and swine (*147-149*). The vertebral processes in sheep can be palpated more easily than swine, to assist in placing the fiber optic probe percutaneously. Swine also have a more robust blood supply to the spinal cord (*150*), which makes it hard to do a comparative study The sheep and human spines are close in bony dimensions, which includes spinal canal depth and width, especially in the thoracic and lumbar spines (*151*). For both humans and sheep, canal width is greater than depth, thus producing a typically oval shape that is most pronounced in the lumbar region. The human spinal canal is wider and deeper in the antero-posterior plane than sheep (*152*); potentially inferring that safety demonstrated in the sheep model may predict at least the same, if not a greater, safety profile in a human. Sheep have 12-14 thoracic and 6-7 lumbar vertebrae. Kaplan (*153*) and Moomiaie (*154*) describe the use of the sheep model for detecting interruption of

spinal cord blood flow during aortic cross clamping. There are numerous reports of the use of the sheep model to study spinal cord injury (*155, 156*). Bockler (*157*) describes the use of a sheep model to study spinal cord ischemia after thoracic vascular surgery. The methodologies used are similar to those herein.

4.2. Methods

All animal experiments were conducted in accordance with the Institutional Animal Care and Use Committee (IACUC) guidelines. Experiments were performed under the supervision of the veterinary technicians at the Division of Laboratory Animal Resources (DLAR, Stony Brook University).

A total of fifty Dorset sheep have been used in our experiments to-date. Due to the expense of our experiments, and the “proof of concept” phase at which it currently lies, we have conducted multiple experiments in many of our sheep when scientifically appropriate.

4.2.1. Anesthetic Management

Animals were pre-treated with glycopyrrolate (.02 mg/kg, IM). Anesthesia was induced with ketamine (10-20 mg/kg IM). Sheep were intubated and anesthesia maintained with isoflurane (1.5-3.0%) through controlled ventilation or 50-200 µg/kg/min intravenous (IV) ketamine. Ketamine boluses of 2-5 mg/kg IV were sometimes used to assist with maintenance of anesthesia. Depth of anesthesia was evaluated by sheep movement, changes in heart rate, jaw tone, and response to interdigital clamping to the "first click" of a hemostat, pupil size and position, and checking for the presence of palpebral reflexes. If these reflexes were noted during surgery, anesthetic depth was increased until the reflexes were no longer present. A complete anesthetic record was maintained for each animal. Blood pressure, heart rate, pulse oximetry, temperature, and respirations were continuously monitored.

After the sheep reached a deep plane of anesthesia, paralytic agents such as Vecuronium (0.1 mg/kg, IV) or Pancuronium were used to prevent movement during procedures such as electrocautery, opening the chest for a thoracotomy, or a laminectomy (wherein the spinal laminae are removed to allow direct visualization of the underlying spinal cord tissue). Movement of the sheep during the surgical procedures due to muscle or nerve stimulation could adversely affect the experimental outcome by causing injury to the heart or spinal cord of the animals. During paralysis, heart rate and blood pressure were used to monitor the depth of anesthesia.

4.2.2. Fiber-optic Probe Placement

A posterior laminotomy was created to allow for open placement of the fiber-optic probe. After adequate general anesthesia was established, the sheep was positioned prone. A midline incision was made and a subperiosteal dissection was performed to expose the spinous processes, lamina and medial facets. A Leksell rongeur was then used to remove the intra-spinous ligaments as well as the spinous processes themselves. A thin-footed Kerrison was used to carefully remove the lamina creating a trough that was sequentially widened until the dura of the spinal cord was well seen. The probe was placed using loupe magnification and was advanced superiorly or inferiorly under intact laminae to lie within the epidural or subdural space Figure 4.1 shows the placement of the fiber optic probe after a direct laminectomy was performed.

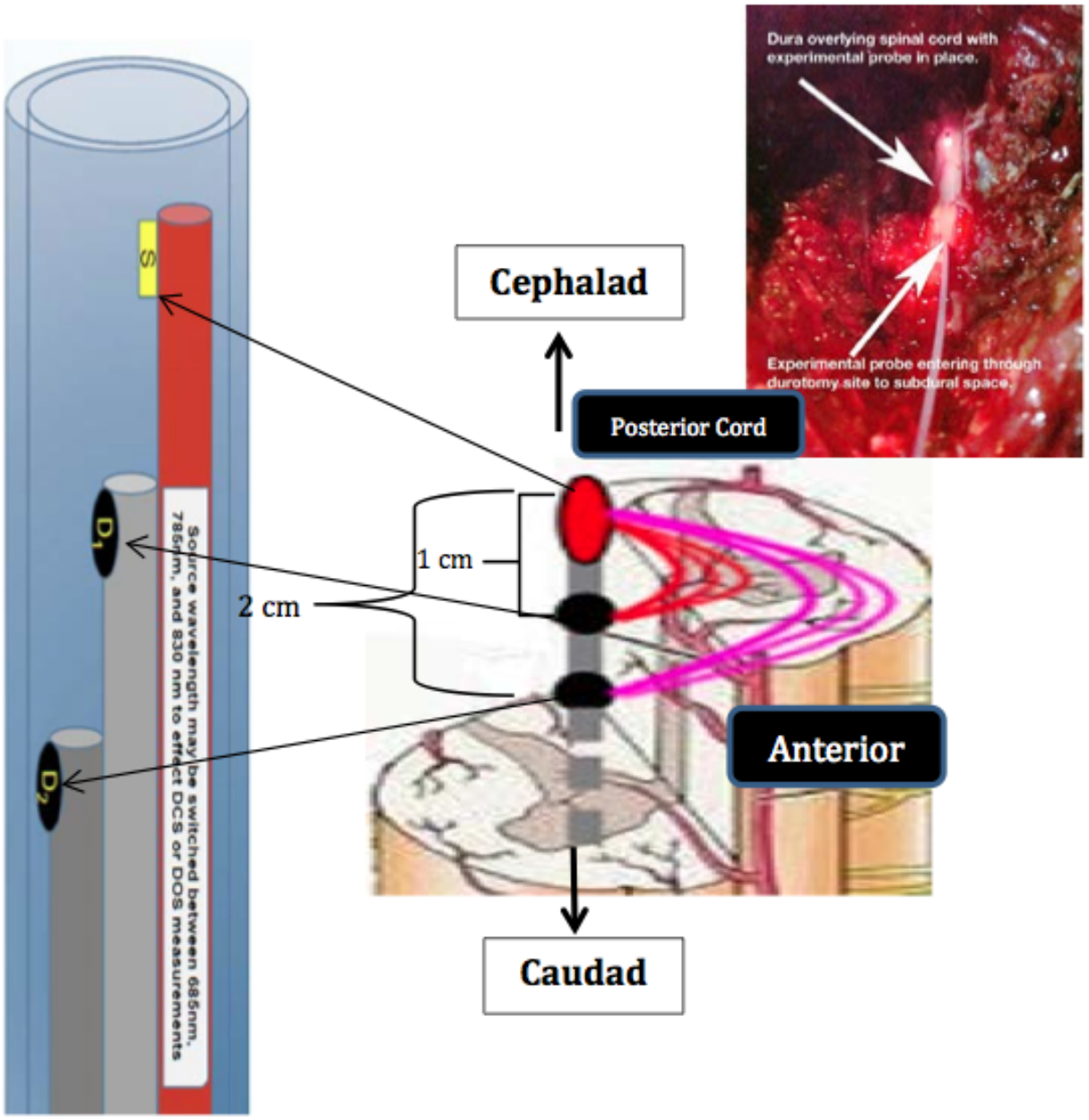

Figure 4.1: The fiber-optic probe lies upon the posterior spinal cord and is oriented form caudad to cephalad. The varied source- detector separations of 1.0 cm and 2.0 cm allows the probe to interrogate spinal cord tissue depths of ≈ 0.5 cm-1.0 cm. Smaller separations offer improved signal detection and resolution while greater separations allow interrogation of deeper tissues. Modeling of the differences in signals received between the two S- D separations can yield spatial information and may allow for spatially resolved blood flow measurements between the anterior and posterior circulations. The inset shows the probe placed in the subdural space upon the posterior cord after a laminectomy.

Percutaneous placement of the probe was achieved via 17 gauge Tuohy needle introduced in an L2-L4 lumbar interspace, with the epidural space identified by loss of resistance to air or saline. The probe was then advanced to the desired level under fluoroscopic guidance. Figure 4.2 shows the site of percutaneous placement of the fiber optic probe and its advancement to the desired vertebral level (the laminectomy site in this case). Figure 4.3 shows a fluoroscopic image (Zeego Artis, Siemens) with the site where the probe was inserted through a 17 Gauge Tuohy needle.

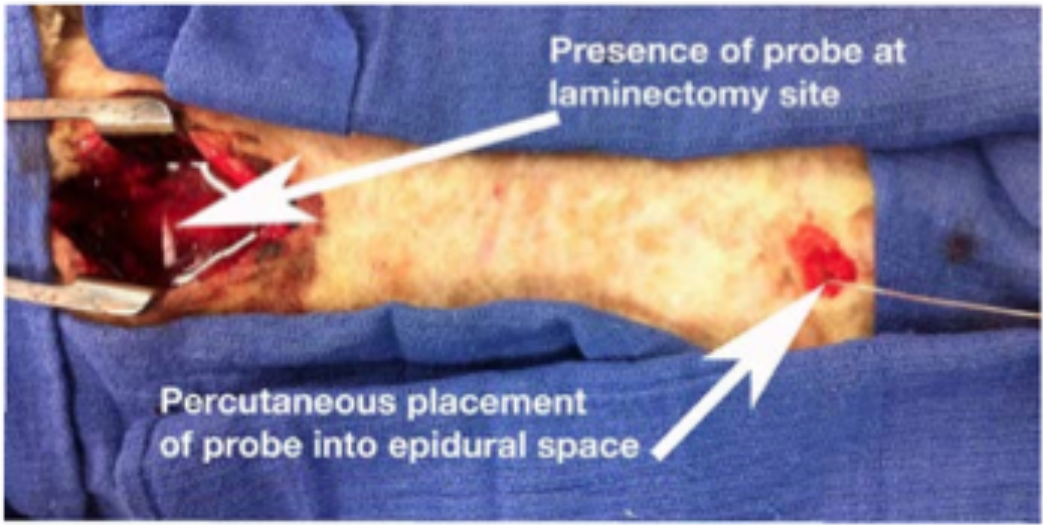

Figure 4.2: Percutaneous placement of the fiber-optic probe, which was visualized via a laminectomy in this case.

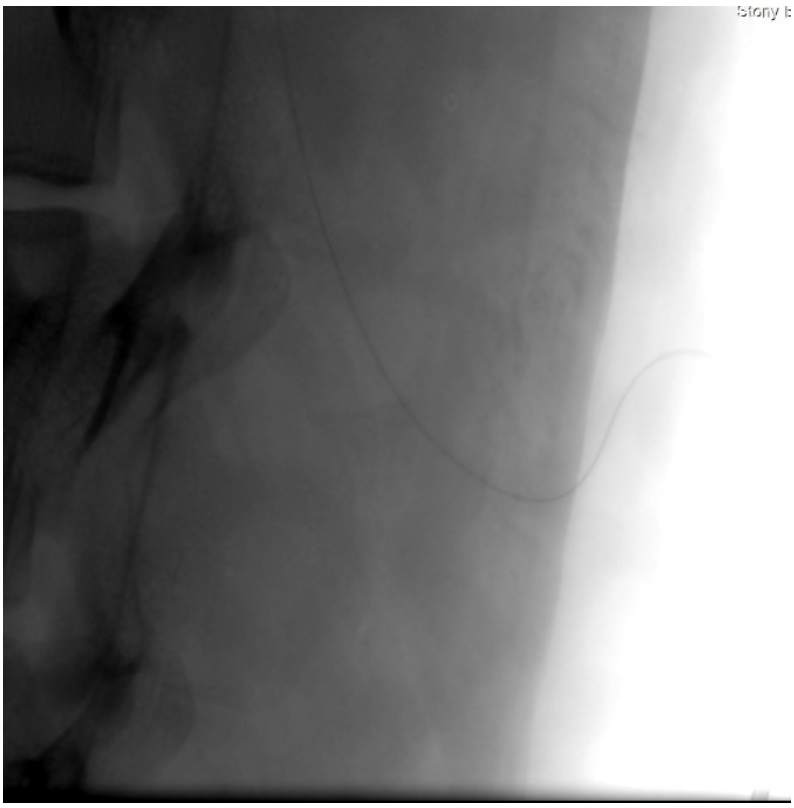

Figure 4.3: Fluoroscopic image showing the site where the probe was inserted percutaneously using a 17 Gauge Tuohy needle.

Ventilatory rate and volume, systemic oxyhemoglobin saturation (pulse oximetry), ECG, end-tidal CO_2, and MAP were continuously monitored.

4.2.3. Data Acquisition and Analysis

After adequate general anesthesia was established, the sheep was positioned supine for the placement of femoral and carotid arterial and venous cannuli to allow measurement of femoral and carotid mean arterial pressures (MAPs) using blood pressure transducers connected to a Powerlab device enabled with a LabChart monitoring software (ADInstruments, Inc., CO).

DCS/ DOS data were collected using LabView software code (National Instruments, TX). Each data acquisition cycle takes about 8 seconds, with the data cycled between the DCS module (~3 seconds) and the ISS Imagent module (~5 seconds). The laser cycles are triggered between the DCS and DOS modules via the data acquisition board (NI USB-6251 Data Acquisition Device, National Instruments, TX). The arterial monitoring and DCS/DOS data were correlated and analyzed offline using homemade Matlab scripts (Mathworks, MA).

4.2.4. Statistical Analysis

The changes due to the various pharmacological and mechanical interventions were calculated from the highest or lowest blood flow and oxygenation value in the time-course during the intervention period. For each intervention, mean change and standard deviation were calculated by averaging over all trials and animals. Non-parametric Wilcoxon rank sum test was used to compare the hemodynamic changes measured by the optical monitor and fiber-optic probe with the different placement techniques (direct placement through a laminectomy in the epidural or subdural space and percutaneous placement through a Tuohy needle in the epidural space). All statistical analysis was performed using JMP Statistical Software (SAS Institute, NC).

4.3. Results

This section describes the results obtained upon comparing the fiber-optic probe placement approaches, i.e. directly visualized placement through a laminectomy and percutaneous placement through a Tuohy needle that is confirmed fluoroscopically. Next, we also discuss the results obtained upon comparing the fiber-optic probe placement locations, i.e. placement in the epidural space of the sheep spinal cord versus the subdural space of the sheep spinal cord.

4.3.1. Direct versus Percutaneous Placement

In this set of experiments, we tested the feasibility of using the probe placed in different positions on the spinal cord and the ability to place it via different approaches. The fiber optic probe was placed via laminotomy (n=6) or via percutaneous (n=11) approaches into the epidural space. Since the potential clinical placement of the probe would be after a laminectomy or laminotomy for spine surgery and percutaneously for aortic surgery, we tested the device's capability to accurately measure spinal cord hemodynamics through both probe placement techniques. We placed the linear probe 1) under direct visualization, by performing a lower thoracic/ upper lumbar posterior laminectomy (surgical details in section 4.2.2.), for the direct placement of the probe upon the posterior cord within the epidural space, and 2) percutanously into the epidural space through a 17 Gauge Tuohy needle positioned at the lumbar spine, and advancing

the probe caudally into the thoracic region (probe position was confirmed using fluoroscopic guidance). At each position, and using both direct (n=6) and percutaneous (n=11) approaches, we performed identical pharmacological and ischemic interventions and compared the difference in blood flow and oxygenation changes detected by the probe. Pharmacological interventions involved administering bolus injections of hypertensive drugs (vasopressors) to increase the spinal cord blood flow and oxygenation and hypotensive drugs (vasodilators), which decrease the spinal cord blood flow and oxygenation. Ischemic interventions involved clamping or occluding the proximal descending thoracic aorta to cut off blood supply to the spinal cord and thus cause a decrease in spinal cord blood flow/oxygenation.

Changes in blood flow and oxygenation measured by the optical monitor after placing the probe either percutaneously or directly agreed with the expected changes for each intervention performed. These changes correlated with the femoral and carotid MAP changes observed. Changes observed after either direct or percutaneous placement approaches were not statistically different ($p = 0.65$). Figure 4.4 shows a representative example of spinal cord blood flow changes measured by DCS, wherein the probe was placed directly into the epidural space (top image) or percutaneously into the epidural space (bottom image). Hypotension, and thus a decrease in spinal cord blood flow, was induced by administering 400 µg boluses of nitroprusside (black arrows) at regular intervals. The expected decrease in the spinal cord blood flow was measured after both placement approaches, indicating that the method of probe placement would not affect the spinal cord blood flow and oxygenation changes measured by the monitor.

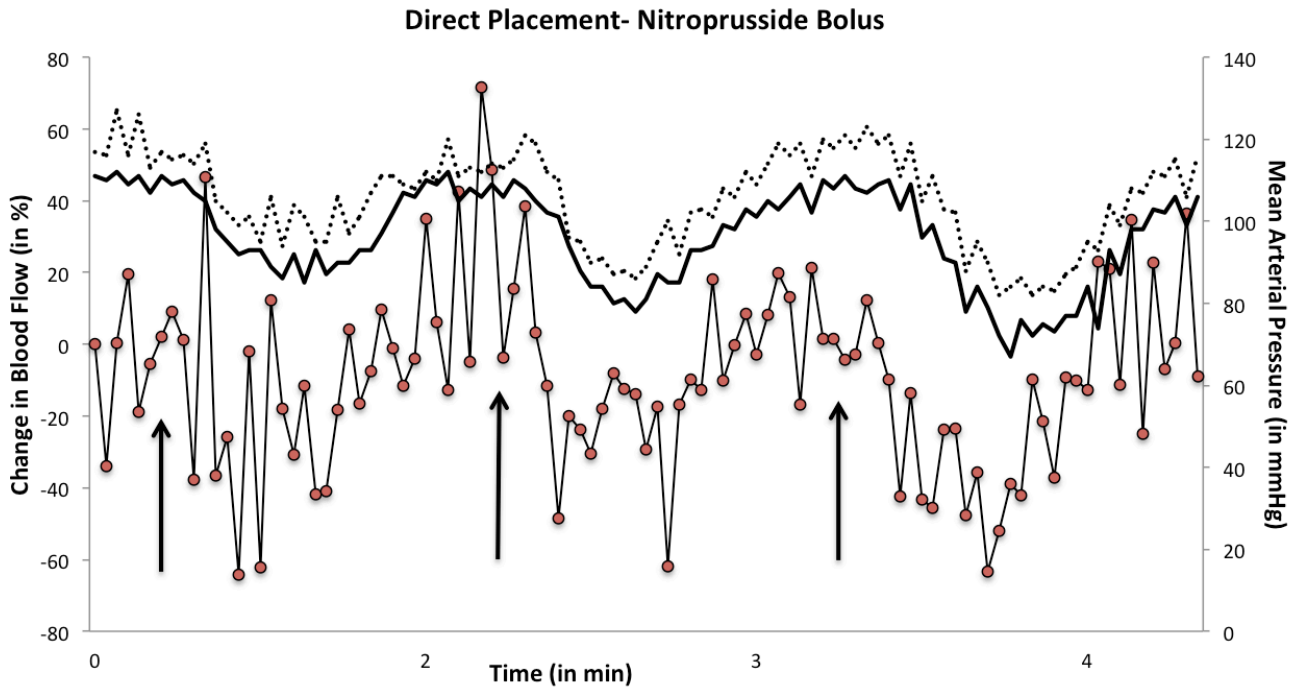
Direct Placement- Nitroprusside Bolus
Change in Blood Flow (in %)
Mean Arterial Pressure (in mmHg)
Time (in min)
80
60
40
20
0
-20
-40
-60
-80
140
120
100
80
60
40
20
0
0
2
3
4

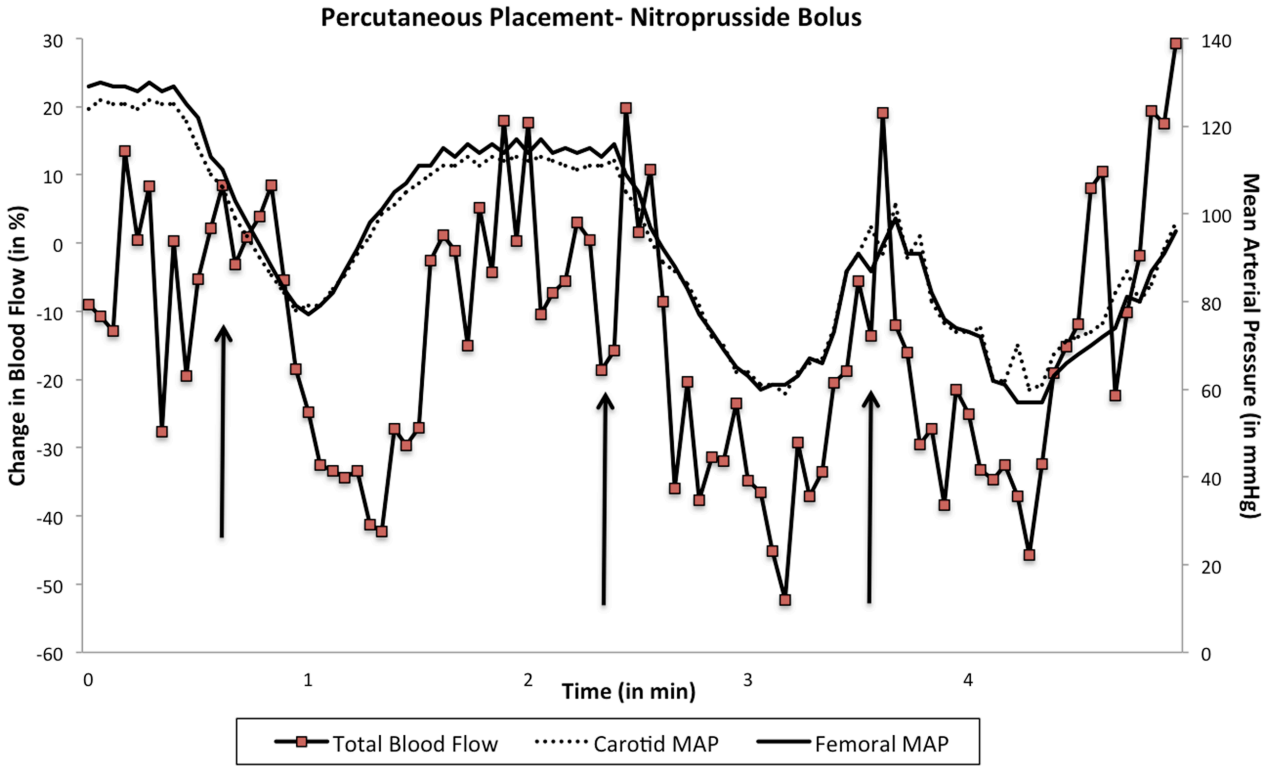

Figure 4.4: A representative example of the decrease in spinal cord blood flow measured by the DCS technique upon administration of a hypotensive drug, 400 µg Nitroprusside bolus (black arrows), at regular intervals. The probe was placed both directly after a laminectomy into the epidural space (top) and percutaneously into the epidural space (bottom). Decrease in the Femoral and Carotid MAPs correlated with the decrease in blood flow whenever a bolus was administered. The X-axis represents the time taken in minutes to detect a change in spinal cord blood flow or mean arterial pressure; the primary Y-axis represents the change in blood flow in per cent detected by DCS; the secondary Y-axis represents the change in femoral and carotid mean arterial pressure in mmHg detected by the Powerlab device.

4.3.2. Epidural versus Subdural Placement

In this set of experiments, we tested if the presence of the dural matter would have an effect on the measurement of spinal cord blood flow and oxygenation concentration changes. The fiber-optic probe was placed either 1) on the posterior spinal cord within the subdural space (the space below the dural matter) directly after performing a posterior laminectomy as described in section 4.2.2., or 2) on the posterior spinal cord within the epidural space (the space above the dural matter), either directly through a laminectomy or percutaneously through a 17 Gauge Tuohy needle.

For all the different interventions (n = 17), spinal cord blood flow measured at the epidural position was not statistically different from the flow measured at the subdural position ($p = 0.87$). Measurements in both positions yielded similar blood flow and oxygenation results for each specific intervention. Femoral and carotid MAPs measured by the PowerLab device correlated well with the changes in blood flow and oxygenation measured by the DCS/DOS monitor. Figure 4.5 shows a representative example of spinal cord blood flow changes measured by DCS, wherein the probe was placed in the subdural space (top image) or the epidural space (bottom image). Hypertension, and thus an increase in spinal cord blood flow, was induced by administering 400 µg boluses of phenylephrine (red arrow) and 4 units of vasopressin (black arrow). The expected increase in the spinal cord blood flow was measured at both the epidural and subdural positions.

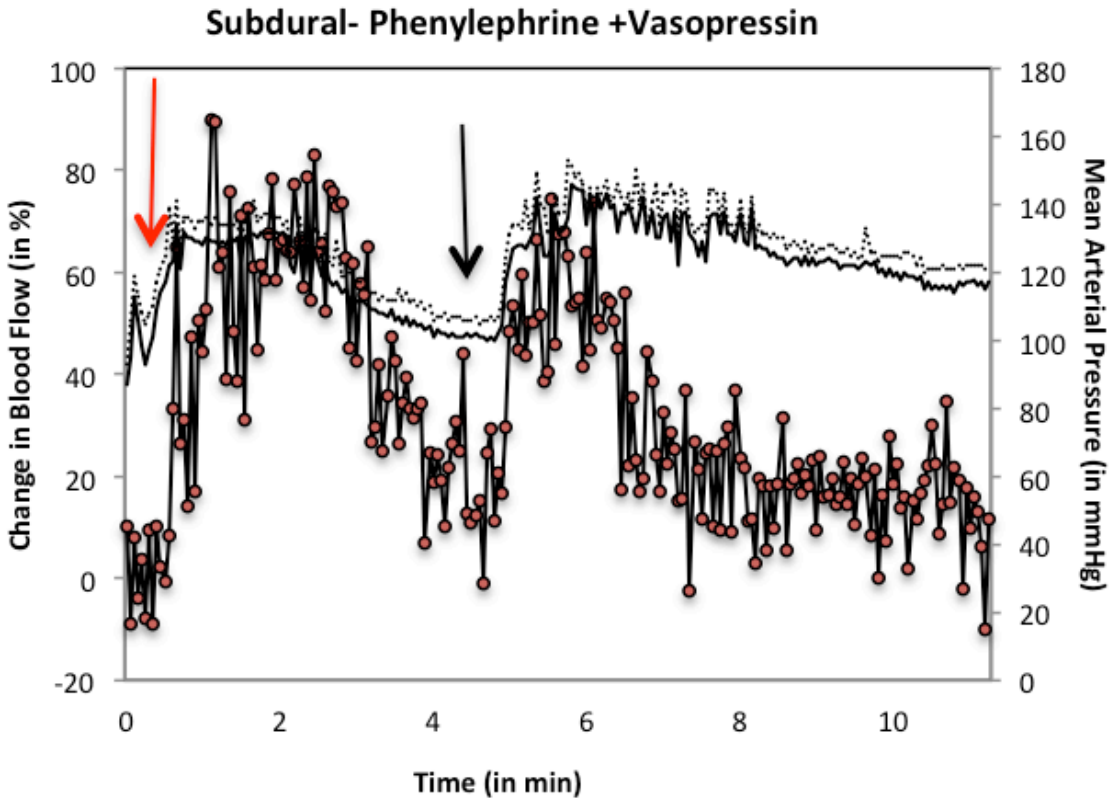
Subdural- Phenylephrine +Vasopressin
Change in Blood Flow (in %)
Mean Arterial Pressure (in mmHg)
Time (in min)
100
80
60
40
20
0
-20
180
160
140
120
100
80
60
40
20
0
0
2
4
6
8
10

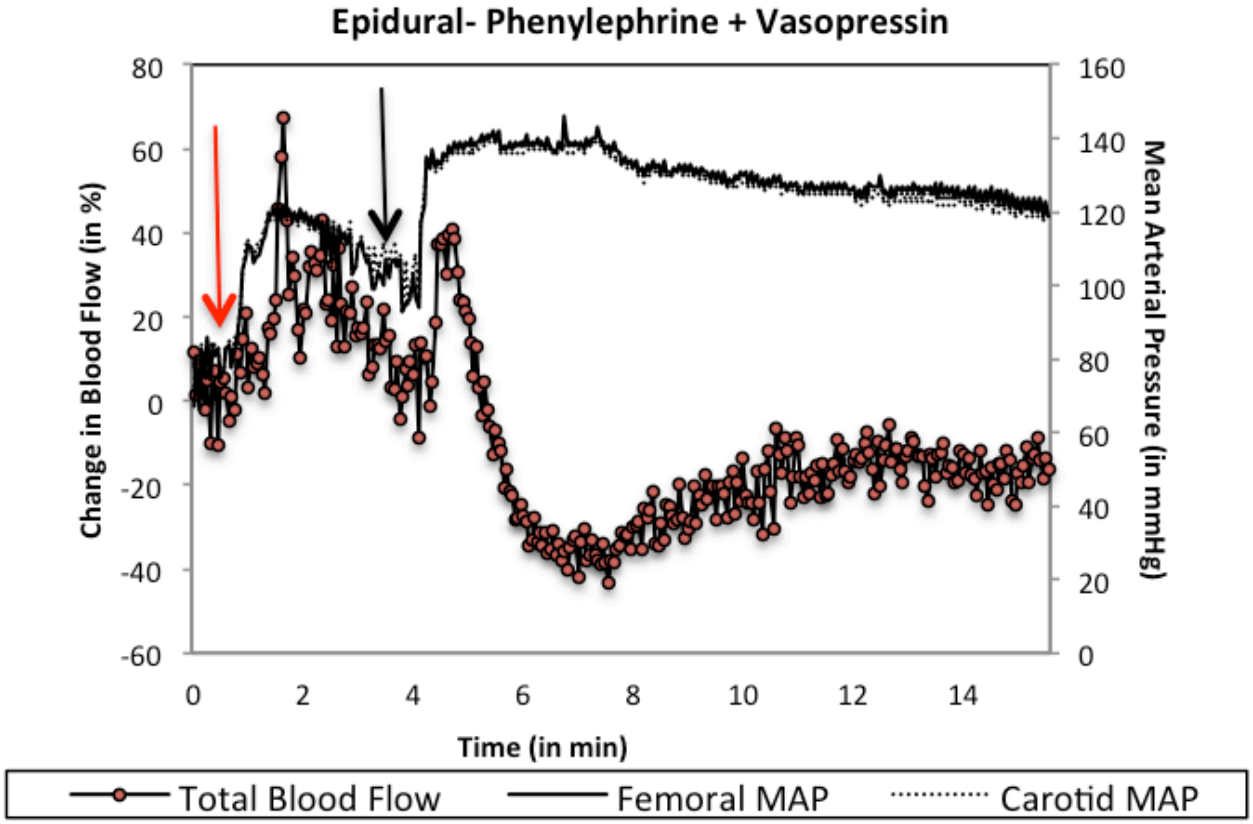

Figure 4.5: A representative example of increase in spinal cord blood flow measured by the DCS technique upon administration of hypertensive drugs: first, a 400 µg Phenylephrine bolus (red arrow), followed by a bolus of 4 units of Vasopressin (black arrow). The probe was placed in both the subdural space (top) and epidural space (bottom) under direct vision after performing a posterior laminectomy. Increase in Femoral and Carotid mean arterial pressures correlated with the increase in blood flow upon injecting boluses of phenylephrine and vasopressin. The X-axis represents the time taken in minutes to detect a change in spinal cord blood flow or mean arterial pressure; the primary Y-axis represents the change in blood flow in per cent detected by DCS; the secondary Y-axis represents the change in femoral and carotid mean arterial pressure in mmHg detected by the Powerlab device.

4.4. Discussion

Since different surgical approaches would require the fiber-optic probe placement in different locations (subdural or epidural) and through different placement techniques (through a laminectomy or percutaneously through a minimally invasive technique), the above set of experiments prove an important point: the placement technique or the presence of the dural matter does not affect the blood flow and oxygenation concentration changes measured by the DCS/DOS device. This increases the versatility of our optical monitor, making it more appealing to a vast variety of surgeons and enabling its use for multiple surgical applications. For example, surgical procedures for the correction of scoliosis, removal of spinal cord tumors and stabilization of spinal cord trauma injuries often require a laminectomy and surgeons would prefer to place the probe directly onto the spinal cord in these situations. Cases involving repair of thoracoabdominal aneurysms, on the other hand, would be better suited with a minimally invasive approach for probe placement, such as through a 17 Gauge Tuohy needle into the epidural space of the spinal cord.

Furthermore, since the percutaneous placement approach has been routinely used in clinical practice to place cerebrospinal fluid drains and epidural catheters, and carries an excellent safety profile, we anticipate that our fiber-optic probe could be placed safely and minimally invasively, without causing any damage to the spinal cord.

Chapter 5

Testing of the Optical Monitor

This chapter focuses on testing the sensitivity of the optical monitor and fiber optic probe. In these experiments, sensitivity is defined as the ability to detect acute changes in spinal cord blood flow and oxygenation associated with pharmacological, physiologic, and mechanical interventions in the sheep model.

Pharmacological drugs such as vasopressors and vasodilators are physiologically known to increase and decrease the mean arterial pressure respectively, thereby increasing/decreasing the spinal cord blood flow and oxygenation. Turning off the ventilator for five minutes, i.e. creating a breath hold, is known to induce hypercarbia and hypoxia, resulting in an increase in spinal cord blood flow and a decrease in oxygenation concentration. We tested if the fiber-optic probe and optical monitor we have developed can indeed accurately detect these induced physiological changes.

By mechanically occluding the aorta through clamping or inflating a balloon in the proximal descending thoracic aorta, we would expect the spinal cord blood flow and oxygenation in the sheep to decrease. Furthermore, clamping the aorta would make

the spinal cord blood supply dependent only on vertebral sources above the level of clamping and as we move farther down the spinal cord and away from the vertebral sources of blood supplying the cord, we would expect a trend where the spinal cord blood flow and oxygenation would decrease progressively. The sensitivity of our device in detecting these blood flow and oxygenation changes in the sheep spinal cord will also be monitored.

5.1. Pharmacological Interventions: Hypertension and Hypotension

In these studies, certain pharmacological drugs with known physiological effects were administered in the sheep to test the hypothesis that the optical monitor and fiber optic probe would be capable of successfully and immediately detecting changes in spinal cord blood flow and oxygenation in sheep.

Vasopressors cause vasoconstriction (contraction of the blood vessels), thereby increasing the blood pressure and blood flow. Phenylephrine and Vasopressin were the vasopressors we used in our experiments to induce hypertension in the sheep, thereby raising the spinal cord blood flow and oxygenation. We hypothesized that the optical monitor and fiber-optic probe would successfully detect the increase in spinal cord blood flow and oxygenation upon administering a bolus of the vasopressor drugs.

Vasodilators dilate the blood vessels, decreasing the blood pressure and causing hypotension and a decrease in blood flow and oxygenation. We hypothesized that the DCS/DOS device would immediately detect a decrease in the spinal cord blood flow and oxygenation in the sheep upon administering a bolus of the vasodilator Nitroprusside.

5.1.1. Methods

Acute hypertension was induced via boluses of phenylephrine and vasopressin in fourteen sheep. Boluses of phenylephrine (200 μg – 600 μg) or vasopressin (4 units) were given to the sheep intravenously. Similarly, acute hypotension was induced via 400 μg boluses of the vasodilator nitroprusside in ten sheep.

The changes due to the various pharmacological interventions were calculated from the highest or lowest blood flow and oxygenation value in the time course during the intervention period. For each intervention, mean change and SD were calculated by averaging over all trials and animals. Nonparametric Wilcoxon signed-rank tests were used to assess whether there was a statistically significant difference between the observed blood flow/oxygenation changes from those at baseline.

5.1.2. Results

Changes in blood flow and oxyhemoglobin concentration were detected in all the cases where pharmacological interventions were performed to elicit acute hypertension (65 of 65 trials) and hypotension (48 of 48 trials).

Acute hypertension, elicited *via* 400 µg boluses of phenylephrine or vasopressin, resulted in an expected transient increase in spinal cord blood flow (+48 ± 21%, n = 65 interventions) and oxyhemoglobin concentration (+4 ±2 %, n = 13 interventions). A representative example of increase in blood flow and oxygenation in one trial is shown in figure 5.1. A brief hyperemic response followed in all cases. Spinal cord blood flow and oxygenation changes measured by DCS and DOS closely paralleled the changes in femoral and carotid MAPs.

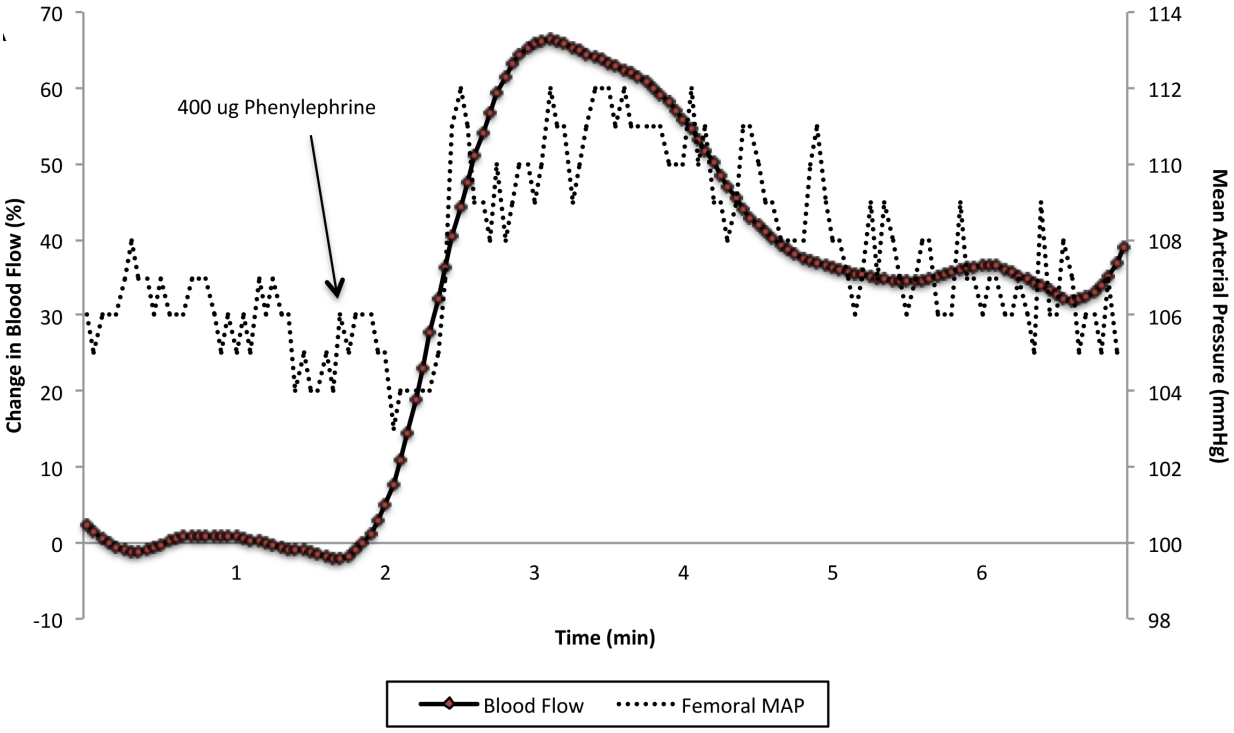

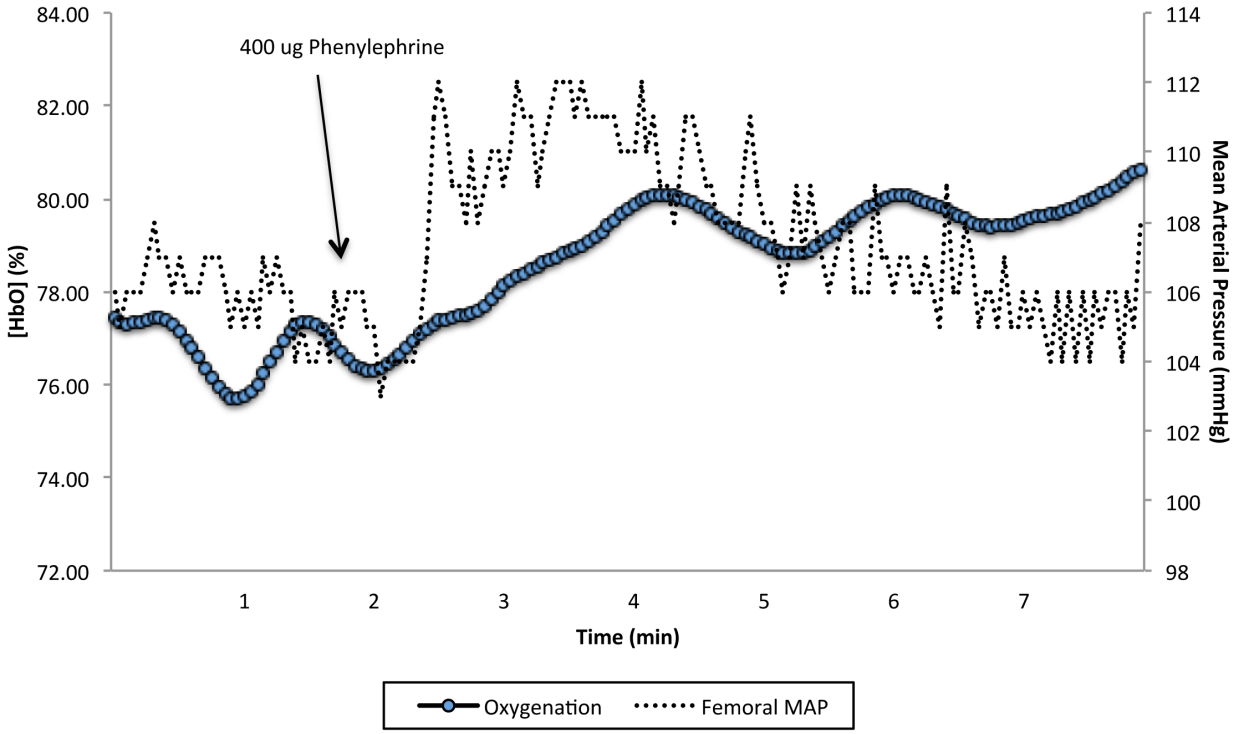

Figure 5.1: A representative example showing the increase in spinal cord blood flow (top) and oxygenation (bottom) detected by DCS and DOS respectively upon inducing hypertension in a single sheep via the administration of a 400 µg bolus of the vasopressor phenylephrine. In this example, the peak blood flow increase was ~ 65% and peak oxygenation increase was ~ 4%. Both increase in spinal cord blood flow and oxygenation paralleled increase in the femoral mean arterial pressure. Top: The X-axis represents the time taken in minutes to detect a change in spinal cord blood flow or mean arterial pressure; the primary Y-axis represents the change in blood flow in percent detected by DCS; the secondary Y-axis represents the change in femoral mean arterial pressure in mmHg detected by the Powerlab device. Bottom: The X-axis represents the time taken in minutes to detect a change in spinal cord oxyhemoglobin concentration or mean arterial pressure; the primary Y-axis represents the change in oxyhemoglobin concentration in percent detected by DOS; the secondary Y-axis represents the change in femoral mean arterial pressure in mmHg detected by the Powerlab device.

Hypotension, elicited *via* bolus of nitroprusside (400 µg), resulted in the expected decrease in blood flow (−48 ± 11%, n = 48 interventions) and oxyhemoglobin (−6 ± 1%, n = 9 interventions). A representative example of the decrease in spinal cord blood flow and oxygenation upon administration of a nitroprusside bolus in a single trial is shown in figure 5.2. These changes were followed by brief hyperemic responses. Decrease in spinal cord blood flow and oxygenation measured by DCS/DOS closely paralleled decrease in femoral and carotid MAPs.

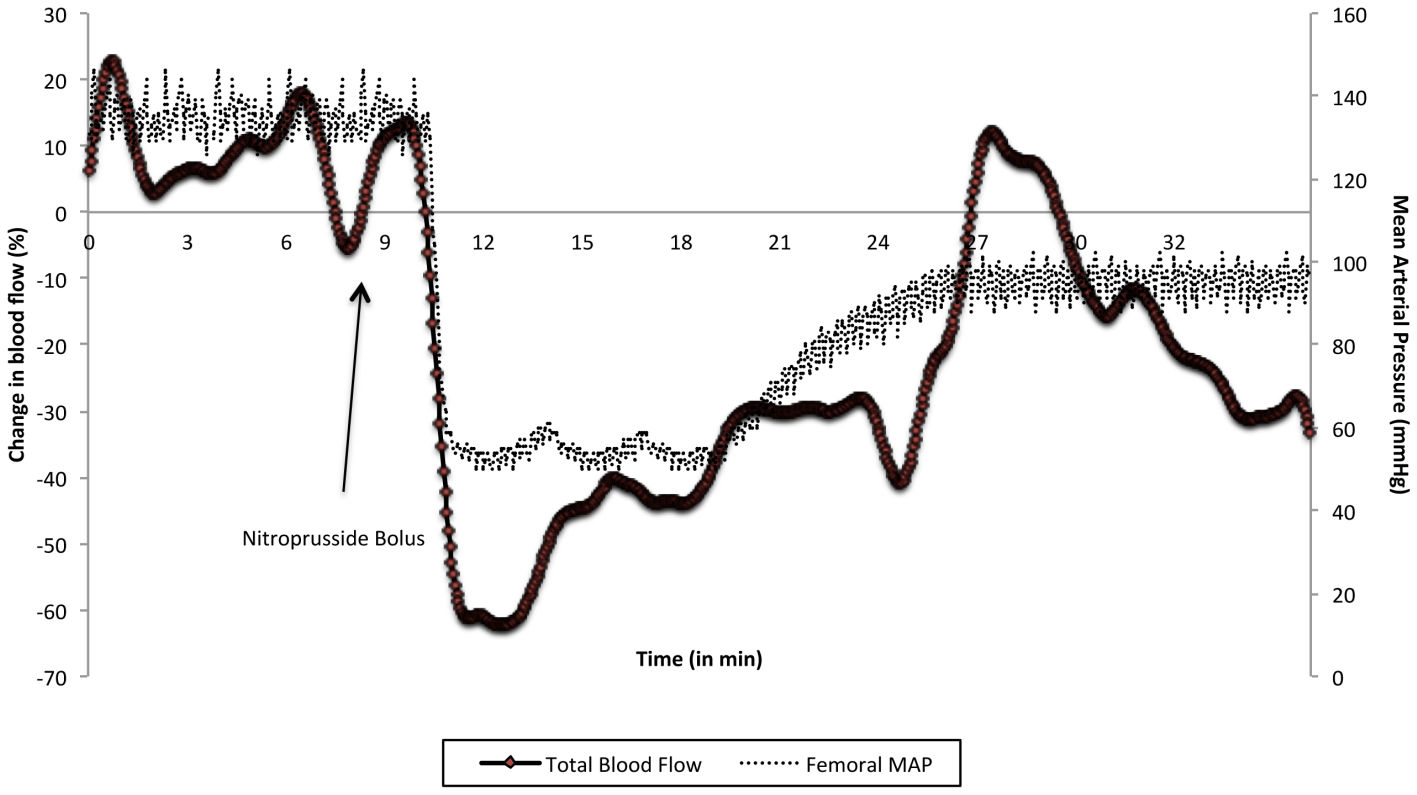

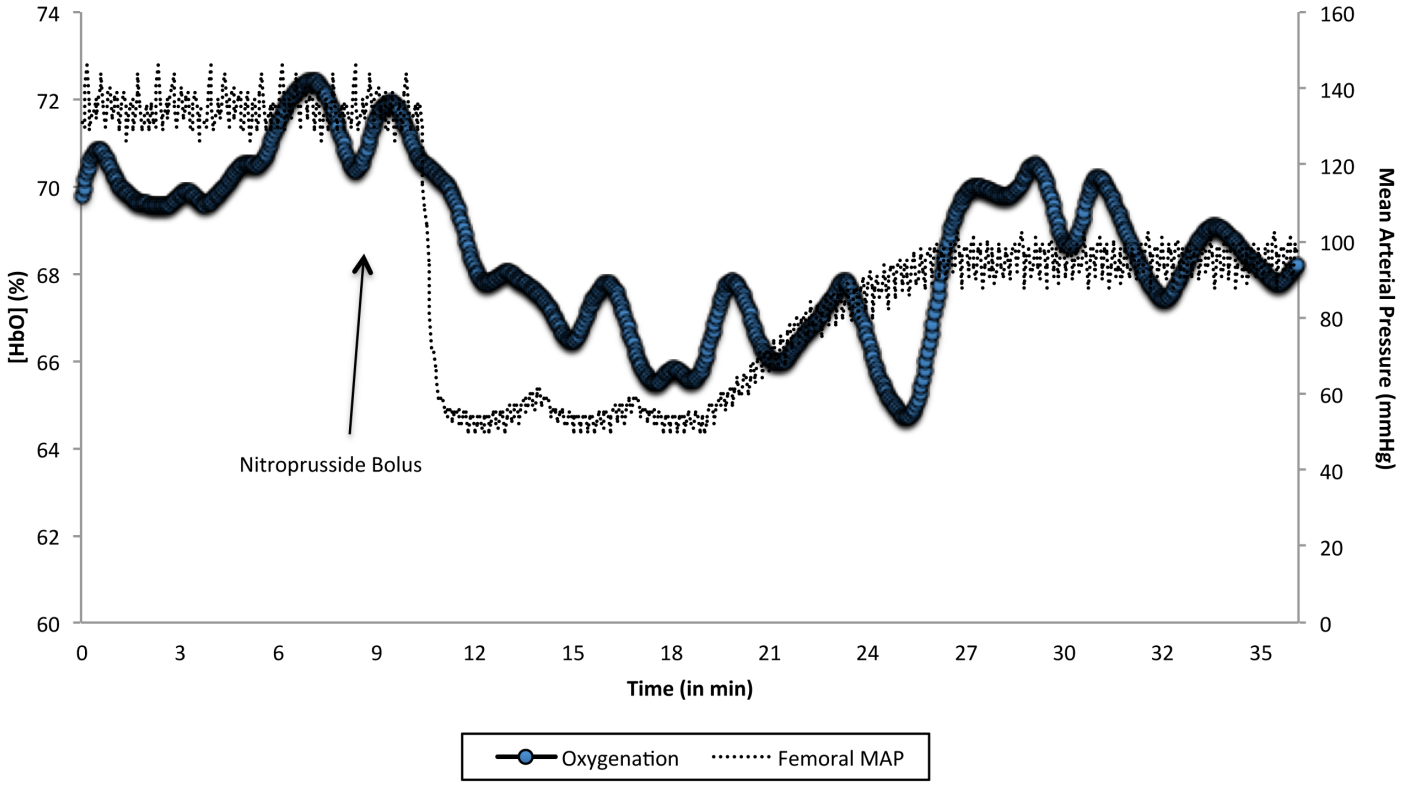

Figure 5.2: A representative example showing the decrease in spinal cord blood flow (top) and oxygenation (bottom) detected by DCS and DOS respectively upon inducing hypotension in a single sheep via the administration of a 400 µg bolus of the vasodilator nitroprusside. In this example, the peak blood flow decrease was ~ 75% and peak oxygenation decrease was ~ 7%. Decrease in spinal cord blood flow and oxygenation closely paralleled the decrease in femoral mean arterial pressure. Top: The X-axis represents the time taken in minutes to detect a change in spinal cord blood flow or mean arterial pressure; the primary Y-axis represents the change in blood flow in percent detected by DCS; the secondary Y-axis represents the change in femoral mean arterial pressure in mmHg detected by the Powerlab device. Bottom: The X-axis represents the time taken in minutes to detect a change in spinal cord oxyhemoglobin concentration or mean arterial pressure; the primary Y-axis represents the change in oxyhemoglobin concentration in percent detected by DOS; the secondary Y-axis represents the change in femoral mean arterial pressure in mmHg detected by the Powerlab device.

5.1.3. Discussion

The fiber-optic probe and monitoring device reliably detected spinal cord responses to pharmacologic interventions designed to induce hypertension and hypotension. The detected responses were in line with published data (*158*). Boluses of hypertensive agents, namely phenylephrine and vasopressin, created brief periods of hypertension, which were accompanied by brief increases in spinal cord blood flow and oxygenation. Boluses of the hypotensive agent nitroprusside produced brief periods of hypotension and corresponding decrement in spinal cord blood flow and oxygenation. The changes were followed by rapid autoregulation back to baseline, as would be expected for neural tissue such as the brain (*159, 160*) and spinal cord (*161*). The responses to all interventions were robust, immediate, and reproducible. In all cases, changes in flow were more immediately responsive than changes in oxygenation. With hypotension, changes in blood pressure and blood flow always preceded slower changes in oxygenation. With hypertension, since oxyhemoglobin saturation is already near maximal, we expected that there would only be a marginal increase detected by DOS. This was supported in the oxygenation concentration results across all trials in the sheep where hypertensive drugs were administered (n = 65 interventions). Vasopressors and vasodilators are often administered to patients in the operating room to prevent hypotension and hypertension respectively. The ability of the DCS/DOS device to immediately detect the changes in spinal cord blood flow and oxygenation upon administration of these drugs could therefore be highly useful during surgical procedures in the operating room.

5.2. Physiological Interventions: Systemic Hypoxia

Respiratory arrest is characterized by inadequate blood oxygenation (systemic hypoxia) and excess carbon dioxide in the blood (hypercarbia). For these sets of experiments, we turned off the ventilator, creating respiratory arrest and therefore inducing systemic hypoxia and hypercarbia in three sheep. This is known to lead to a decrease in tissue oxygen saturation and an increase in the blood flow. The systemic hypoxia due to respiratory arrest would not physiologically affect the femoral and carotid MAPs. We hypothesized that the optical monitor would be able to detect the increase in blood flow and decrease in oxyhemoglobin concentration caused by the induction of hypoxia and hypercarbia in the sheep.

5.2.1. Methods

Systemic hypoxia and hypercarbia were created in three sheep via respiratory arrest; achieved by turning off the ventilator until the systemic hemoglobin saturation reached approximately 80%, as measured by a pulse oximeter.

5.2.2. Results

Hypoxia and hypercarbia, elicited via respiratory arrest, resulted in an increase in blood flow (84 ± 22%, n = 4 interventions) and decrease in oxygenation (−9 ± 6%, n = 4 interventions). A representative example is shown in the figure 5.3 below. Changes in blood flow and oxygenation concentration were detected in all four trials wherein hypoxia was induced. No changes were observed in femoral and carotid MAPs by the Powerlab device.

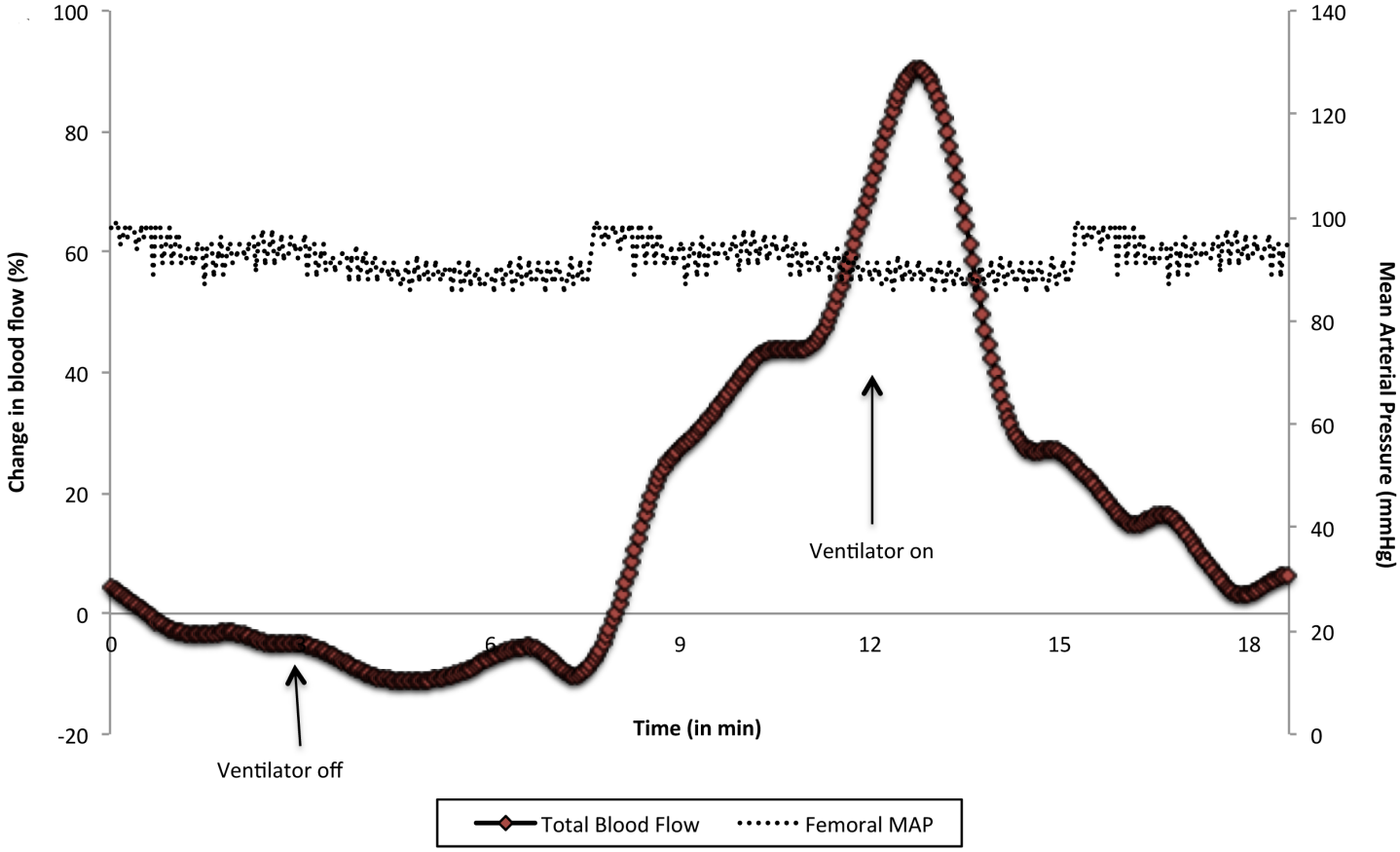

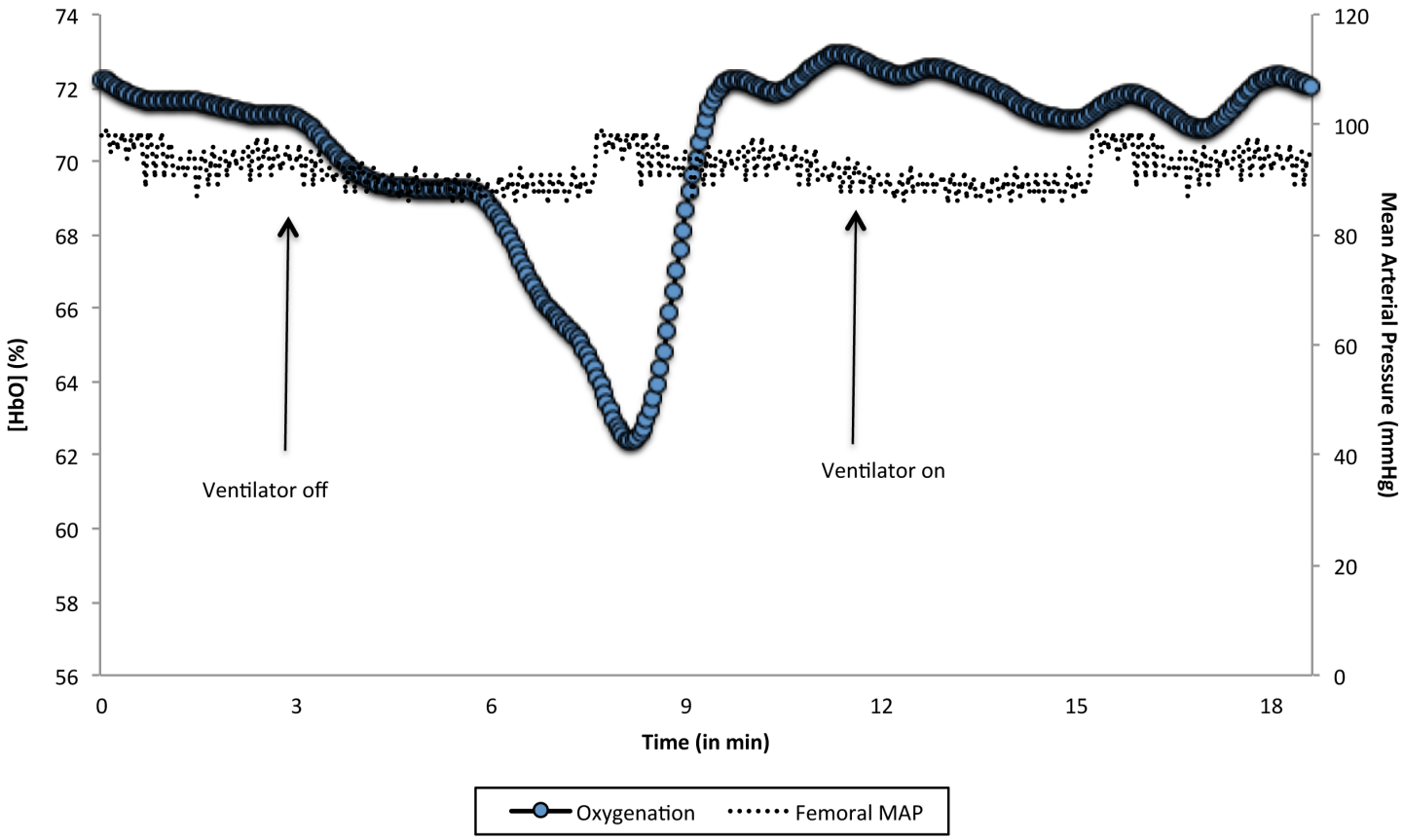

Figure 5.3: A representative example showing the increase in spinal cord blood flow (top) and decrease in oxygenation (bottom) detected by DCS and DOS respectively upon inducing hypoxia in a single sheep via respiratory arrest. In this example, the peak blood flow increase was ~ 90% and peak oxygenation decrease was ~ 8%. No change was observed in femoral mean arterial pressure. Top: The X-axis represents the time taken in minutes to detect a change in spinal cord blood flow or mean arterial pressure; the primary Y-axis represents the change in blood flow in percent detected by DCS; the secondary Y-axis represents the change in femoral mean arterial pressure in mmHg detected by the Powerlab device. Bottom: The X-axis represents the time taken in minutes to detect a change in spinal cord oxyhemoglobin concentration or mean arterial pressure; the primary Y-axis represents the change in oxyhemoglobin concentration in percent detected by DOS; the secondary Y-axis represents the change in femoral mean arterial pressure in mmHg detected by the Powerlab device.

5.2.3. Discussion

With respiratory arrest, hypercarbia precedes the occurrence of hypoxia, eliciting a gradual increase in flow and much slower fall in oxygenation. The fiber-optic probe and optical monitoring device reliably detected the increase in spinal cord blood flow and decrease in oxyhemoglobin concentration upon the induction of hypoxia and hypercarbia, via respiratory arrest, in three sheep. The changes corresponded with the onset of respiratory arrest, i.e. when the systemic hemoglobin saturation reached approximately 80%, as detected by a pulse oximeter. The results from these experiments further supported the capability of the optical monitor to immediately, reliably and accurately detect changes in the blood flow and oxygenation of the spinal cord.

5.3. Mechanical Interventions: Aortic Occlusion

In the following set of experiments, the sensitivity of the DCS/DOS device in detecting changes in spinal cord blood flow and oxygenation associated with aortic occlusion was characterized in fourteen sheep. Occluding the proximal descending thoracic aorta would cut off the blood supply to levels below the aorta, thus leading to a decrease in the amount of blood flow and oxygenation to the spinal cord. We therefore hypothesized that the DCS/DOS monitor would detect a decrease in spinal cord blood flow and oxygenation upon aortic occlusion.

5.3.1. Methods

In order to occlude the proximal descending thoracic aorta, a surgical procedure known as a thoracotomy was performed in the anesthetized sheep (refer to section 4.2.1. in chapter 4 for details on the anesthetic management), wherein the chest wall was opened through surgery to gain access to the aorta. Once a deep plane of anesthesia was achieved, paralytic agents such as Vecuronium (0.1 mg/kg, IV) or Pancuronium were used to prevent movement during the thoracotomy. Movement of the sheep during the thoracotomy, due to muscle or nerve stimulation, could adversely affect the experimental outcome by causing injury to the heart of the animals. During paralysis, the heart rate and blood pressure were used to monitor the depth of anesthesia.

In fourteen sheep, spinal cord ischemia was elicited through occlusion of the proximal descending thoracic aorta either by inflation of an intra-aortic balloon (Cook Medical, USA) or by clamping the aorta after a thoracotomy. Aortic occlusion was confirmed fluoroscopically *via* direct visual inspection through the open chest and *via* loss of femoral arterial pressure; aortic occlusion was maintained for five minutes. Completeness of aortic occlusion was confirmed by hypotension recorded in the femoral artery and hypertension recorded in the carotid artery.

5.3.2. Results

During aortic occlusion, spinal cord blood flow and oxygenation decreased immediately in response to occlusion by −65 ± 32% (n = 38) and −17 ± 13% (n = 17), respectively. Aortic unclamping resulted in a hyperemic flow and oxygenation response. A representative example of the decrease in spinal cord blood flow and oxygenation upon aortic occlusion is shown in figure 5.4. Aortic occlusion resulted in a decrease in femoral MAP while the carotid MAP increased. Wilcoxon signed-rank test showed statistically significant difference in the blood flow index values from baseline for the 38 trials ($P < 0.0001$). Aortic occlusion yielded similar results when the probe was placed *via* laminectomy (N = 6) or percutaneous (N = 4) approaches.

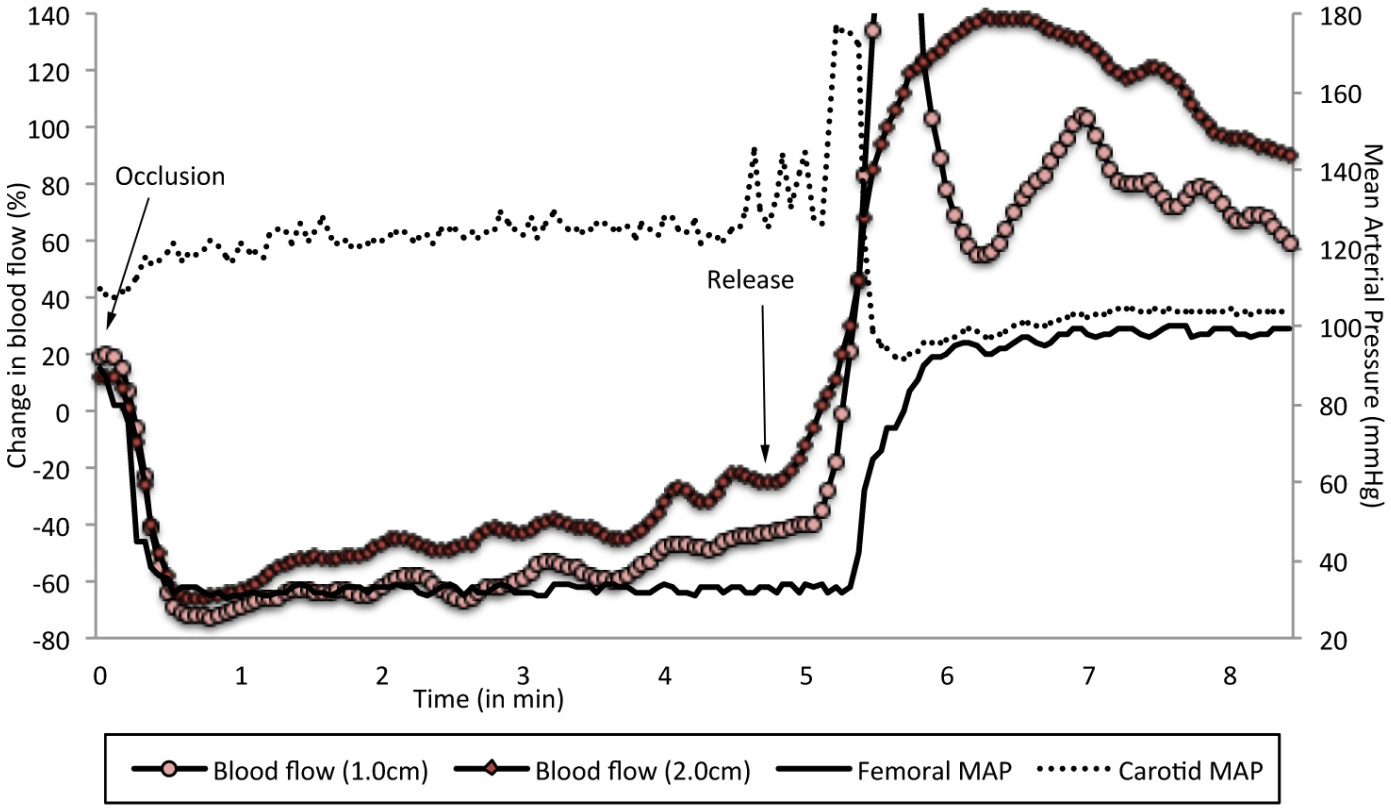

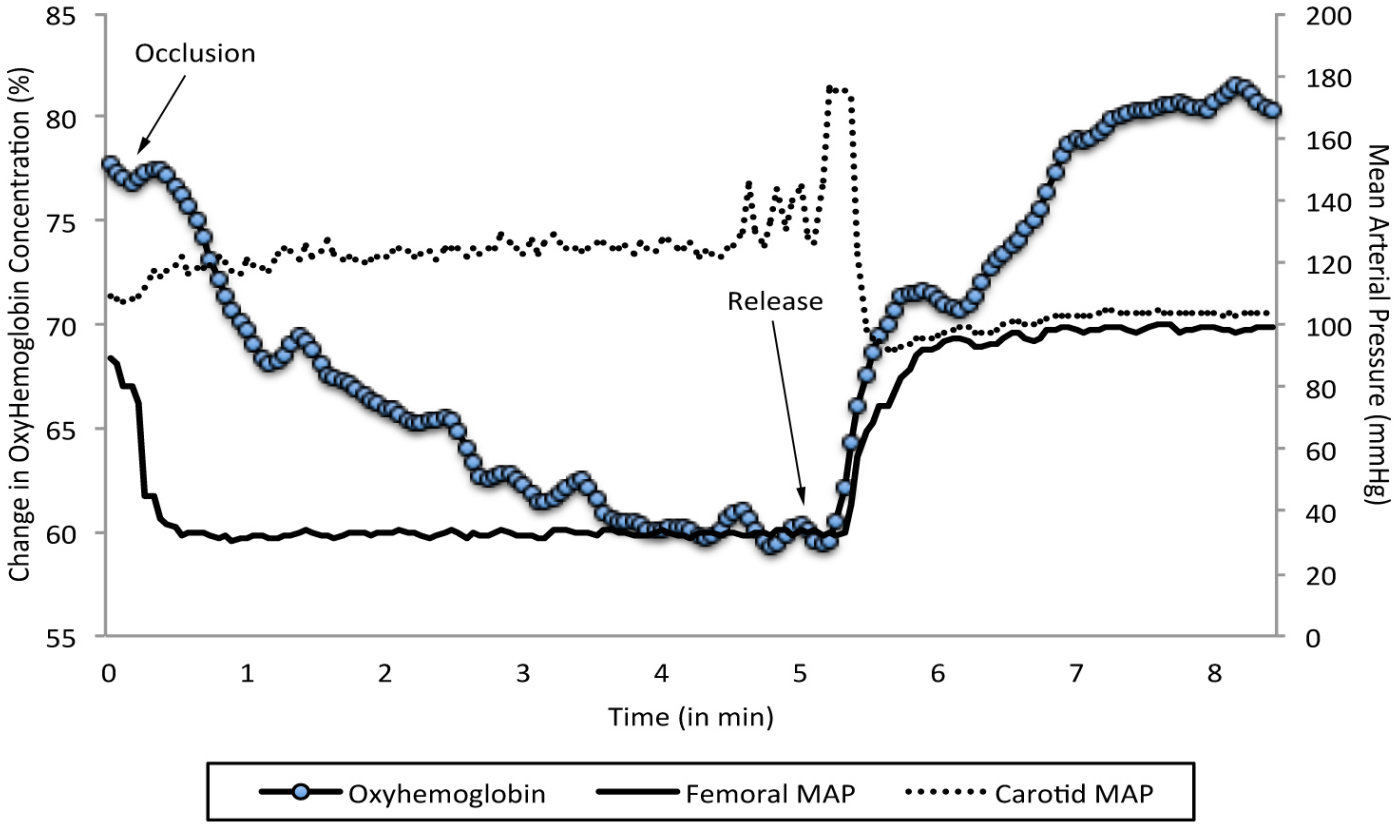

Figure 5.4: A representative example showing the decrease in spinal cord blood flow (top) and oxygenation (bottom) detected by DCS and DOS respectively upon proximal aortic occlusion. In this example, the peak blood flow decrease was ~ 83% and peak oxygenation decrease was ~ 18%. Decrease in spinal cord blood flow and oxygenation closely paralleled the decrease in femoral mean arterial pressure and increase in carotid mean arterial pressure. Top: The X-axis represents the time taken in minutes to detect a change in spinal cord blood flow or mean arterial pressure; the primary Y-axis represents the change in blood flow in percent detected by DCS; the secondary Y-axis represents the change in femoral and carotid mean arterial pressures in mmHg detected by the Powerlab device. Bottom: The X-axis represents the time taken in minutes to detect a change in spinal cord oxyhemoglobin concentration or mean arterial pressure; the primary Y-axis represents the change in oxyhemoglobin concentration in percent detected by DOS; the secondary Y-axis represents the change in femoral and carotid mean arterial pressures in mmHg detected by the Powerlab device.

5.3.3. Discussion

The fiber-optic probe and monitoring device reliably detected spinal cord responses to occlusion of the proximal descending thoracic aorta in fourteen sheep. Clamping the aorta resulted in a rapid decrement in spinal cord blood flow and a slower decrement in tissue oxygenation, as expected. Unclamping the aorta resulted in a hyperemic overshoot from baseline. Since the femoral artery is at a level below the occlusion site, the femoral MAP was expected to decrease. The carotid MAP increased since the carotid artery is located above the site of occlusion. The responses to all interventions were robust, immediate, and reproducible. In all cases, changes in flow were more immediately responsive than changes in oxygenation.

5.4. Distance from Aortic Occlusion Site and Spinal Cord Hemodynamics

The blood supply to the anterior circulation of the spinal cord in humans, down to the lower thoracic/ high lumbar vertebral level, is highly dependent on vertebral artery sources of blood flow originating superiorly from the cephalic trunk. The anatomy of the sheep in this regard is not well documented. When the descending thoracic aorta is occluded proximally, this should eliminate blood supply from local contributions, such as thoracolumbar arteries and the artery of Adamkiewicz, making the spinal cord dependent on collateral blood flow from vertebral sources originating above the occlusion site. Thus, we would expect a progressively greater decrease in spinal cord

blood flow and oxygenation as we move down the spinal cord, farther away from the occlusion site and origin of the vertebral arteries. The figure 5.5 below shows the human spinal cord and the vasculature supplying its blood flow.

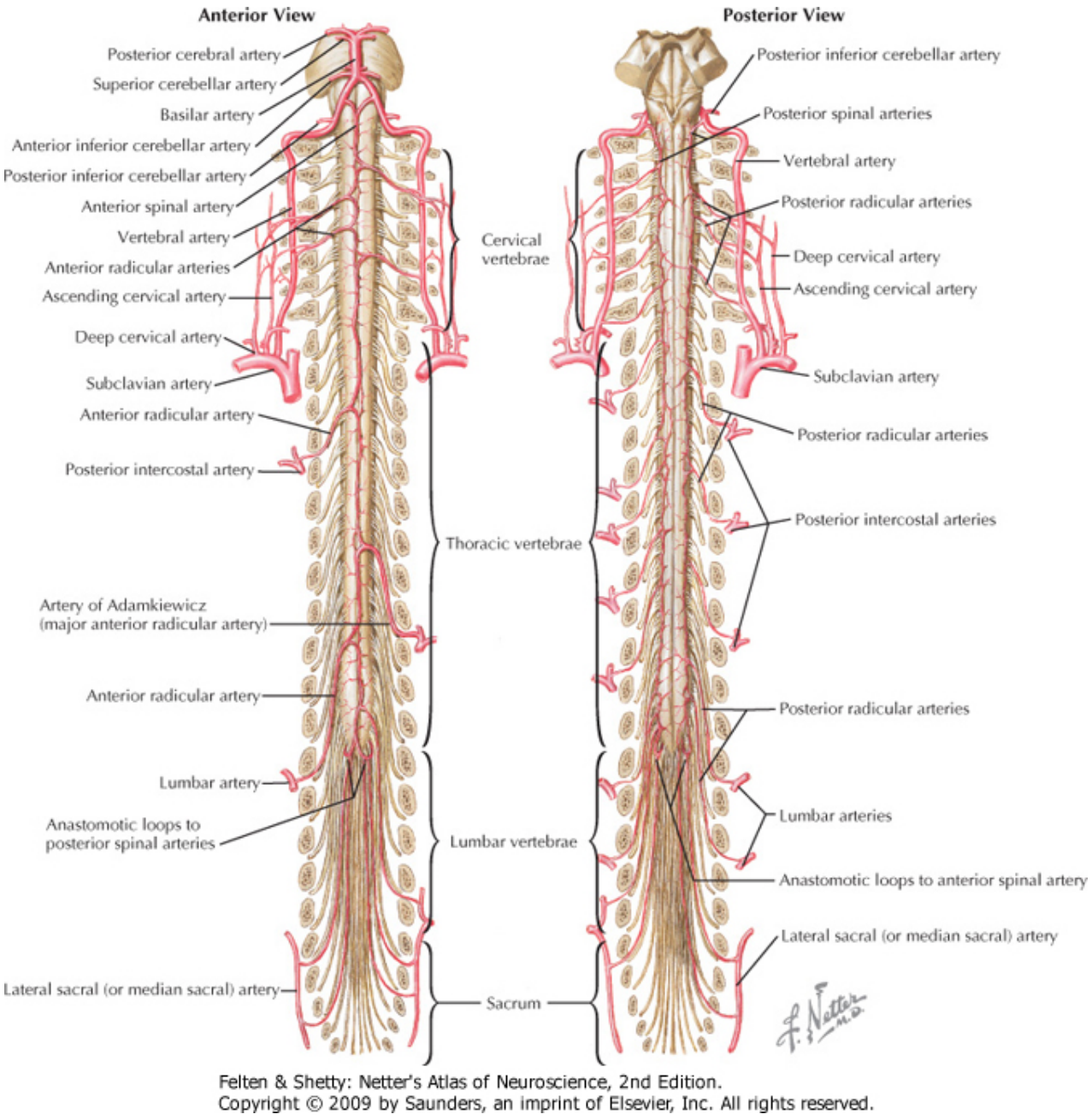

Figure 5.5: The human spinal cord and its vascular supply. (Illustration adapted from Felten and Shetty: Netter's Atlas of Neuroscience, 2nd Edition).

Here we tested, in a single sheep, the hypothesis that spinal cord blood flow and oxygenation diminishes with increasing distance from the site of proximal aortic occlusion and from the sites of collateral blood flow originating from sources above the level of the occlusion, and that the probe is capable of detecting the effect of distance upon flow and oxygenation. We thus attempted to demonstrate that the device could axially resolve differences in changes in blood flow and oxygenation during ischemia due to differences in vascular anatomy.

5.4.1. Methods

Aortic occlusion was again achieved via inflation of an intra-aortic balloon just below the common cephalic trunk and was maintained for 5 minutes. During sequential aortic occlusions, spinal cord blood flow and oxygenation were recorded with the probe placed at the vertebral levels T4, T7, T11, and L2. Prior to probe repositioning and repeated measurements, aortic occlusion was released and MAP allowed to recover to baseline. Corresponding microsphere measurements of spinal cord blood flow at baseline and following aortic occlusion at each level were conducted as described below in section 6.1.

5.4.2. Results

The descending thoracic aortic occlusion just below the level of the common cephalic trunk was associated with greater diminution in spinal cord blood flow with increasing distance from the occlusion site. Spinal cord blood flow decreased by ~62% (T4 level), ~65% (T7 level), ~89% (T11 level) and ~90% (L2 level), while oxygenation decreased by ~18% (T4 level), ~23% (T7 level), ~40% (T11 level) and ~40% (L2 level), as shown in figure 5.6. Blood flow measured by DCS correlated with blood flow measured by microspheres (R^2=0.92) as shown in figure 5.7.

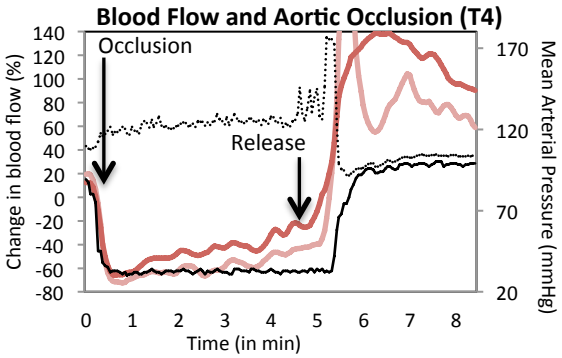
Blood Flow and Aortic Occlusion (T4)
Occlusion
Release
Change in blood flow (%)
Mean Arterial Pressure (mmHg)
Time (in min)

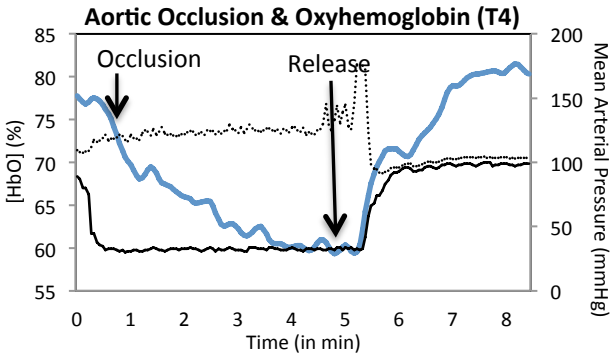
Aortic Occlusion & Oxyhemoglobin (T4)
Occlusion
Release
[HbO] (%)
Mean Arterial Pressure (mmHg)
Time (in min)

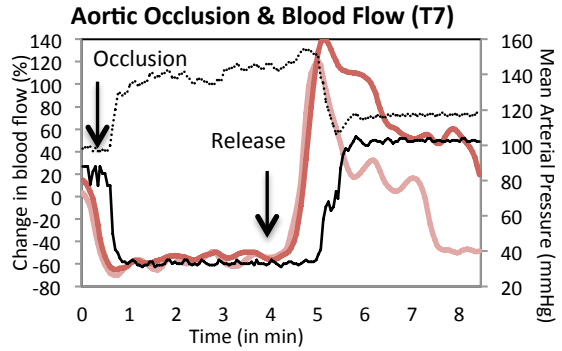
Aortic Occlusion & Blood Flow (T7)
Occlusion
Release
Change in blood flow (%)
Mean Arterial Pressure (mmHg)
Time (in min)

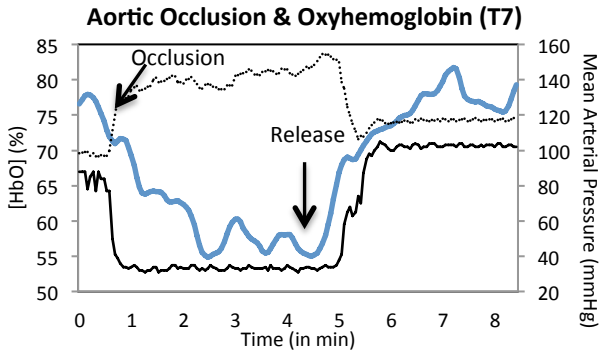
Aortic Occlusion & Oxyhemoglobin (T7)
Occlusion
Release
[HbO] (%)
Mean Arterial Pressure (mmHg)
Time (in min)

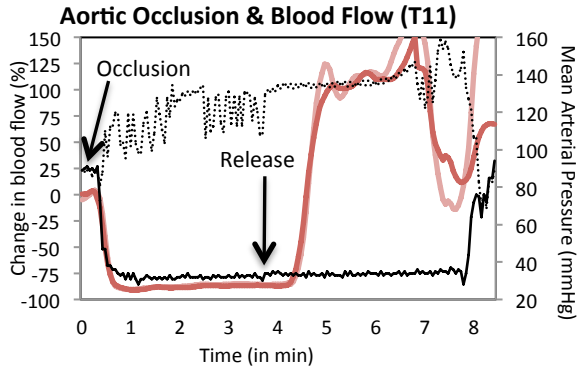
Aortic Occlusion & Blood Flow (T11)
Occlusion
Release
Change in blood flow (%)
Mean Arterial Pressure (mmHg)
Time (in min)

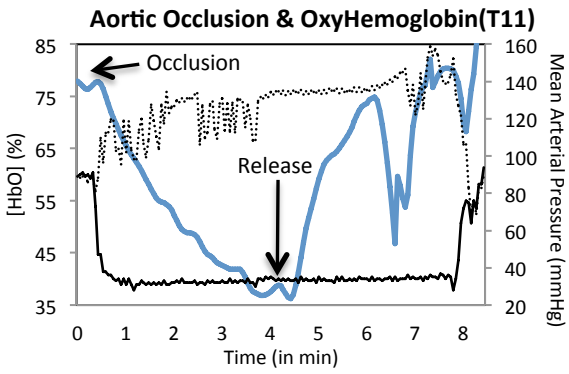
Aortic Occlusion & OxyHemoglobin(T11)
Occlusion
Release
[HbO] (%)
Mean Arterial Pressure (mmHg)
Time (in min)

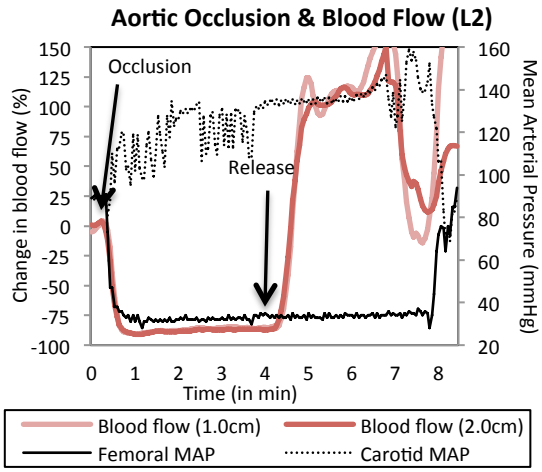
Aortic Occlusion & Blood Flow (L2)
Occlusion
Release
Change in blood flow (%)
Mean Arterial Pressure (mmHg)
Time (in min)
Blood flow (1.0cm)
Blood flow (2.0cm)
Femoral MAP
Carotid MAP

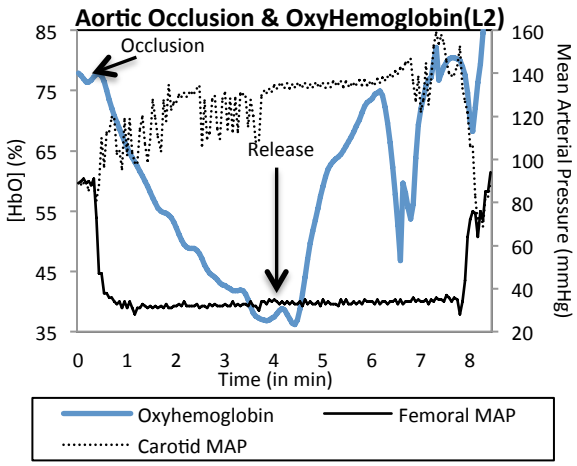
Aortic Occlusion & OxyHemoglobin(L2)
Occlusion
Release
[HbO] (%)
Mean Arterial Pressure (mmHg)
Time (in min)
Oxyhemoglobin
Femoral MAP
Carotid MAP

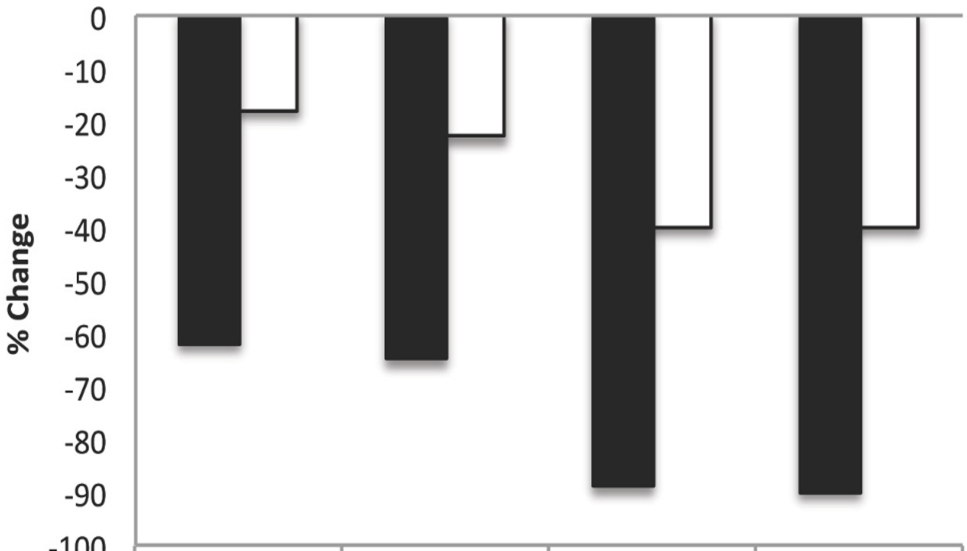

	T4 Level	T7 Level	T11 Level	L2-L3 Level
■ Blood Flow	-62	-65	-89	-90
□ Oxygenation	-18	-23	-40	-40

Figure 5.6: This figure depicts the percent change in blood flow (black bars) and oxygenation (white bars) detected at the T4, T7, T11 and L2-L3 vertebral levels respectively upon aortic occlusion. Clamping the proximal descending thoracic aorta cuts off blood supply from intercostal arteries, making the spinal cord flow heavily dependent on flow from vertebral arteries above the occlusion site. One would then expect a greater decrease in blood flow and oxygenation the farther one moves away from the occlusion site and vertebral artery sources. Flow and oxygenation measurements made sequentially from T4 to L3 during proximal aortic occlusion documented this pattern.

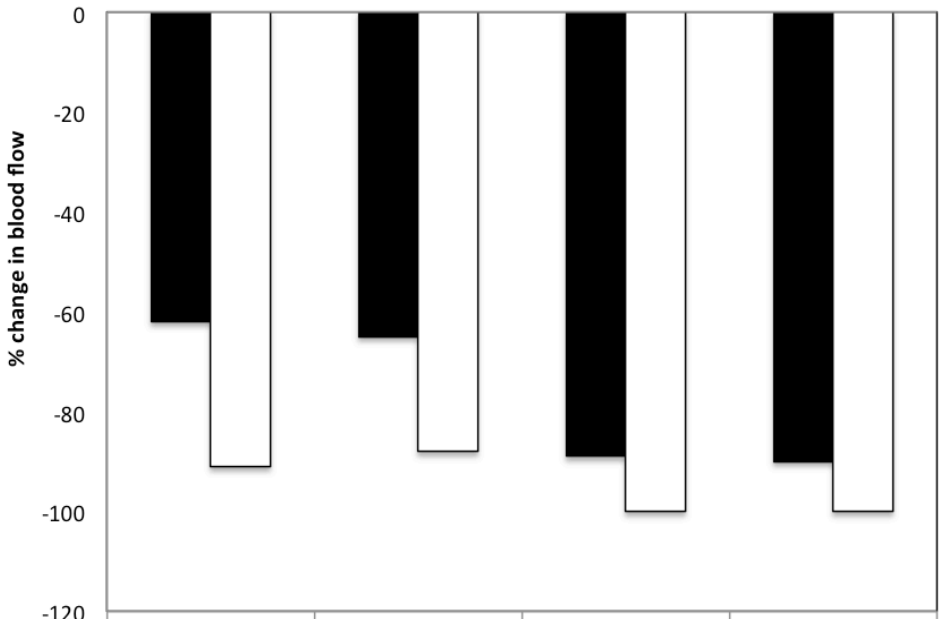

	T4 Level	T7 Level	T11 Level	L2-L3 Level
■ DCS: Blood Flow	-62	-65	-89	-90
□ Microspheres: Blood Flow	-91	-88	-100	-100

Figure 5.7: This figure depicts the percent change in blood flow detected by DCS (black bars) and microspheres (white bars) at the T4, T7, T11 and L2-L3 vertebral levels respectively. Blood flow changes detected by both techniques correlated well (R^2=0.92).

5.4.3. Discussion

In humans, it is well documented that the proximal to mid thoracic anterior spinal cord receives a significant contribution from the vertebral arteries (*162*). More distal aspects of the thoracic and lumbar spinal cord are dependent upon blood supply directly from the descending thoracic and abdominal aorta. Multiple reports establish the unpredictable and diffuse nature of the blood supply to the spinal cord (*163, 164*). This unpredictable blood supply demands a monitoring technique that is not discretely focused upon a single level. The experiment we performed above shows that the DCS/DOS monitor and fiber-optic probe can axially resolve changes in spinal cord blood flow and oxygenation differences at variable vertebral levels.

Chapter 6

Validation of the DCS Technique

The previous two chapters have focused on the testing the ability of the optical monitor and fiber-optic probe to successfully detect induced changes in spinal cord blood flow and oxygenation. This chapter focuses on the validation of the DCS technique with microspheres, which are the current "gold standard" technique used for measuring regional blood flow in research. Since DOS has been extensively used in various applications and the validity of its measurements extensively studied, we focused on testing the validity of the DCS measurements of blood flow changes in the sheep spinal cord. DCS is a relatively novel technique, and furthermore, it has never been used on spinal cord tissue or in sheep model, making the testing of the validity of the DCS measurements essential.

Next, we addressed the question of whether the fiber-optic probe is truly measuring spinal cord blood flow changes. First we examined if the surrounding paraspinous muscles interfere with the blood flow measurements by DCS. Since the paraspinous muscle blood flow is too low to be measured, we did not anticipate our fiber-optic probe to pick up any changes in systemic blood flow that were induced. We also sought to prove that the fiber-optic probe was indeed measuring blood flow changes in the spinal cord and not in surrounding tissues or muscles by performing

interventions that would only elicit regional changes in the spinal cord. These interventions included: inflating an epidural balloon directly on to the spinal cord and performing spinal distraction surgery. Both the approaches would only cause a decrease in spinal cord blood flow since they directly affect spinal cord vascular circulation while leaving surrounding muscles and tissues unaffected.

6.1. Comparison of DCS with Microspheres

Microspheres can measure absolute blood flow, and are often considered a "gold standard" in measuring regional blood flow in a particular organ. Thus, we wanted to compare changes in blood flow detected by DCS and microspheres.

The accuracy of any microsphere blood flow measurement technique is dependent on having a sufficient number of microspheres present within the tissue sample, the spinal cord tissue in our case. A minimum of 400 microspheres are needed per tissue sample for a 95% probability that the blood flow measurement will be within 10% of the true value (*165*).

6.1.1. Methods

The accuracy of the device was tested via comparison of DCS with microsphere spinal cord blood flow measurements. Nonradioactive stable-isotope labeled microspheres of 15 μm diameter were injected into the left atrium (10 ml, $2x10^6$ microspheres/ml, STERIspheres, BioPal Inc., MA). Reference blood samples were

withdrawn from the distal aorta via the femoral artery catheter at a rate of 600 ml/hr over 3 min using a syringe pump (Harvard Apparatus, MA). Multiple measurements (n=20) during interventions (nitroprusside- 400 µg bolus, phenylephrine- 400 µg bolus, aortic clamping) were performed through the use of multi-color microspheres in seven sheep.

At the end of the experiments, the sheep were euthanized. Spinal cord tissue blocks and blood samples were then prepared for subsequent analysis of microsphere concentrations and blood flow. Following euthanasia, the spinal cord was resected, labeled, weighed and placed in tracer-free polypropylene sample vials provided by BioPAL Inc. SansSaLine was used to aid in the transfer of blood samples to a BioPAL to the blood sample vials. SansSaLine is a saline-free buffer, which is used as a substitute for saline or Phosphate Buffered Saline (PBS) in histochemical stains, to wash and clean the blood and tissue samples in order to minimize sodium background activity, thereby maximizing the sensitivity of the measurement.

The blood samples in the blood sample vials were centrifuged for 1 minute at 2,000 RPM. The supernatant was aspirated to a level safely above the visible pellet. The pellet was resuspended in SansSaLine and the centrifugation and aspiration steps were repeated. Both spinal cord tissue and blood samples were then dried overnight via a warming oven at 70C. This step would prevent the potential leakage of the samples during shipment to BioPAL Inc. for analysis. Once dried, the tissue blocks and blood samples were sent to the company for analysis, where the assay of the microspheres was performed.

A neutron activation assay technique (*166*) was used to measure the microsphere content and blood flow was calculated in mL/min/g. Neutron activation is an analytical technique wherein the tissue samples are exposed to neutrons that penetrate the isotopic elements within the sample, rendering them radioactive. The radioactive elements are then quantified using high-resolution radiation counting equipment. Once the tissue and blood samples were received at BioPAL, they were exposed to a field of neutrons and the vials were then stored for 48 hours to allow short-lived activation products to decay. After this decay period, spectroscopic analysis was performed on each sample, with corrections made to account for interradionuclide crossover and tracer decay during the counting period. In addition, instruments were calibrated to account for differences in sample volume and geometry. The results of the assay were reported as the number of disintegrations per minute measured for each stable labeled microsphere set.

Absolute tissue blood flow (mL/min/g), measured by the stable isotope-labeled microspheres, was calculated for the radiolabeled microspheres as previously described (*165*). Briefly, the microsphere concentration (measured in disintegrations per minute, dpm/g) in the blood samples taken during each intervention was normalized to the microsphere concentration measured in a 2 min reference blood sample (taken during the baseline microsphere measurement).

Once we received the values of absolute blood flow measurements obtained by the microspheres in each blood sample after each intervention, we compared the percent change in blood flow from baseline detected by microspheres, with the peak/nadir value of the percent change in Blood Flow Index (BFI) measured with DCS from baseline.

Spinal cord blood flow measured by the DCS and microsphere techniques was compared by correlating the simultaneous point measurements across all animals and trials. The degree of correlation was measured by the Pearson correlation coefficient. The ratios of DCS changes to microsphere changes from baseline were obtained from the slope of the curve. All statistical analysis was performed using JMP Statistical Software (SAS Institute, NC).

6.1.2. Results

DCS and microspheres were used to measure blood flow changes immediately after performing the following interventions: 400 μg phenylephrine bolus (n=6), 400 μg nitroprusside bolus (n=4) and aortic occlusion (n=10) in seven sheep. Due to the cost associated with our experiments, multiple interventions were performed in each sheep. Table 6.1 below represents which interventions were performed in each sheep and a summary of the percent change in blood flow detected by microspheres and DCS for each intervention.

Sheep #	Intervention	% change in blood flow - microspheres	% change in blood flow - DCS
1	Phenylephrine Bolus	19	69
1	Aortic Occlusion	-85	-85
2	Aortic Occlusion	-99	-73
3	Aortic Occlusion	-91	-100
4	Aortic Occlusion	-91	-62
4	Aortic Occlusion	-88	-65
4	Aortic Occlusion	-100	-89
4	Aortic Occlusion	-100	-90
5	Epidural Balloon	-28	-32
6	Phenylephrine Bolus	115	41
6	Phenylephrine Bolus	-90	39
6	Phenylephrine Bolus	40	23
6	Nitroprusside Bolus	30	-38
6	Nitroprusside Bolus	30	-32
7	Phenylephrine Bolus	17	41
7	Phenylephrine Bolus	33	20
7	Nitroprusside Bolus	-11	-25
7	Nitroprusside Bolus	-17	-25
7	Epidural Balloon	-35	-100
7	Epidural Balloon	-100	-75

Table 6.1: Multiple interventions (n = 20) were performed in seven sheep to elicit changes in spinal cord blood flow, which were then measured by DCS and microspheres simultaneously. The table summarizes which interventions were performed in each sheep and the percent change in blood flow detected by each technique.

The bar graph below (figure 6.1) depicts the percent changes in spinal cord blood flow measured by the DCS and microsphere techniques. The peak/nadir blood flow value measured by DCS and the absolute blood flow value measured by a microsphere injected at the start of a certain intervention were compared. Different isotope-labeled microspheres were used for each different intervention to distinguish between them.

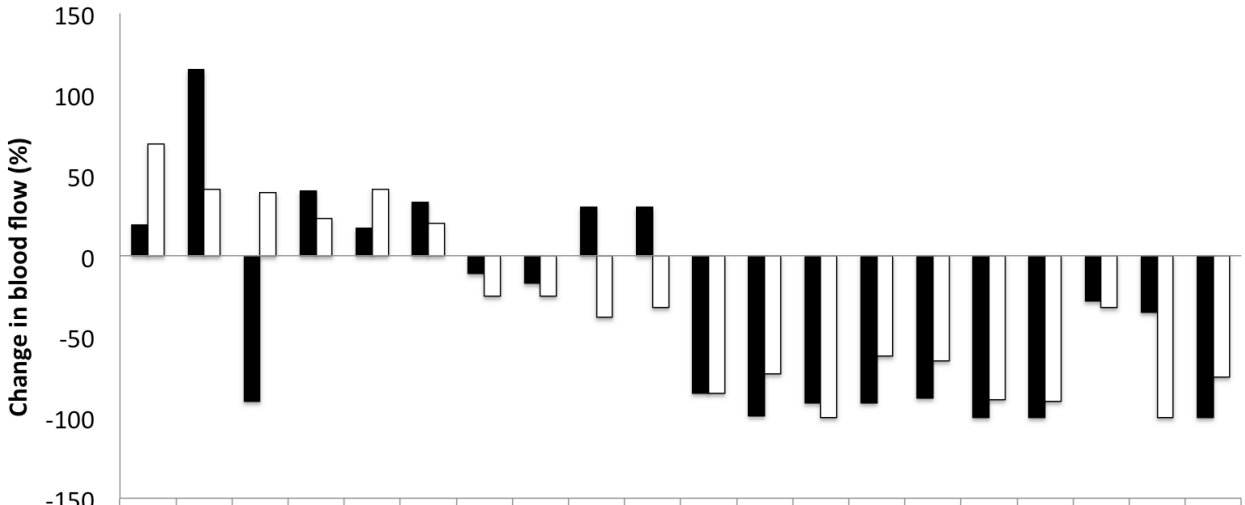

	A	A	A	A	A	A	B	B	B	B	C	C	C	C	C	C	C	C	C	C
■ Microspheres	19	115	-90	40	17	33	-11	-17	30	30	-85	-99	-91	-91	-88	-100	-100	-28	-35	-100
□ DCS	69	41	39	23	41	20	-25	-25	-38	-32	-85	-73	-100	-62	-65	-89	-90	-32	-100	-75

Figure 6.1: Bar Graph summarizing the percent changes in spinal cord blood flow detected by the microsphere (black bars) and DCS techniques (white bars) upon performing various interventions: A- 400 µg phenylephrine bolus, B- 400 µg nitroprusside bolus and C- aortic occlusion.

Peak or nadir changes in blood flow during continuous monitoring of DCS correlated reasonably well with the change measured with microspheres after a single injection during the intervention (R^2=0.49, $p < 0.01$, Figure 6.2).

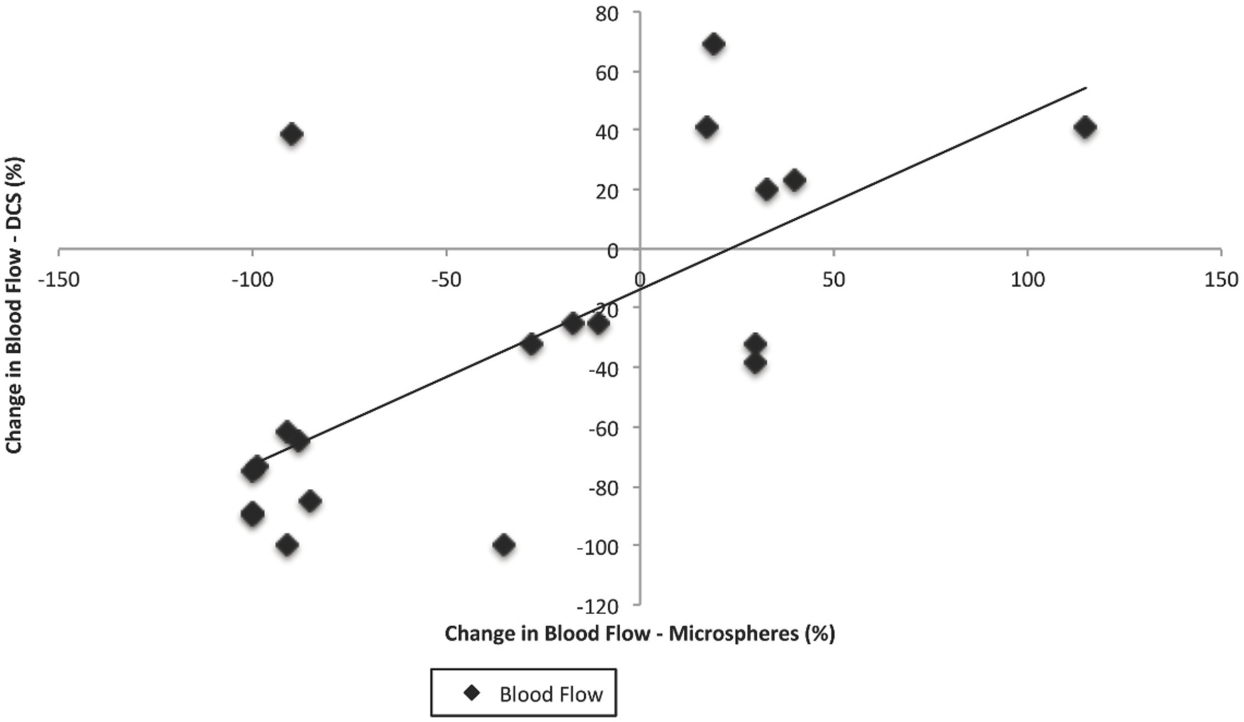

Figure 6.2: Scatter plot representing the Pearson Correlation between microsphere and DCS measurements of blood flow changes (R^2=0.49, $p<0.01$, n=22). The X-axis represents the percent change in blood flow detected by microspheres while the Y-axis represents the percent change in blood flow detected by DCS.

6.1.3. Discussion

The accuracy of the blood flow changes measured by the optical probe was difficult to determine due to the fact that no true 'gold standard' exists for the measurement of spinal cord blood flow. The microsphere measurements and DCS measurements of spinal cord blood flow have some differences that make a direct comparison between the two methods difficult. DCS has high temporal resolution

(milliseconds) and offers continuous measurements, but the units of the DCS blood flow index are not the same as absolute flow units. Microsphere measurements, on the other hand, require minutes to complete, but offer quantitative measurements of flow (in absolute units). Thus, it is not possible to exactly match the DCS peak or nadir measurement with the microsphere measurement as observed in our data.

Microsphere measurements in the spinal cord can be challenging for other reasons. The entire spinal cord, in a 50 kg sheep, weighs between 20-25 grams. Spinal cord blood flow is reported to be in the range of 20-40 ml/100g/min. In a 50 kg sheep, with a 4 l/min cardiac output, the cord receives approximately 10 ml/minute, or 0.25% of the total cardiac output. The fraction of microspheres injected reaching the cord is then 0.25%, and the sampled volume of spinal cord analyzed is approximately 2-5 grams. Therefore, microsphere measurements are themselves clearly challenged by a number of factors severely limiting their own accuracy. Thus, while there was a reasonably good correlation between the DCS and microsphere measurements, the differences in the techniques may explain the lack of an excellent correlation curve.

An alternative method for comparison might be Laser Doppler Flowmetry (LDF). LDF has high temporal resolution, but its depth of penetration is limited to < 0.5 mm. An LDF probe, placed upon the posterior cord, could tell us almost nothing about flow in the anterior spinal cord, which is the area of greatest interest since the anterior circulation affects motor function. The DCS/DOS device offers not only high temporal resolution

(~3-8 seconds), but can also interrogate the entire depth of the spinal cord, providing valuable information about anterior and posterior blood flow. Furthermore, the LDF probe is rigid and placement can be difficult. The fiber-optic probe we have designed is flexible and can be placed relatively easily in an approach similar to the placement of spinal drains and epidural catheters.

6.2. Are we truly measuring blood flow in the spinal cord?

Since we are the first group to use DCS to measure the blood flow in the spinal cord, we performed a series of experiments to prove that what we are measuring is indeed blood flow changes in the spinal cord tissue and that our recordings were not influenced by blood flow changes in surrounding areas such as the paraspinous muscles. We performed interventions/surgeries that would only cause a localized decrease in spinal cord blood flow, without affecting the overall systemic hemodynamics in the sheep. We also placed the fiber-optic probe directly into the paraspinous muscle (as opposed to placement onto the spinal cord tissue) and hypothesized that there should be no changes in blood flow detected by DCS upon administering vasopressors/ vasodilators or aortic occlusion. The sections below detail these experiments performed to validate that the fiber-optic probe is truly measuring blood flow changes in the spinal cord.

6.2.1. Epidural Balloon Inflation

To create a localized injury to the spinal cord tissue without causing a systemic change, we inflated a Fogarty Arterial Embolectomy balloon catheter (Edwards Lifesciences, CA) directly onto the spinal cord tissue. Figure 6.3 below shows an image of the Fogarty Arterial Embolectomy balloon catheter (left). Since there was no record of similar experiments found in literature search, the ideal size of the balloon catheter was determined by trial and error in a single sheep. We chose three different balloon catheter sizes of 5 French (F), 6F and 7F, which would have an inflated balloon diameter of 11 mm, 13 mm and 14 mm respectively. Each balloon was placed into the epidural space and inflated onto the spinal cord and the DCS measurements were recorded. Only the inflated 7F balloon exerted enough pressure to crush the spinal cord tissue and create an injury resulting in drop of spinal cord blood flow and oxygenation. This was confirmed at the end of the experiment when the sheep was euthanized and spinal cord tissue was resected. Only the 7F balloon caused visible injury to the spinal cord (figure 6.3, right). Thus, we decided that using 7F Fogarty arterial embolectomy balloons for our experiments would be the ideal choice.

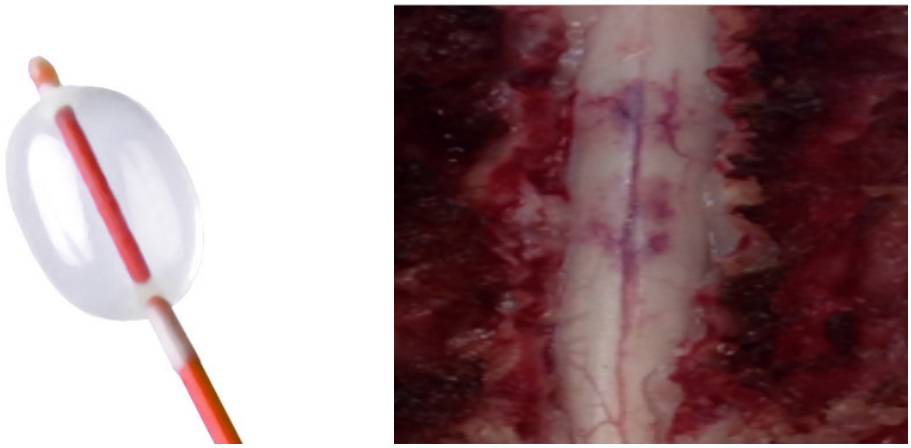

Figure 6.3: Left: Inflated Fogarty Arterial Embolectomy Balloon. Right: Spinal cord tissue with visible injury due to inflation of a 7 French Fogarty Arterial Embolectomy balloon catheter in the epidural space of the spinal cord of a sheep.

6.2.1.1. Methods

In this set of experiments, we introduced the 7F balloon into the epidural space of the spinal cord (either directly through a laminectomy, or percutaneously and advanced it under fluoroscopic guidance) to lie adjacent to the fiber-optic probe detectors in three sheep. The balloon was then inflated to compress the cord directly adjacent to the probe while spinal cord blood flow was recorded by DCS. The figure 6.4 shows the placement of the epidural balloon and fiber-optic probe directly onto the spinal cord tissue either percutaneously into the epidural space and confirmed fluoroscopically (radiographic image) or directly into the epidural space following a laminectomy (inset image).

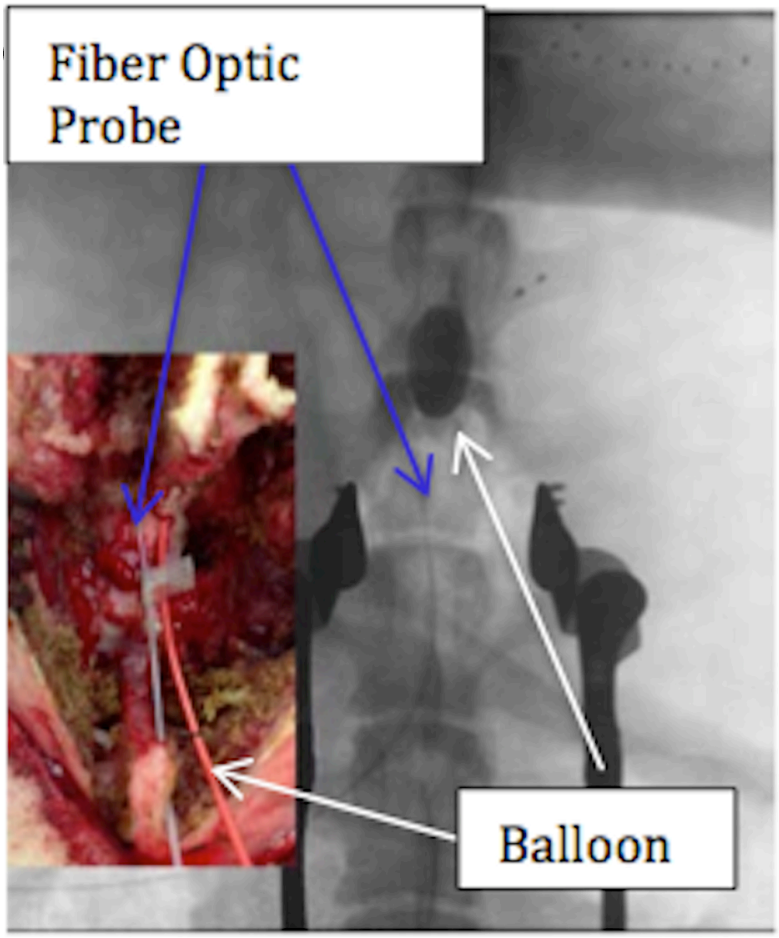

Figure 6.4: The radiographic image shows the epidural balloon placed directly on top of the spinal cord tissue, and adjacent to the fiber-optic probe. In this case, the balloon has been inflated, thus crushing the spinal cord. The inset image shows a picture taken during the experiment wherein the fiber-optic probe and epidural balloon were placed under direct vision following a laminectomy, to lie adjacent to each other on top of the spinal cord tissue.

6.2.1.2. Results

Upon epidural balloon inflation, there was an immediate drop in spinal cord blood flow (-75 ± 14%, n=3) and oxygenation (- 10 ± 6%, n=3), which recovered as soon as the balloon was released. An example is shown in figure 6.5.

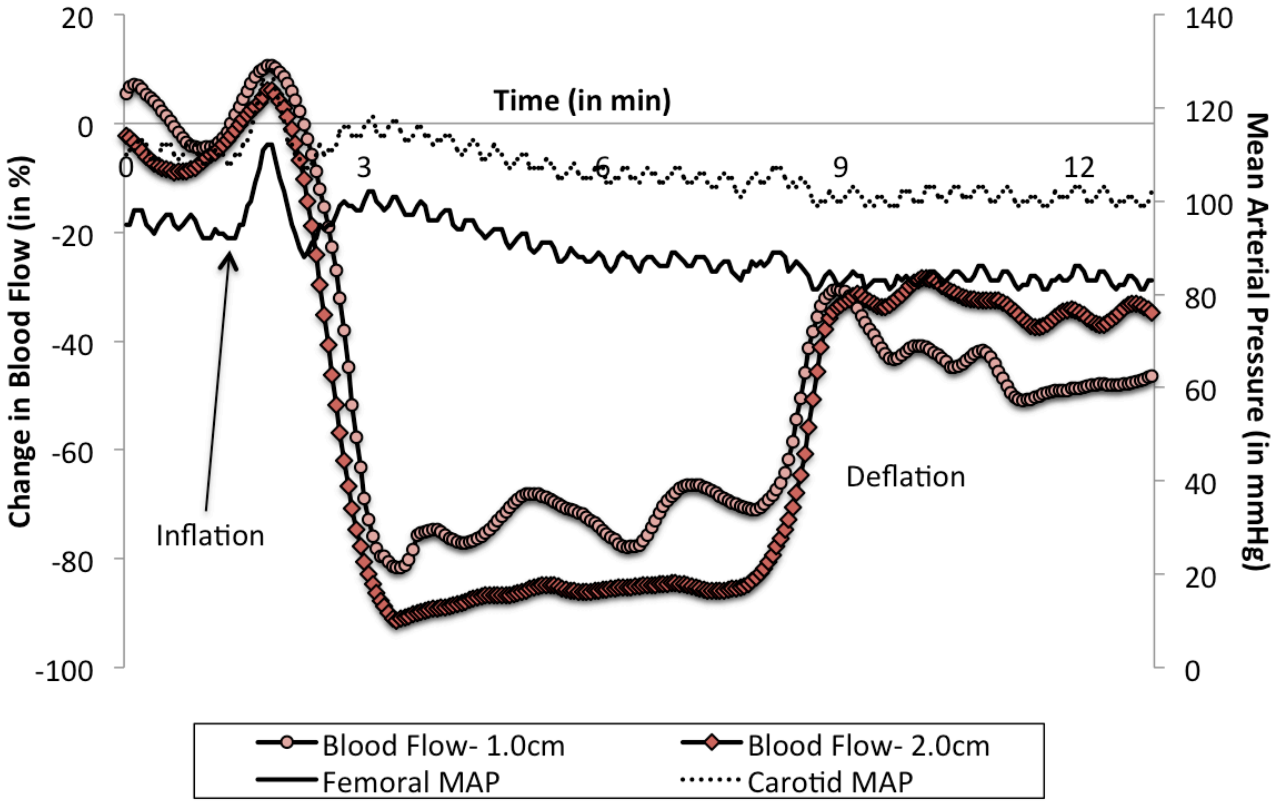

Figure 6.5: A representative example showing the decrease in spinal cord blood flow detected by DCS upon inflation of a 6 French Fogarty arterial embolectomy balloon catheter directly onto the spinal cord tissue, which created localized spinal cord injury. The fiber-optic probe, placed at the site of injury, immediately detected a drop in blood flow upon balloon inflation, which recovered soon after the balloon was deflated. The X-axis represents time in minutes and the Y-axis represents the percentage of change in the blood flow detected by DCS. Since this was a localized intervention and not a systemic intervention (such as aortic clamping), there was no noticeable effect on the femoral and carotid mean arterial pressures.

6.2.1.3. Discussion

While thoracic aortic clamping can be expected to result in diminished flow to not only the spinal cord, but also the aorta and paraspinous muscles, epidural balloon inflation onto the spinal cord creates a localized decrease in blood flow only in the spinal cord, leaving flow in surrounding muscles and vessels intact. As inflation of the epidural balloon over the probe resulted in a near complete and instantaneous loss of blood flow, we can therefore conclude that the probe was not measuring flow in the aorta, paraspinous muscles, or other source.

6.2.2. Spine Distraction

Spinal cord injury, resulting in paralysis, can follow spine trauma and spine surgery. Distraction, as a mechanism of injury, occurs in both trauma and from corrective maneuvers to improve spinal deformity. Spinal cord ischemia (lack of blood flow) has been proposed as the underlying cause (*58, 167*). Evidence suggests that ischemia occurs before mechanical injury to the spinal cord. Continuously monitoring for spinal cord ischemia during surgery could alert the surgeon to the earliest stages of pre-injury, thereby making surgery safer. Currently available approaches to monitor spinal cord function, namely evoked potential monitoring, are associated with a significant delay between the onset of spinal cord ischemia and the occurrence of functional changes (*69, 168, 169*). This delay handicaps surgeons by offering data that is neither timely nor specific.

6.2.2.1. Methods

A distraction model was created in a single sheep under sterile conditions. Anesthesia was administered as described in section 4.2.1. The levels T9 and T10 were identified under fluoroscopic guidance. A longitudinal midline incision and subperiosteal dissection were performed to the tips of the transverse processes. Pedicles were identified using anatomic landmarks and confirmed using fluoroscopy. A burr was used to make a pilot hole and a pedicle awl was used to create a tract down the pedicle into the vertebral body. A ball tipped probe was used to palpate the tract to confirm acceptable position. The tract was tapped and an appropriate sized stainless steel pedicle screw placed. Screws were placed bilaterally at the T9 and T10 levels, and a stainless steel rod was placed into the head of the pedicle screws. In order to allow the spinal column to distract, a complete facetectomy, release of the interspinous ligaments, and anterior vertebral column osteotomy were performed. Distraction was performed in intervals of 1 mm by placing a ratcheting distractor between the pedicle screws on the rod bilaterally.

The fiber-optic probe was placed at the site of distraction under fluoroscopic guidance and spinal cord blood flow and oxygenation were continuously monitored. Motor evoked potentials (MEPs) were also monitored throughout the distraction procedure (see chapter 9 for details on evoked potential monitoring techniques). Fluoroscopy and calipers were used to confirm the length of the distraction bilaterally. 2 mm of distraction was performed every two minutes. Distraction was ceased at the time when a 50% fall in blood flow was measured with the probe or at the time when a

significant change (80% fall from baseline) in MEPs occurred. Once either of these criteria were reached, distraction was stopped and monitoring continued for 7 minutes. DCS blood flow and MEPs were continuously recorded. After 7 minutes, the spine was relaxed to its pre-distraction state, the hardware tightened, the wound closed and the animal recovered for neurological evaluation over 24 hours.

The recovered sheep was monitored for respiratory rate, heart rate, signs of distress or agitation, temperature and neurological compromise as measured by the modified Tarlov scoring system (see section 8.2. for details). The sheep was monitored hourly for the first four hours after surgery. After 24 hours post-surgery, the sheep was euthanized and the spinal cord was resected from the T9- L1 position for histological evaluation of ischemic and/or mechanical injury.

6.2.2.2. Results

In a single sheep, distraction was performed every two minutes until maximal resistance was felt, at 24 mm, distraction. The distraction was held at 24 mm for seven minutes. The fiber-optic probe measured a decrease in spinal cord blood flow by 50% approximately 30 seconds post-distraction, with a maximum decrease in blood flow of approximately 80%. Evoked potential signal amplitude took approximately five minutes post-distraction to decrease by 50%, indicating that DCS is much more sensitive to spinal cord hemodynamic changes and has greater temporal resolution than evoked

potentials. Upon release of distraction by removing the rods and screws, partial recovery of spinal cord blood flow was measured by DCS. The figure 6.6 below summarizes the results of this experiment.

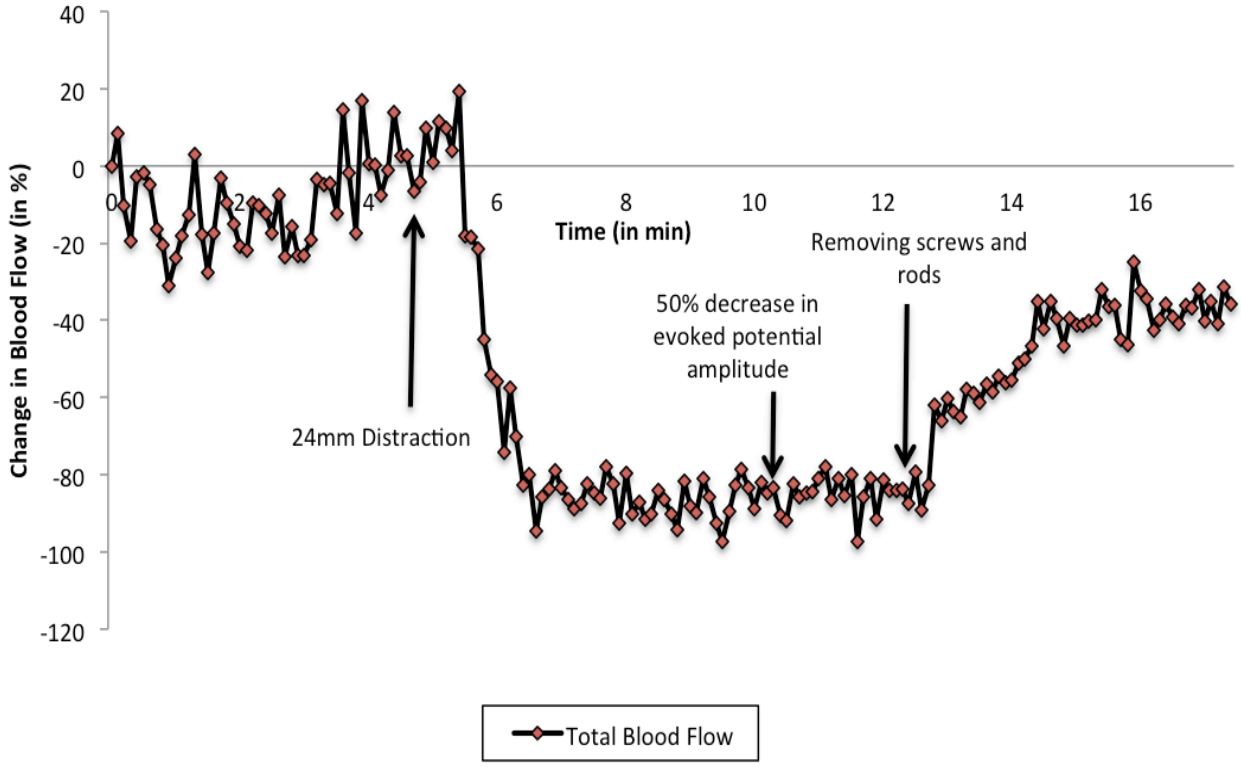

Figure 6.6: A Spine Distraction Model was created in a single sheep and the distraction was held at 24 mm for 7 minutes. There was an approximately 80% decrease in spinal cord blood flow detected by DCS 1 minute after distraction, while evoked potential signal amplitude decreased by 50% approximately 5 minutes after distraction. Partial recovery in spinal cord blood flow was observed after relieving the distraction by removing the rods and screws placed on the spinal cord. The X-axis represents time in minutes and the Y-axis represents the percentage of change in the blood flow detected by DCS.

6.2.2.3. Discussion

The spinal cord distraction model created localized spinal cord injury and since the fiber-optic probe detected a decrease in spinal cord blood flow, it offers further evidence that the probe is truly measuring changes in blood flow in the spinal cord and not in surrounding vessels or muscles. Furthermore, this experiment serves to prove that DCS is more sensitive to hemodynamic changes in the spinal cord and has a higher temporal resolution than the current gold standard technique used to monitor spinal cord integrity, namely evoked potential monitoring.

6.2.3. Probe Placement in Paraspinous Muscle

The paraspinous muscles run along the length of the spinal cord and assist in motor movement. The blood flow to the paraspinous muscles is relatively small compared to the spinal cord tissue (*170*). To further test the hypothesis that the fiber-optic probe indeed detects blood flow changes in the spinal cord and not the surrounding paraspinous muscle, we hypothesized that when the probe was placed in the paraspinous muscle, there would be no change detected by DCS and DOS upon administering vasopressors or occluding the aorta.

6.2.3.1. Methods

We placed the probe into the lumbar paraspinous muscles of the sheep and measured blood flow 1) after administering vasopressors, and 2) during aortic cross clamping at the T4 and T8 thoracic vertebral levels.

6.2.3.2. Results

With the probe placed in the paraspinous muscle, 400 µg – 800 µg phenylephrine boluses (n = 5) and aortic clamping (n = 2) resulted in no significant changes in flow detected by the optical device. Figure 6.7 below shows a representative example of an experiment wherein the aorta was clamped, with the fiber-optic probe placed in the paraspinous muscle of a single sheep. Average changes in muscle blood flow detected by DCS (0.85 ± 0.1%, n = 7) were not significant. This further confirms that the optical device measures only spinal cord blood flow and no blood flow from surrounding muscle or vessels is contributing to the measurements.

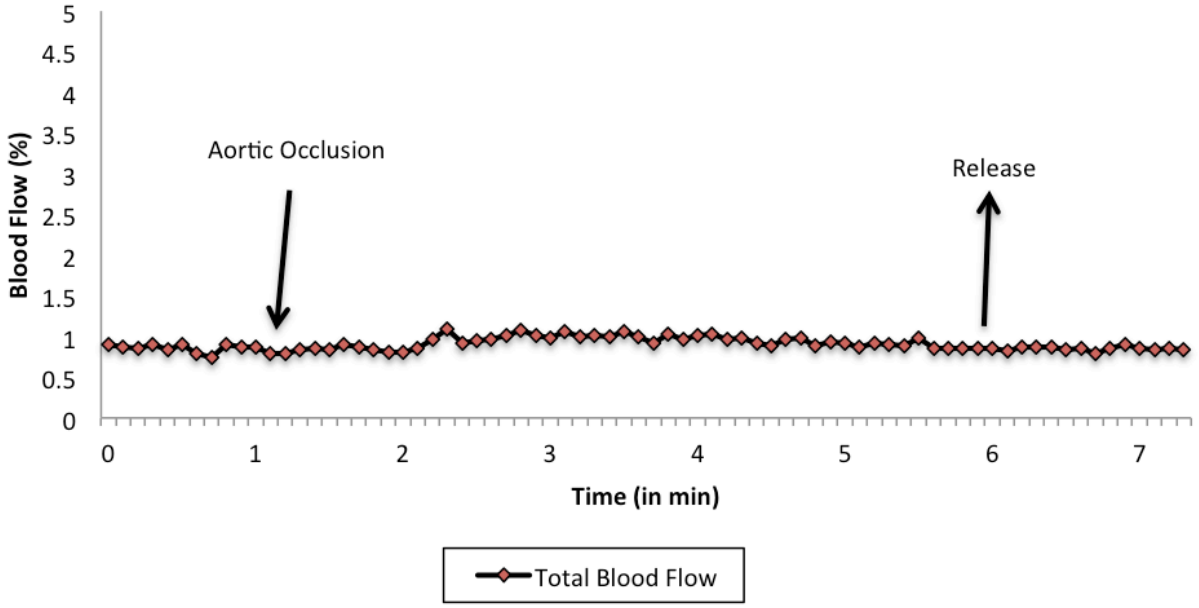

Figure 6.7: The proximal descending thoracic aorta was clamped for 5 minutes, with the fiber-optic probe placed in the paraspinous muscle of a single sheep. No significant changes in muscle blood flow were detected by DCS. The X-axis represents time in minutes and the Y-axis represents the percentage of change in the muscle blood flow detected by DCS.

6.2.3.3. Discussion

It has been established that while paraspinous muscles (and all muscle for that matter) have a rich vascular supply (*171*), baseline muscle blood flow under rest conditions is almost too low to measure by any clinically applicable technique (*172*). Thus, the lack of detection of significant blood flow changes by the optical device upon phenylephrine boluses and aortic clamping when the probe was positioned in the paraspinous muscle can be attributed to this extremely low blood flow and further documents that the paraspinous muscles are not the source of changes in blood flow detected by our device.

Chapter 7

Precision of the Optical Monitor

In this chapter, we attempt to evaluate the precision of the measurements made by the optical monitor and the fiber-optic probe. The precision of the DCS measurements recorded by the optical monitor was evaluated by calculating the within-sheep and between-sheep coefficients of variation and the repeatability value using a root mean square approach.

7.1. Coefficient of Variation and Repeatability

Within- and between-subject coefficients of variation are used to evaluate the precision (*173, 174*). The coefficient of variation is the ratio of the standard deviation of the DCS measurements to their mean. It is calculated from repeated measurements using either a root-mean-square approach or a logarithmic approach. Both methods have been described by Bland-Altman and have been shown to yield similar results (*173*). For our calculations, we used the root mean square approach to calculate the coefficient of variation of DCS measurements collected by the optical monitor between- and within-sheep. The repeatability of the DCS measurements can be calculated via

the within-sheep standard of deviation. All measurements were taken at steady state over four hours with no interventions performed so as to preserve the integrity of the DCS data.

7.1.1. Methods

The precision of the DCS-flow measurement was assessed via analysis of the spinal cord blood flow measured at steady state over four hours in four sheep. The DCS monitor measures one data point every 8 seconds. Here we compared the repeatability of measurements taken every 10 minutes. Within- sheep coefficient of variation and repeatability were calculated as described previously using a root mean square approach (*175*). Briefly, we calculated the square of the coefficient of variation for each sheep separately, found its mean, and took the square root of this mean. We also report the estimated Repeatability Coefficient, calculated as $1.96 \times \sqrt{2}$ x within-sheep standard deviation. The repeatability coefficient could be interpreted as the upper limit of the absolute difference between two measurements on a subject, to differ with 95% probability when the differences are approximately normally distributed.

7.1.2. Results

The DCS BFI values were averaged every ten minutes during four uninterrupted hours of monitoring, in four sheep, to test the repeatability of the device. The mean ± standard deviation, between-sheep and within-sheep coefficient of variation and group Repeatability Coefficient are reported in table 7.1.

Sheep	10 minutes			
	Mean[1] ± SD[1]	Between-sheep coefficient of variation	Within-sheep coefficient of variation	Repeatability coefficient
1	14.02 ± 1.17	24.60%	9.69%	26.80%
2	8.66 ± 1.08			
3	13.23 ± 1.32			
4	9.09 ± 0.68			

Table 7.1: DCS was used to measure the blood flow index in four sheep at steady state (baseline) over 4h. The repeatability coefficient of 26.8% indicates that the absolute difference between two measurements on a sheep would have a 95% probability to differ by no more than 26.8%.
* Means and SDs of each sheep's blood flow index values measured by DCS in corresponding time scales.

7.1.3. Discussion

A point of reference with which to interpret our precision estimates made with DCS can be found via comparison with those made with the 'gold standard' for brain blood flow, Positron Emission Tomography (PET). Precision assessments are typically made under steady state conditions, such as have been reported for PET in brain (*176*). Carroll, in a group of 10 subjects, and comparing 3 measurements within 45 minutes in each subject, conducted on days 1 & 3 reported an inter-subject Reproducibility Coefficient of ± 24% for grey matter and ± 34% for white matter in brain.

Chapter 8

Safety of the Optical Monitor

In this chapter, we address the issue of safety of the laser source. Neurological scoring and histological assessment of the spinal cord tissue samples evaluated safety of the laser source. We calculated if the maximum permissible energy exposure of the spinal cord tissue to the laser source was within safe theoretical limits. Serial neurological evaluations were performed on the sheep for 48 hours and the neurological outcomes scored using a modified Tarlov scale. Once the sheep were euthanized, the spinal cord tissue was collected for histological analysis to determine if any surface tissue injury occurred due to thermal heating.

8.1. Theoretical Calculations of Laser Safety

The fiber-optic probe is comprised of one laser source and two detectors axially located along the probe. The DCS module employs one 785 nm laser diode (CrystaLaser Inc., NV) with an operating power specification of 70 mW. In order to obtain absolute values of oxyhemoglobin and deoxyhemoglobin concentration, the DOS module uses a 70 MHz RF oscillator that sinusoidally drives three laser diodes of 690

nm, 785 nm and 830 nm, with rated operating powers of 30 mW, 70 mW, and 40 mW respectively. Table 8.1 summarizes the modulated optical powers of the lasers at the tissue fiber sources and the duration of exposure to the laser light.

	λ (nm)	**Φ (W)**	**texp (ms)**
DOS	830	0.0149	30
	785	0.0095	30
	690	0.0078	30
DCS	785	0.0282	2500

Table 8.1: Summary of the modulated optical powers (Φ) measured at the output of each of the three Diffuse Optical Spectroscopy (DOS) and one Diffuse Correlation Spectroscopy (DCS) laser sources. λ is the wavelength of the laser sources and t_{exp} is the duration of exposure of tissue to the laser source.

Laser safety can be evaluated using the following factors: power per unit area on the tissue surface and the duty cycle. The power per unit area is dependent on the beam diameter.

Assuming the optical monitor runs continuously for 8 hours (28,800 seconds), we can then derive the exposure energy (E_{exp}). The laser wavelengths of the DCS and DOS sources are in the range of 690 nm – 830 nm (table 8.1). Considering exposure

duration of 10-30,000 seconds, we used the ANSI Z136.1 standard (2014) to calculate the maximum permissible exposure (MPE) for wavelengths ranging from 400 nm – 1400 nm as shown:

$$E = 0.2C_A$$

where E is the maximum permissible exposure in W/cm^2,

C_A, which is a wavelength dependent unit, equals 1 W/cm^2 for λ < 700 nm and $10^{2(\frac{\lambda}{1000}-0.700)}$ (W/cm^2) for λ > 700 nm.

The exposure energy (E_{exp}) of the optical monitor for each laser source was then calculated as follows:

$$E_{\exp} = \phi / \pi r^2$$

where E_{exp} is the exposure energy, i.e. the experimental irradiances of the optical monitor,

Φ is the laser power,

r is the beam radius.

The Maximum Permissible Exposure (MPE) for human skin, retina, and the calculated irradiances of our DCS/DOS device are summarized in table 8.2.

	λ (nm)	Φ (W)	texp (ms)	Duty Cycle	πr^2 (cm^2)	E_{skin} (W/cm^2)	E_{retina} (W/cm^2)	E_{exp} (W/cm^2)
DOS	830	0.0149	30	0.05%	0.096	0.364	0.0018	0.155
	785	0.0095	30	0.05%	0.096	0.296	0.0015	0.099
	690	0.0078	30	0.05%	0.096	0.2	0.001	0.081
DCS	785	0.0282	2500	4.90%	0.096	0.296	0.0015	0.263

Table 8.2: Calculated Energy Deposition (Maximum Permissible Exposure) for human skin, retina and the DCS/DOS monitor.

No standards are currently available for neural tissue like the spinal cord. However, since the retina is a specialized neural tissue with extremely sensitive photoreceptors, we assume that it is much more sensitive than the skin and spinal cord.

The exposure energy we calculated was lesser than the MPE for skin but higher than that specified for the retina.

The spinal cord tissue is much less sensitive than retinal tissue. It is also important to note that the actual power that exits the fiber tips is significantly smaller than the rated operating power due to coupling inefficiencies of the fibers. Therefore the actual power that interacts with the spinal cord tissue is significantly smaller than the power specifications of the laser source.

8.2. Neurological Evaluation

Here, we aimed to characterize the safety profile of the fiber optic probe by evaluating the effect of the laser source on the sheep spinal cord after prolonged placement (4-8 hours). Excessive exposure to the laser source could be associated with thermal heating of surrounding tissue leading to cell death and necrosis.

8.2.1. Methods

We placed the fiber optic probe through open (n=3) and percutaneous (n=8) approaches into the epidural space once the sheep was anesthetized. For both approaches, the study was conducted in a sterile environment since the sheep would be recovered at the end of the experiment. Table 8.3 summarizes the duration of probe placement (4 or 6 hours), placement technique (laminectomy or percutaneous), vertebral level at which the probe was introduced, and its final location on the spinal cord (confirmed fluoroscopically for percutaneous approaches).

Sheep #	Placement Duration	Placement Technique	Probe Entry Level	Probe Tip level
1	4 hours	Laminectomy	L4	L2
2	4 hours	Laminectomy	L5	L2
3	4 hours	Laminectomy	L3	L1
4	4 hours	Percutaneous	L1/L2	T13
5	4 hours	Percutaneous	T14/L1	T12
6	4 hours	Percutaneous	L6/L7	L4
7	6 hours	Percutaneous	L6	L4
8	6 hours	Percutaneous	L6	L3/L4
9	6 hours	Percutaneous	L6	L2
10	6 hours	Percutaneous	L7	L2
11	6 hours	Percutaneous	L8	L3

Table 8.3: Summary of the duration and technique of fiber-optic probe placement, vertebral level at which probe was introduced and the final location of the probe tip on the spinal cord.

The probe was left in the epidural space, in close proximity to the spinal cord for 4-6 hours, without being moved. At the end of the 4-6 hours, the sheep were recovered from the anesthetic and serial neurological evaluations were conducted for 48 hours using the modified Tarlov scale (*177*), as described below in table 8.4. Evaluations were conducted every hour for four hours on the day of the study, and in the morning and evening eight hours apart for the following two days. At the end of the 48 hours, the sheep were euthanized and the spinal cord was resected for histological analysis as

described below in section 8.3. If the sheep were paralyzed or were experiencing discomfort/pain prior to the 48-hour period, they were euthanized and the spinal cord was resected prior to the 48-hour period.

Scale	Motor Function	Deficits
0	No hind limb movement	Paraplegia
1	Hind limb motion without gravity, barely perceptible	Paraplegia
2	Hind limb motion against gravity but unable to support weight	Paraplegia
3	Able to stand, crawl with assistance	Paraplegia
4	Able to walk with assistance	Paraparesis
5	Normal	Paraparesis

Table 8.4: The modified Tarlov scale (*1*) was used for the neurological scoring and evaluation of sheep for a period of 48 hours after surgery.

8.2.2. Results

Sequential neurological monitoring of eleven sheep exposed to the laser source for 4 or 6 hours revealed no signs of paresis or paralysis. The modified Tarlov score was 5 in all cases, which indicated that the sheep were normal and showed no signs of any neurological sequelae.

8.3. Histological Assessment

The spinal cord samples were evaluated for death of neurons and tissue necrosis, hematoma, and physical disruption of tissue at the site where the probe was introduced and where the probe ultimately laid during data collection. This would give us an idea of safety related to probe placement and removal, tissue damage, if any, due to prolonged laser exposure, and the biocompatibility of the probe materials.

8.3.1. Methods

To determine if there were any pathological changes in spinal cord tissue due to surface injury, the tissue samples of the eleven sheep that were euthanized after neurological evaluations were stained with Hematoxylin and Eosin (H&E), with three sections per spinal cord level. A pathologist we collaborated with examined the slides under light microscopy, in a blinded fashion. The vertebral levels at which the spinal cord tissue was retrieved for histological analysis were: level where probe tip was placed (confirmed fluoroscopically), level above and level below probe placement.

To determine if the prolonged exposure to the laser had any effect on the spinal cord tissue, the tissue was evaluated for surface injury. We placed the fiber-optic probe percutaneously through a Tuohy needle placed at the lumbosacral junction in five sheep for 6 hours. The probe was left in place undisturbed and no interventions were performed to maintain the integrity of the pathology data. At the end of the 6 hours, the

sheep were woken up and neurologically evaluated for any signs of paresis/paralysis for 48 hours and scored using a modified Tarlov score. The sheep were then euthanized and the spinal cord tissue was retrieved. The vertebral levels at which the spinal cord tissue was retrieved were: level where probe tip was placed (confirmed fluoroscopically), level above and level below probe placement. A pathologist then evaluated, in a blinded fashion, the spinal cord tissue samples for spinal cord tissue injury, if any, due to prolonged laser exposure.

8.3.2. Results

Histological analysis of the spinal cord tissue samples resected from eleven sheep, at the level where the tissue was exposed to the laser source, showed no signs of surface injury associated with heating due to exposure to the laser source. Figure 8.1 shows an H&E stained spinal cord tissue section observed under the light microscope at 20x magnification with normal neurons and no signs of surface injury associated with thermal heating due to exposure to the laser source. The lack of neurological complications or pathological changes of the spinal cord tissue further indicates a high safety profile of the laser source of our DCS/DOS device.

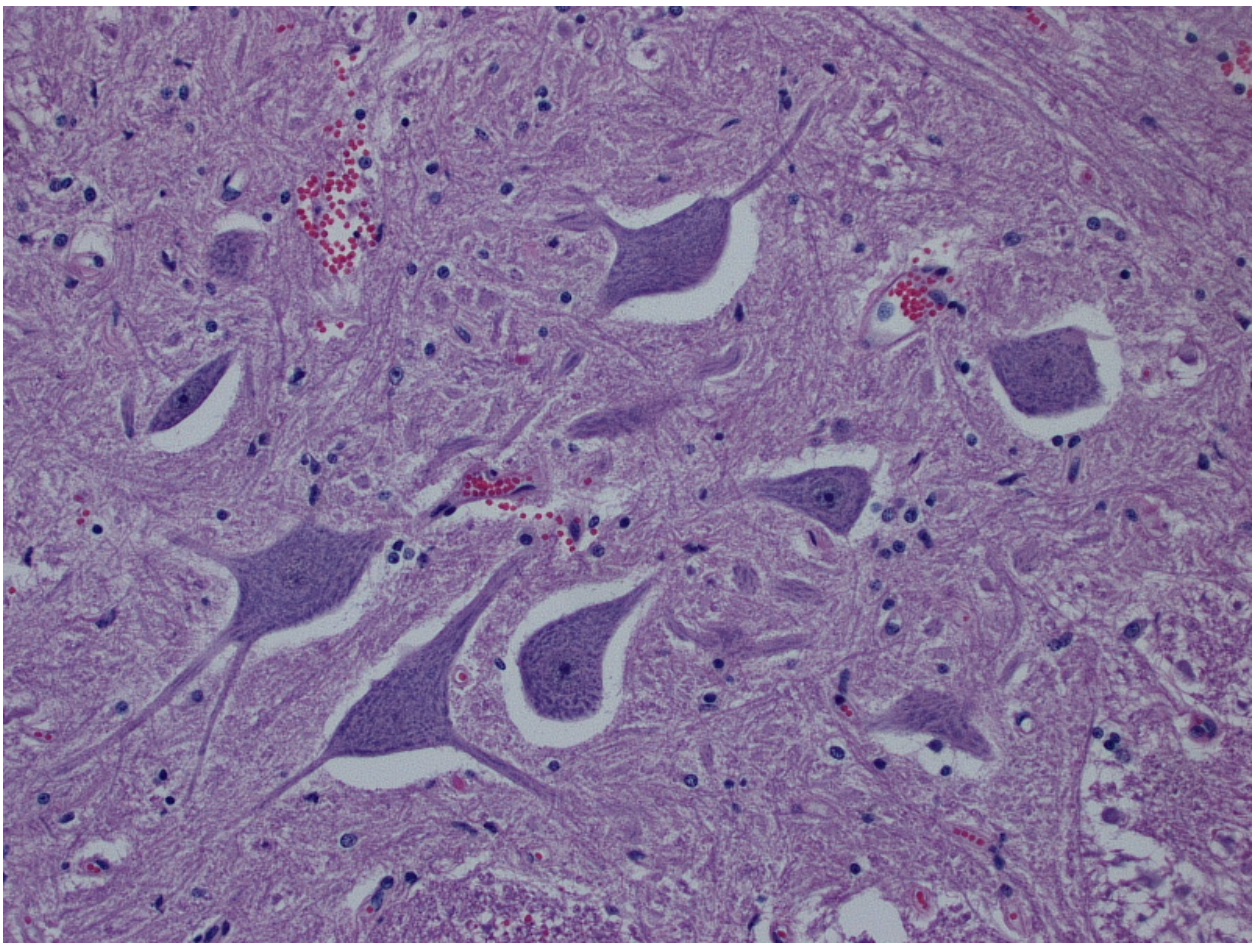

Figure 8.1: Spinal cord tissue stained with H&E showing neurons with normal morphology. Images were taken using a light microscope at 20x magnification.

8.4. *Ex-vivo* evaluation of Tissue Heating

In addition to the theoretical calculations of maximum permissible energy exposure for spinal cord tissue and the neurological and histological evaluations of laser safety, we also performed *ex-vivo* experiments wherein, employing a local thermometry approach, we recorded the tissue heating, if any, due to prolonged laser exposure.

8.4.1. Methods

Spinal cord sections from two sheep were resected after euthanasia. We placed our fiber-optic probe, along with a thermometry probe (Oxford Optronics, UK), co-axially into the core of the resected spinal cord. The tissue temperature was then monitored over 4 hours, with recordings made every hour. The spinal cord tissue, along with the two probes, was suspended in a normal saline bath maintained at 37C to replicate *in vivo* conditions.

8.4.2. Results

There was no increase in temperature over four hours in both of the resected samples of spinal cord tissue (table 8.5). In both samples, the fiber-optic probe and temperature probe were embedded at the tissue site that was exposed to the fiber-optic probe laser source.

Sheep #	**1**	**2**
Initial Temperature	36.8	37.1
Hour 1	36.8	37
Hour 2	37	37
Hour 3	36.9	36.9
Hour 4	37.1	36.9
Mean	**36.92**	**36.98**
Standard Deviation	**0.13**	**0.08**

Table 8.5: No relevant change in temperature of the two resected spinal cord tissue samples was observed after being directly exposed to the laser source of the fiber-optic probe for 4 hours.

8.5. Discussion

Our theoretical calculations of the maximum permissible laser energy that the spinal cord tissue can be exposed to showed that the laser source of our DCS/DOS device should theoretically be safe upon prolonged exposures of eight hours. Experimental evaluation of neurological outcomes and histological analysis of the resected spinal cord tissue in eleven sheep that were exposed to the laser source of our DCS/DOS monitor for prolonged periods (4-6 hours) also revealed no neurological complications or surface injury of the spinal cord. We therefore concluded that there would be minimal thermal heating upon prolonged exposure to the laser source of our DCS/DOS monitor.

Chapter 9

Comparing the Temporal Resolution of the Optical Monitor with Evoked Potential Monitoring

This chapter details the experiments performed to compare the DCS blood flow measurements with the current "gold standard" technique used for monitoring spinal cord integrity in the operating room, namely evoked potential monitoring. Evoked potential monitoring is a neurophysiological monitoring technique and can collect motor evoked potentials (MEPs) and somatosensory evoked potentials (SSEPs). While MEPs monitor the integrity of motor function, SSEPs monitor sensory function. Since they monitor different pathways, they are often used in tandem to get the best overview of spinal cord integrity. Evoked potential monitoring has a number of flaws as discussed in chapter 1, section 1.2. Evoked potentials indirectly assess ischemic injury by monitoring the integrity of the spinal tracts; DCS, on the other hand, directly measures the relative changes in blood flow of the spinal cord. Therefore, it stands to reason that our optical monitor would detect spinal ischemia faster than evoked potential monitoring techniques. In this set of experiments, we hypothesized that the DCS measurement technique is temporally more sensitive to changes in spinal cord blood flow than evoked potentials upon ischemic change induced by aortic occlusion.

9.1. Evoked Potential Monitoring

Intraoperative neuromonitoring (IONM) uses various neurophysiological tests that are used to assess the functional integrity of the central and peripheral nervous systems during surgical procedures that would place these structures at risk for injury (*178*). The purpose of IONM is to provide feedback during surgeries regarding changes in neural function, before the development of ischemia and irreversible neural injury. This permits the surgeon to perform interventions preventing or minimizing the occurrence of post-operative neurological deficit such as paralysis and/or paresis. IONM is currently used during a wide variety of surgical procedures, including spinal surgery, intracranial neurosurgery, interventional neuroradiology, otolaryngology, internal fixation of pelvic fractures, carotid endarterectomies, and thoracic aortic aneurysm repair. The use of IONM for spinal cord integrity has been associated with a decreased rate of paralysis after scoliosis surgery.

Evoked potential monitoring technology is currently the “gold standard” of IONM used in the operating room. Evoked potential monitoring includes somatosensory evoked potentials (SSEPs) and motor evoked potentials (MEPs). Somatosensory evoked potentials (SSEPs) provide direct information regarding dorsally located ascending spinal cord sensory tracts and indirect information regarding integrity of ventrally located spinal cord motor tracts. SSEPs offer no information regarding individual nerve root function. The introduction of transcranial electric MEPs during the last decade addressed the limitations of SSEPs by permitting direct evaluation of the

functional properties of the corticospinal motor tracts, spinal nerve roots, peripheral nerves, and nerve plexuses. Since SSEPs and MEPs monitor different regions, their combination provides global monitoring coverage of spinal cord function.

SSEPs are cortical or subcortical responses to repeated electrical stimulation of a peripheral nerve. Typical nerves stimulated in humans include the posterior tibial nerve (ankle) or median/ulnar nerves (wrist). The figure below summarizes how SSEPs are recorded. Multiple small-amplitude responses are recorded over multiple trials, amplified and filtered to provide a measurable SSEP response. Figure 9.1 below shows the schematic of how SSEP recording is performed.

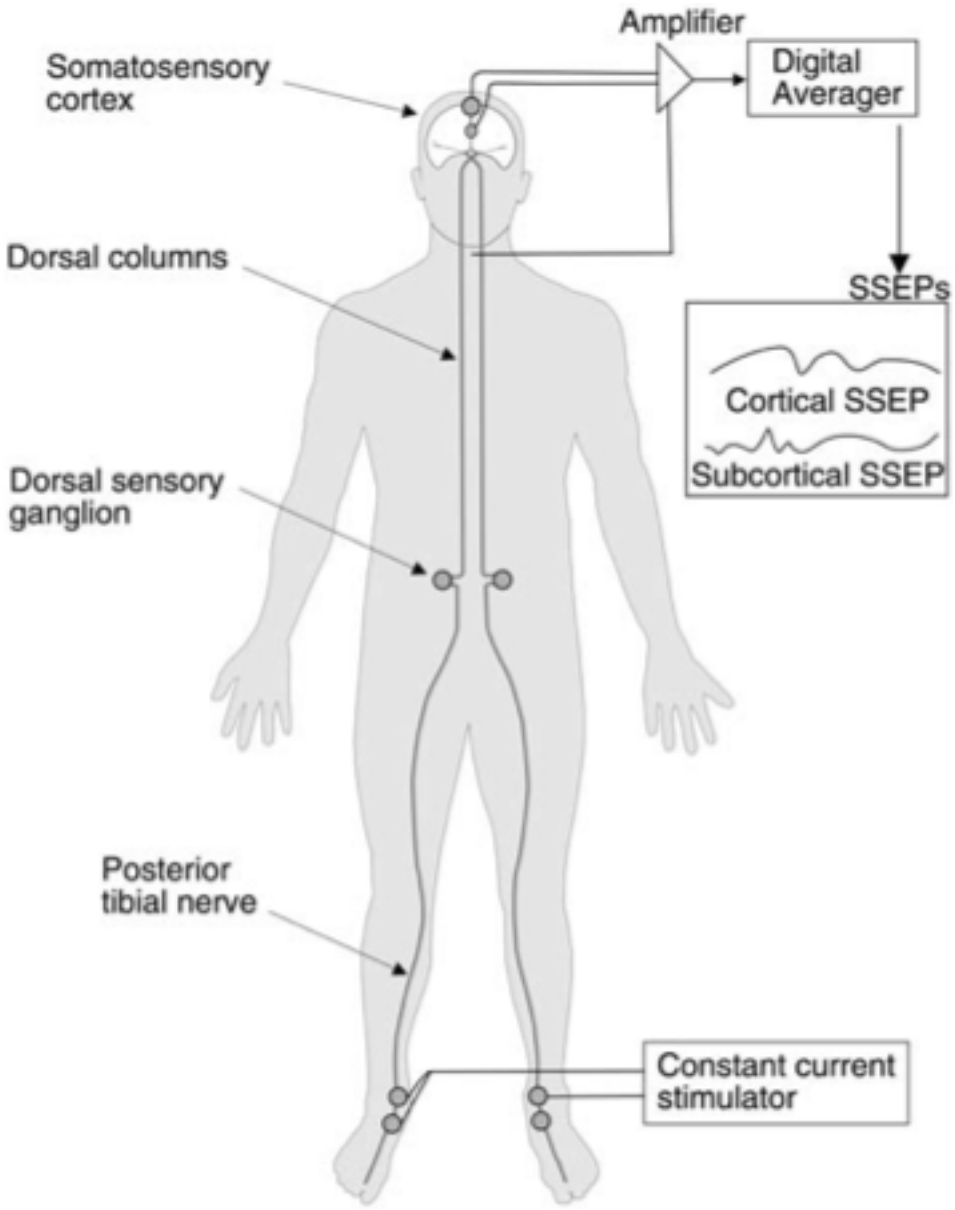

Figure 9.1: Schematic showing somatosensory evoked potential (SSEP) recording in a human subject. The posterior tibial nerves are stimulated and responses recorded from the somatosensory cortex. Figure from (*179*)

MEPs work by assessing spinal cord integrity during surgery by applying high voltage electrical impulses across the skull, to the brain below. The impulses are then conducted through the spinal cord, and out to the arm or leg. Needle electrodes placed in the muscle then detect these signals. Figure 9.2 below shows the schematic of MEP recording.

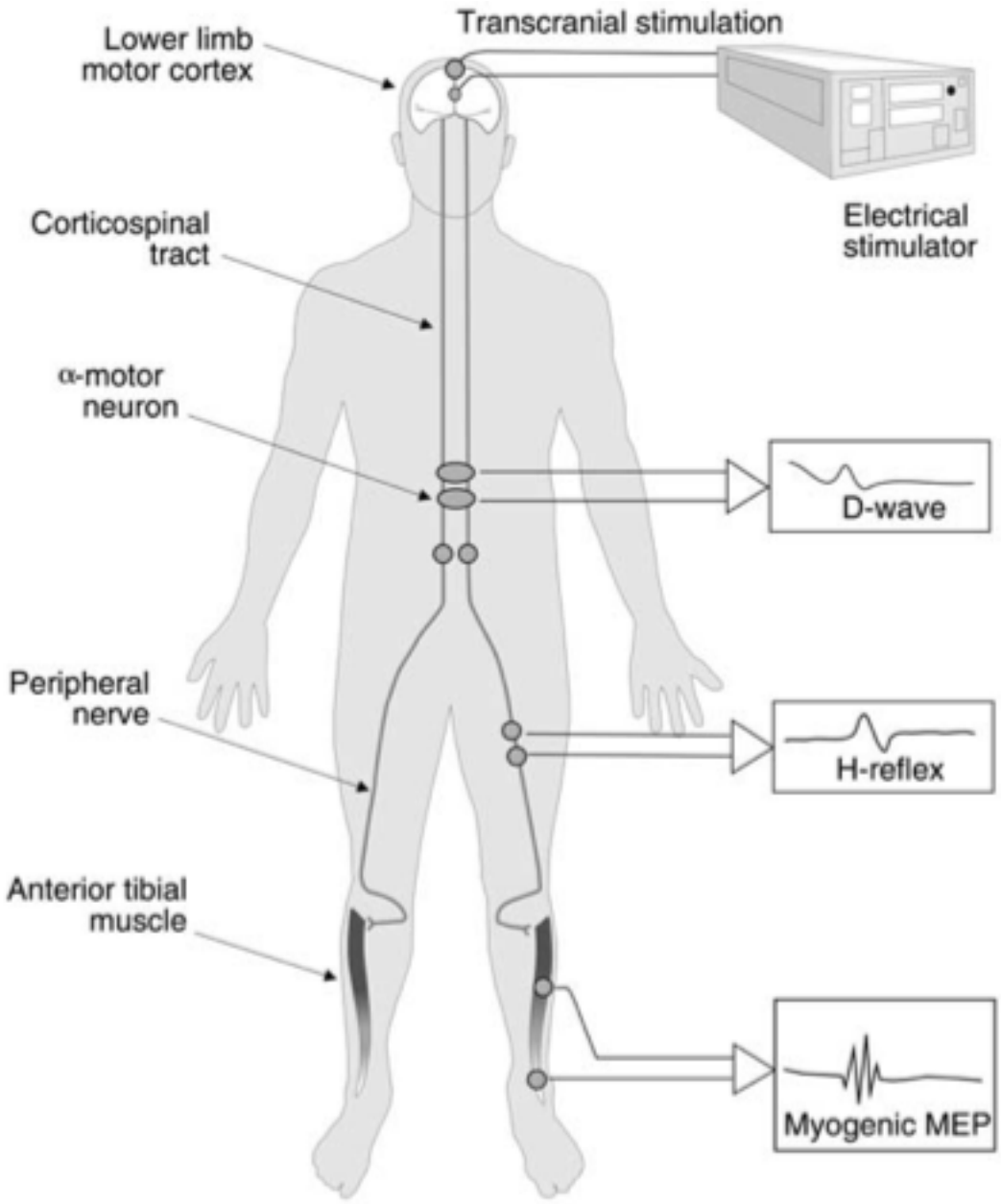

Figure 9.2: Schematic showing motor evoked potential (MEP) recording in a human subject. The motor cortex is stimulated after transcranial electrical stimulation. The signal travels down the corticospinal tract and activates the anterior horn motor neuron. Subdermal needle electrodes placed in the muscles of the extremities record these myogenic MEPs. Figure from (*179*)

Interruption of the anterior circulation would lead to a loss of function in the descending anterior and lateral corticospinal, as well as ascending spinothalamic tracts, which would be detected by MEP electrodes. When the blood flow to the posterior circulation is interrupted, we can expect a loss of function within the ascending tracts, which would be detected by SSEPs. Figure 9.3 below shows the corticospinal tract of the spinal cord.

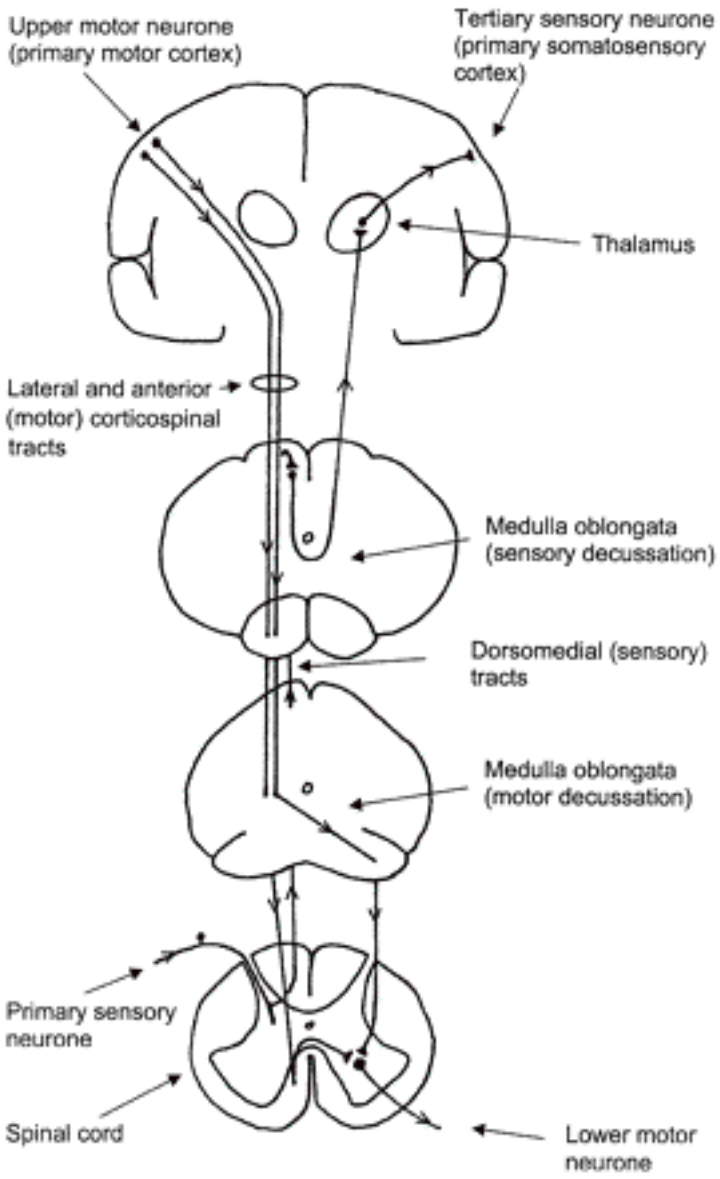

Figure 9.3: Schematic of the spinal tracts through which the evoked potential signals travel. (Raw et al (*180*)).

Signal amplitude (power) and latency (velocity) are recorded during surgery and compared with baseline values. Of the two parameters, amplitude is more relevant since spinal cord injury without amplitude change in evoked potential signal is highly unlikely. Delay in the conduction of the impulse to the extremity, or decrease in

magnitude of the impulse sensed, indicates a decrement in spinal cord integrity. Signal changes may be due to direct spinal cord injury, loss of blood flow to the cord, or both. The ability to discriminate between the two is critical, yet impossible with current technology.

Evoked potential monitoring during vascular and spinal surgery is the current standard of care (*181, 182*). The published range for subjects with electrophysiological changes that developed paraparesis, paraplegia, or quadriplegia varies from 16-40% (*183*). False negative results can occur since the monitoring is pathway specific and any injury not involving that pathway will not be detected by evoked potentials (*70*). Somatosensory and motor evoked potentials do not directly monitor spinal cord hemodynamics; rather, they detect the result of protracted ischemia upon nerve transmission (*184*), and studies have demonstrated that the delay in nerve transmission variation from the onset of ischemia may exceed 20 minutes (*185*). Furthermore, since evoked potential changes can also be influenced by hypothermia, limb ischemia, and anesthetic management (*186*), the management decisions in response to these alerts are difficult. A device that could be used in a complimentary fashion with evoked potentials could eliminate these problems.

For our experiments, we created acute ischemia in the spinal cord of the sheep using two types of interventions: vascular models where the aorta was occluded (described in section 5.3) and spinal cord distraction models (section 6.2.2.). The sheep were monitored by the DCS/DOS device and MEP monitoring simultaneously. The timing of both devices in detecting the onset of ischemia from the time of intervention performed was compared. For DCS/DOS, we considered ischemia to have set in when the blood flow dropped by 50% from baseline. For evoked potentials, we used the clinically accepted standard of an 80% decrease in evoked potential signal amplitude.

9.2. Methods

Evoked potential monitoring experiments were performed with assistance from an electroencephalography technician at Stony Brook University hospital.

MEP monitoring required transcranial stimulation of the motor cortex by electrical stimuli involving 3-7 pulses of 100-400 volts that produced a response that traveled down the corticospinal tracts and which generated a measurable muscle response, the compound muscle action potential. The disposable subdermal needle electrodes were placed according to the International 10-20 system (*187*). The motor stimulus electrodes were placed a few centimeters behind the Cz plane at C3'-C4'. The motor recording electrodes were placed in the semi-membranous or gastrocnemius muscles in the lower

extremities and in the flexor carpi ulnaris for upper limb MEP recording. The anesthetic agent was ketamine, 200 mg/hr via infusion during these experiments. No muscle relaxant was used so as to not compromise the motor and somatosensory evoked potential amplitudes (*188*). Figure 9.4 shows the placement of the motor electrodes on the sheep's cortex that we employed for our experiments.

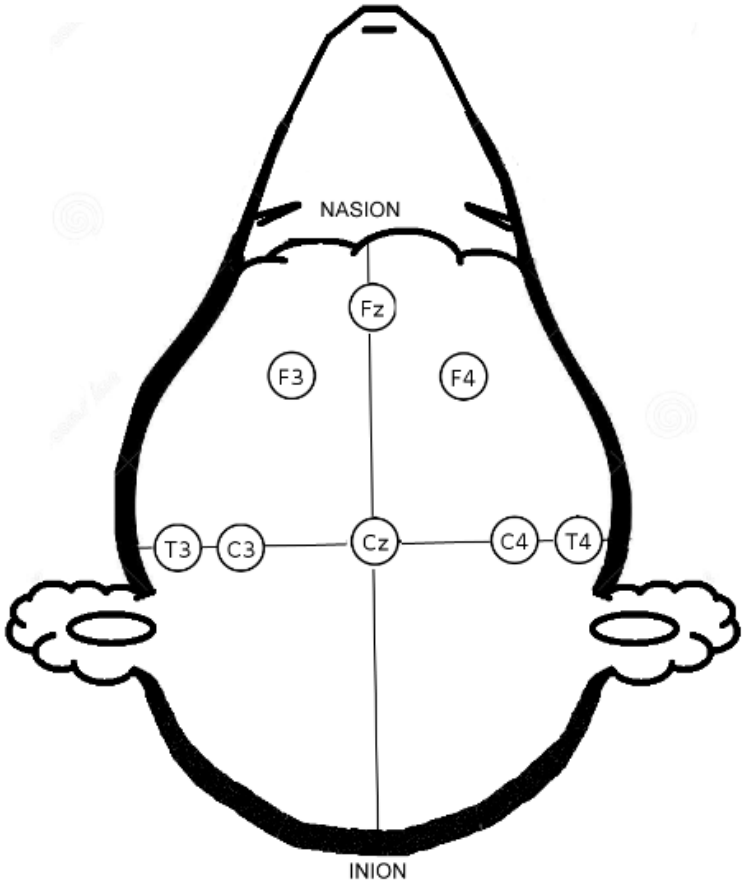

Figure 9.4: The motor electrodes were placed on the sheep head according to the international 10-20 placement system.

The most commonly used criteria for alerting to a clinically relevant event during MEP monitoring is either a 100% or 80% loss of signal (*189*). Therefore, the time for DCS to detect a 50% drop in blood flow from baseline was compared with the time for motor evoked potential (MEP) signals to drop by 80% from baseline upon performing an aortic clamping in three sheep. The time for the DCS and evoked potential signal to recover back to baseline after unclamping was also compared.

Non-parametric Wilcoxon signed rank test was used to determine if the time taken by DCS and evoked potentials to drop/recover upon aortic clamping/unclamping was statistically different. Data were analyzed using JMP statistical software (SAS Institute, NC).

9.3. Results

Upon proximal aortic clamping in three sheep, it took an average of 2 ± 0.8 minutes for the blood flow detected by DCS to drop by 50% from baseline. The mean time taken for an 80% drop in amplitude of evoked potential signal was 16 ± 4 min, an example of which is shown in figure 9.5. After the clamp was released, the DCS signal returned back to baseline in 1 ± 0.2 min, while it took approximately 18 ± 5 minutes for evoked potentials to return back to baseline. Non-parametric Wilcoxon signed rank tests showed statistically significant difference between the time taken for DCS and evoked potential signals to drop upon clamping ($p = 0.03$) and recover upon unclamping ($p = 0.03$).

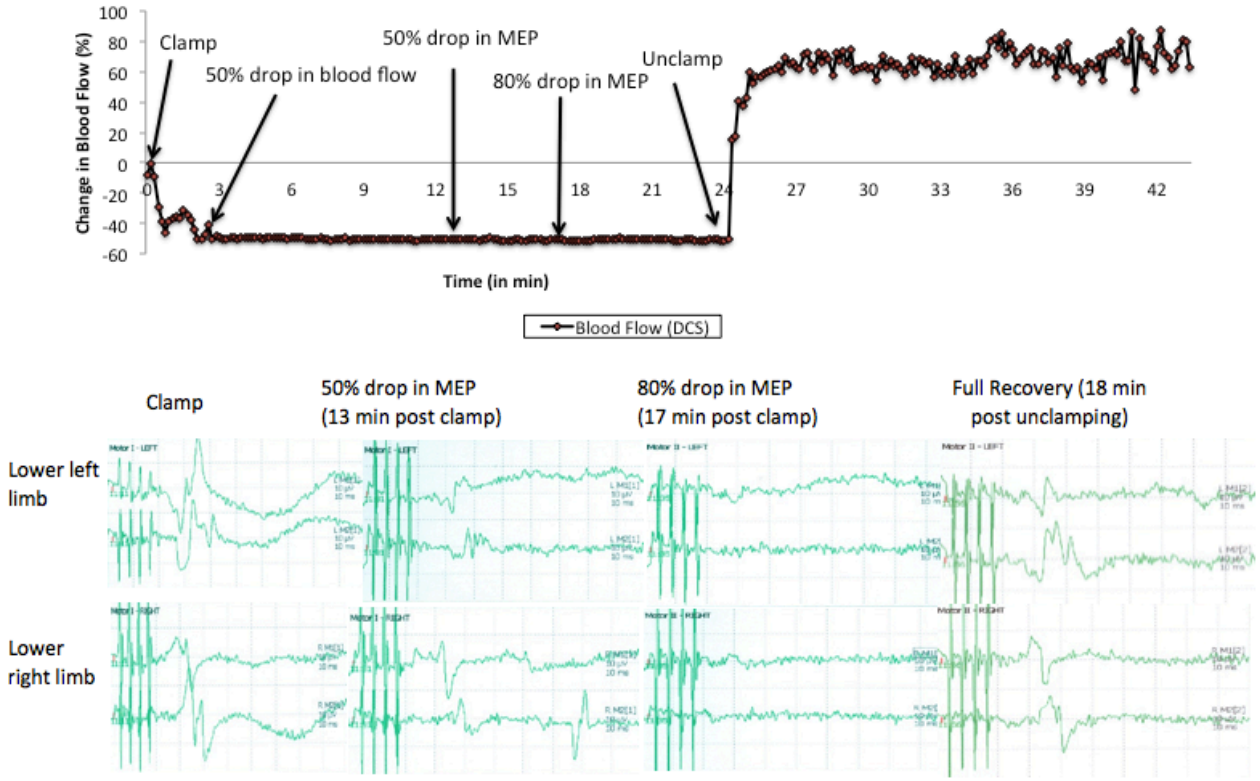

Figure 9.5: In three sheep, the time taken by Diffuse Correlation Spectroscopy (DCS) to detect a 50% decrease in blood flow from baseline was compared with the time taken by motor evoked potential (MEP) monitoring to detect an 80% decrease in its signal upon aortic clamping. As shown in this representative example, DCS took 3 min to detect a 50% decrease in blood flow from baseline, while it took 17 minutes to detect an 80% loss of amplitude in MEP signal. While DCS detected blood flow recovery immediately (1 min), it took the MEP signal 18 minutes to return back to baseline after the clamp was removed.

9.4. Discussion

In addition to the high degree of sensitivity of the DCS/DOS device that we have reported, the immediacy of the response to aortic clamping deserves special note. Published reports suggest that current evoked potential monitoring technology produces a lag from the insult to alert, and this lag time can approach 20min (*183*). Our data in sheep confirm this. This difference in response to time between DCS and evoked potentials in alerting the surgeon or anesthesiologist to the decrement in blood flow may have important implications for a surgeon attempting to address the ischemia. The clinical impact of such a delay is compounded by the fact that evoked potentials are also associated with a profound delay in recovery of signal. On the contrary, DCS immediately identifies the restoration of flow. Therefore, DCS may have important advantages over evoked potentials in alerting the surgeon to the onset of ischemia as well as signaling when an attempt at restoration has been successful.

Because the optical device measures relative changes in blood flow, it is not likely to be affected by patient temperature, anesthetic agents, or decrement in blood flow to a lower limb, which commonly frustrate evoked potential monitoring. When used in conjunction with evoked potential monitoring, this device could allow for the ability to discriminate between cord and nerve root injury during spine surgery. Used in tandem, they could also better discriminate the contribution of anesthetics and peripheral ischemic issues, such as an ischemic leg during femoral cannulation for cardiopulmonary bypass, that frequently impair evoked potential signals unilaterally.

Chapter 10

Conclusions and Future Work

Probes when placed by open approaches might be used by a neurosurgeon or orthopedic spine surgeon or when placed *via* percutaneous approaches might be used when spine surgery was not planned, such as for aortic surgery, or in the neurocritical care environment to manage spine injury before surgery. The demonstrated ability to place the highly flexible DCS/DOS probe using a percutaneous approach that replicates the approach to the placement of epidural catheters may lower the barrier to acceptance of the device by anesthesiologists and critical care specialists.

The shorter S-D separations are biased to interrogating and measuring flow in the posterior circulation closest to the probe, whereas the longer separations would be biased toward interrogating and measuring flow in the more distant anterior circulation. In this study, we have averaged the flow and oxygenation measured by both detectors. Working out the ability of the probe to spatially resolve flow and oxygenation in the anterior and posterior circulations is a long-term goal of this research.

Although the DCS/DOS device described herein may offer more immediate and reliable detection of spinal cord ischemia than conventional methods such as evoked potentials, it is reasonable to question whether interventions designed to alleviate detected ischemia may actually have the capacity to reverse the ischemic insult, and

whether improved monitoring might actually impact outcome. It would be ideal to know before committing to aortic grafting just what impact the graft might have upon spinal cord blood flow. The device described herein could be placed before surgery or at least before commitment to grafting. A trial aortic occlusion or stent deployment might be performed, during which spinal cord blood flow is monitored. An “unsafe” drop in spinal cord blood flow might allow the surgeon to reevaluate the neurologic risk associated with the proposed procedure.

Finally, because the probe can remain in place after surgery, it offers the opportunity for postoperative monitoring and management of patients in the intensive care unit, providing feedback for the impact of cerebrospinal fluid drainage or hemodynamic support upon spinal cord blood flow and oxygenation.

Bibliography

1. P. G. Popovich *et al.*, A reassessment of a classic neuroprotective combination therapy for spinal cord injured rats: LPS/pregnenolone/indomethacin. *Exp Neurol* **233**, 677-685 (2012).
2. M. E. van den Berg, J. M. Castellote, I. Mahillo-Fernandez, J. de Pedro-Cuesta, Incidence of spinal cord injury worldwide: a systematic review. *Neuroepidemiology* **34**, 184-192; discussion 192 (2010).
3. D. Kattail, J. C. Furlan, M. G. Fehlings, Epidemiology and clinical outcomes of acute spine trauma and spinal cord injury: experience from a specialized spine trauma center in Canada in comparison with a large national registry. *J Trauma* **67**, 936-943 (2009).
4. M. Wyndaele, J. J. Wyndaele, Incidence, prevalence and epidemiology of spinal cord injury: what learns a worldwide literature survey? *Spinal Cord* **44**, 523-529 (2006).
5. D. Kattail, J. C. Furlan, M. G. Fehlings, Epidemiology and clinical outcomes of acute spine trauma and spinal cord injury: experience from a specialized spine trauma center in Canada in comparison with a large national registry. *J Trauma* **67**, 936-943 (2009).
6. D. A. Becker, M. L. McGarvey, C. Rojvirat, J. E. Bavaria, S. R. Messe, Predictors of outcome in patients with spinal cord ischemia after open aortic repair. *Neurocrit Care* **18**, 70-74 (2013).
7. M. F. Conrad, R. S. Crawford, J. K. Davison, R. P. Cambria, Thoracoabdominal aneurysm repair: a 20-year perspective. *Ann Thorac Surg* **83**, S856-861; discussion S890-852 (2007).
8. S. R. Messe *et al.*, Neurologic outcomes from high risk descending thoracic and thoracoabdominal aortic operations in the era of endovascular repair. *Neurocrit Care* **9**, 344-351 (2008).
9. G. C. Hughes, N. D. Andersen, J. M. Hanna, R. L. McCann, Thoracoabdominal aortic aneurysm: hybrid repair outcomes. *Annals of cardiothoracic surgery* **1**, 311-319 (2012).
10. D. R. Wong *et al.*, Open repair of thoracoabdominal aortic aneurysm in the modern surgical era: contemporary outcomes in 509 patients. *Journal of the American College of Surgeons* **212**, 569-579; discussion 579-581 (2011).
11. C. D. Etz *et al.*, Thoracic and thoracoabdominal aneurysm repair: is reimplantation of spinal cord arteries a waste of time? *The Annals of thoracic surgery* **82**, 1670-1677 (2006).
12. S. N. Khan, G. Stansby, Cerebrospinal fluid drainage for thoracic and thoracoabdominal aortic aneurysm surgery. *The Cochrane database of systematic reviews* **10**, CD003635 (2012).
13. J. S. Coselli, J. Bozinovski, S. A. LeMaire, Open surgical repair of 2286 thoracoabdominal aortic aneurysms. *Ann Thorac Surg* **83**, S862-864; discussion S890-862 (2007).
14. J. S. Coselli, J. Bozinovski, S. A. LeMaire, Open surgical repair of 2286 thoracoabdominal aortic aneurysms. *Ann Thorac Surg* **83**, S862-864; discussion S890-862 (2007).
15. C. G. Patil, T. S. Patil, S. P. Lad, M. Boakye, Complications and outcomes after spinal cord tumor resection in the United States from 1993 to 2002. *Spinal Cord* **46**, 375-379 (2008).

16. D. L. Reames *et al.*, Complications in the surgical treatment of 19,360 cases of pediatric scoliosis: a review of the Scoliosis Research Society Morbidity and Mortality database. *Spine (Phila Pa 1976)* **36**, 1484-1491 (2011).
17. F. Pastorelli *et al.*, The prevention of neural complications in the surgical treatment of scoliosis: the role of the neurophysiological intraoperative monitoring. *Eur Spine J* **20 Suppl 1**, S105-114 (2011).
18. H. N. Modi, S. W. Suh, J. H. Yang, J. Y. Yoon, False-negative transcranial motor-evoked potentials during scoliosis surgery causing paralysis: a case report with literature review. *Spine (Phila Pa 1976)* **34**, E896-900 (2009).
19. H. N. Modi, S. W. Suh, J. H. Yang, J. Y. Yoon, False-negative transcranial motor-evoked potentials during scoliosis surgery causing paralysis: a case report with literature review. *Spine (Phila Pa 1976)* **34**, E896-900 (2009).
20. F. Pastorelli *et al.*, The prevention of neural complications in the surgical treatment of scoliosis: the role of the neurophysiological intraoperative monitoring. *Eur Spine J* **20 Suppl 1**, S105-114 (2011).
21. D. L. Reames *et al.*, Complications in the surgical treatment of 19,360 cases of pediatric scoliosis: a review of the Scoliosis Research Society Morbidity and Mortality database. *Spine (Phila Pa 1976)* **36**, 1484-1491 (2011).
22. J. S. Krause, J. L. Coker, Aging after spinal cord injury: A 30-year longitudinal study. *J Spinal Cord Med* **29**, 371-376 (2006).
23. C. Pflaum, G. McCollister, D. J. Strauss, R. M. Shavelle, M. J. DeVivo, Worklife after traumatic spinal cord injury. *J Spinal Cord Med* **29**, 377-386 (2006).
24. K. Whalley Hammell, Quality of life after spinal cord injury: a meta-synthesis of qualitative findings. *Spinal Cord* **45**, 124-139 (2007).
25. R. J. Dumont *et al.*, Acute spinal cord injury, part I: pathophysiologic mechanisms. *Clin Neuropharmacol* **24**, 254-264 (2001).
26. R. J. Dumont *et al.*, Acute spinal cord injury, part II: contemporary pharmacotherapy. *Clin Neuropharmacol* **24**, 265-279 (2001).
27. J. R. Dimar *et al.*, Predictors of complications after spinal stabilization of thoracolumbar spine injuries. *J Trauma* **69**, 1497-1500 (2010).
28. J. C. Furlan, V. Noonan, D. W. Cadotte, M. G. Fehlings, Timing of decompressive surgery of spinal cord after traumatic spinal cord injury: an evidence-based examination of pre-clinical and clinical studies. *J Neurotrauma* **28**, 1371-1399 (2011).
29. R. Gupta *et al.*, Advances in the management of spinal cord injury. *J Am Acad Orthop Surg* **18**, 210-222 (2010).
30. J. R. Wilson, M. G. Fehlings, Emerging approaches to the surgical management of acute traumatic spinal cord injury. *Neurotherapeutics* **8**, 187-194 (2011).
31. C. A. Oyinbo, Secondary injury mechanisms in traumatic spinal cord injury: a nugget of this multiply cascade. *Acta Neurobiol Exp (Wars)* **71**, 281-299 (2011).
32. X. Jia, R. G. Kowalski, D. M. Sciubba, R. G. Geocadin, Critical Care of Traumatic Spinal Cord Injury. *J Intensive Care Med*, (2011).
33. P. A. Findley, R. Banerjea, U. Sambamoorthi, Excess mortality associated with mental illness and substance use disorders among veteran clinic users with spinal cord injury. *Disabil Rehabil* **33**, 1608-1615 (2011).
34. D. J. Strauss, M. J. Devivo, D. R. Paculdo, R. M. Shavelle, Trends in life expectancy after spinal cord injury. *Arch Phys Med Rehabil* **87**, 1079-1085 (2006).

35. R. Banerjea, P. A. Findley, B. Smith, T. Findley, U. Sambamoorthi, Co-occurring medical and mental illness and substance use disorders among veteran clinic users with spinal cord injury patients with complexities. *Spinal Cord* **47**, 789-795 (2009).
36. B. M. Smith, S. L. LaVela, F. M. Weaver, Health-related quality of life for veterans with spinal cord injury. *Spinal Cord* **46**, 507-512 (2008).
37. D. D. French *et al.*, Health care costs for patients with chronic spinal cord injury in the Veterans Health Administration. *J Spinal Cord Med* **30**, 477-481 (2007).
38. W. Yu, B. Smith, S. Kim, A. Chow, F. M. Weaver, Major medical conditions and VA healthcare costs near end of life for veterans with spinal cord injuries and disorders. *J Rehabil Res Dev* **45**, 831-839 (2008).
39. R. K. Greenberg *et al.*, Contemporary analysis of descending thoracic and thoracoabdominal aneurysm repair: a comparison of endovascular and open techniques. *Circulation* **118**, 808-817 (2008).
40. S. R. Messe *et al.*, Neurologic outcomes from high risk descending thoracic and thoracoabdominal aortic operations in the era of endovascular repair. *Neurocrit Care* **9**, 344-351 (2008).
41. C. Bafort *et al.*, Predicting spinal cord ischemia before endovascular thoracoabdominal aneurysm repair: monitoring somatosensory evoked potentials. *J Endovasc Ther* **9**, 289-294 (2002).
42. E. C. Gravereaux *et al.*, Risk of spinal cord ischemia after endograft repair of thoracic aortic aneurysms. *J Vasc Surg* **34**, 997-1003 (2001).
43. A. T. Cheung *et al.*, Strategies to manage paraplegia risk after endovascular stent repair of descending thoracic aortic aneurysms. *Ann Thorac Surg* **80**, 1280-1288; discussion 1288-1289 (2005).
44. B. Lamme, I. C. de Jonge, J. A. Reekers, B. A. de Mol, R. Balm, Endovascular treatment of thoracic aortic pathology: feasibility and mid-term results. *Eur J Vasc Endovasc Surg* **25**, 532-539 (2003).
45. M. S. Makaroun *et al.*, Endovascular treatment of thoracic aortic aneurysms: results of the phase II multicenter trial of the GORE TAG thoracic endoprosthesis. *J Vasc Surg* **41**, 1-9 (2005).
46. V. Lepore *et al.*, Treatment of descending thoracic aneurysms by endovascular stent grafting. *J Card Surg* **18**, 436-443 (2003).
47. K. Tabayashi, Spinal cord protection during thoracoabdominal aneurysm repair. *Surg Today* **35**, 1-6 (2005).
48. J. S. Coselli, S. A. LeMaire, Z. C. Schmittling, C. Koksoy, Cerebrospinal fluid drainage in thoracoabdominal aortic surgery. *Semin Vasc Surg* **13**, 308-314 (2000).
49. R. P. Cambria *et al.*, Epidural cooling for spinal cord protection during thoracoabdominal aneurysm repair: A five-year experience. *J Vasc Surg* **31**, 1093-1102 (2000).
50. C. D. Etz *et al.*, Spinal cord blood flow and ischemic injury after experimental sacrifice of thoracic and abdominal segmental arteries. *Eur J Cardiothorac Surg* **33**, 1030-1038 (2008).
51. J. S. Coselli, S. A. LeMaire, C. Koksoy, Z. C. Schmittling, P. E. Curling, Cerebrospinal fluid drainage reduces paraplegia after thoracoabdominal aortic aneurysm repair: results of a randomized clinical trial. *Journal of vascular surgery* **35**, 631-639 (2002).

52. C. S. Cina *et al.*, Cerebrospinal fluid drainage to prevent paraplegia during thoracic and thoracoabdominal aortic aneurysm surgery: a systematic review and meta-analysis. *J Vasc Surg* **40**, 36-44 (2004).
53. E. Weigang *et al.*, Perioperative management to improve neurologic outcome in thoracic or thoracoabdominal aortic stent-grafting. *Ann Thorac Surg* **82**, 1679-1687 (2006).
54. S. N. Khan, G. Stansby, Cerebrospinal fluid drainage for thoracic and thoracoabdominal aortic aneurysm surgery. *Cochrane Database Syst Rev*, CD003635 (2004).
55. J. S. Coselli, S. A. LeMaire, C. Koksoy, Z. C. Schmittling, P. E. Curling, Cerebrospinal fluid drainage reduces paraplegia after thoracoabdominal aortic aneurysm repair: results of a randomized clinical trial. *J Vasc Surg* **35**, 631-639 (2002).
56. G. Melissano, R. Chiesa, Advances in imaging of the spinal cord vascular supply and its relationship with paraplegia after aortic interventions. A review. *Eur J Vasc Endovasc Surg* **38**, 567-577 (2009).
57. R. Shi, J. D. Pryor, Pathological changes of isolated spinal cord axons in response to mechanical stretch. *Neuroscience* **110**, 765-777 (2002).
58. J. H. Owen, M. Naito, K. H. Bridwell, Relationship among level of distraction, evoked potentials, spinal cord ischemia and integrity, and clinical status in animals. *Spine (Phila Pa 1976)* **15**, 852-857 (1990).
59. M. G. Fehlings, C. H. Tator, R. D. Linden, The relationships among the severity of spinal cord injury, motor and somatosensory evoked potentials and spinal cord blood flow. *Electroencephalogr Clin Neurophysiol* **74**, 241-259 (1989).
60. P. de Haan *et al.*, Efficacy of transcranial motor-evoked myogenic potentials to detect spinal cord ischemia during operations for thoracoabdominal aneurysms. *J Thorac Cardiovasc Surg* **113**, 87-100; discussion 100-101 (1997).
61. L. Pelosi *et al.*, Combined monitoring of motor and somatosensory evoked potentials in orthopaedic spinal surgery. *Clin Neurophysiol* **113**, 1082-1091 (2002).
62. M. R. Nuwer *et al.*, Evidence-based guideline update: intraoperative spinal monitoring with somatosensory and transcranial electrical motor evoked potentials: report of the Therapeutics and Technology Assessment Subcommittee of the American Academy of Neurology and the American Clinical Neurophysiology Society. *Neurology* **78**, 585-589 (2012).
63. M. Kawaguchi, H. Furuya, Intraoperative spinal cord monitoring of motor function with myogenic motor evoked potentials: a consideration in anesthesia. *J Anesth* **18**, 18-28 (2004).
64. P. Costa *et al.*, Somatosensory- and motor-evoked potential monitoring during spine and spinal cord surgery. *Spinal Cord* **45**, 86-91 (2007).
65. V. Deletis, F. Sala, Intraoperative neurophysiological monitoring of the spinal cord during spinal cord and spine surgery: a review focus on the corticospinal tracts. *Clin Neurophysiol* **119**, 248-264 (2008).
66. M. Mahmoud *et al.*, Susceptibility of transcranial electric motor-evoked potentials to varying targeted blood levels of dexmedetomidine during spine surgery. *Anesthesiology* **112**, 1364-1373 (2010).
67. S. Deiner, Highlights of anesthetic considerations for intraoperative neuromonitoring. *Semin Cardiothorac Vasc Anesth* **14**, 51-53 (2010).

68. A. C. Wang, K. D. Than, A. B. Etame, F. La Marca, P. Park, Impact of anesthesia on transcranial electric motor evoked potential monitoring during spine surgery: a review of the literature. *Neurosurg Focus* **27**, E7 (2009).
69. R. P. Lesser *et al.*, Postoperative neurological deficits may occur despite unchanged intraoperative somatosensory evoked potentials. *Ann Neurol* **19**, 22-25 (1986).
70. J. Y. Hong *et al.*, False negative and positive motor evoked potentials in one patient: is single motor evoked potential monitoring reliable method? A case report and literature review. *Spine (Phila Pa 1976)* **35**, E912-916 (2010).
71. C. ter Wolbeek *et al.*, Value and pitfalls of neurophysiological monitoring in thoracic and thoracoabdominal aortic replacement and endovascular repair. *Thorac Cardiovasc Surg* **58**, 260-264 (2010).
72. J. Lips, P. de Haan, G. J. Bouma, M. J. Jacobs, C. J. Kalkman, Delayed detection of motor pathway dysfunction after selective reduction of thoracic spinal cord blood flow in pigs. *J Thorac Cardiovasc Surg* **123**, 531-538 (2002).
73. V. K. Nielsen, T. Kardel, Temporospatial effects on orthodromic sensory potential propagation during ischemia. *Ann Neurol* **9**, 597-604 (1981).
74. M. Kakinohana *et al.*, Delayed response of transcranial myogenic motor-evoked potential monitoring to spinal cord ischemia during repair surgery for descending thoracic aortic aneurysm. *J Anesth* **22**, 304-307 (2008).
75. M. Simonovich, E. Barbiro-Michaely, A. Mayevsky, Real-time monitoring of mitochondrial NADH and microcirculatory blood flow in the spinal cord. *Spine (Phila Pa 1976)* **33**, 2495-2502 (2008).
76. P. J. Lindsberg, J. T. O'Neill, I. A. Paakkari, J. M. Hallenbeck, G. Feuerstein, Validation of laser-Doppler flowmetry in measurement of spinal cord blood flow. *Am J Physiol* **257**, H674-680 (1989).
77. S. J. Schneider, A. D. Rosenthal, B. M. Greenberg, J. Danto, A preliminary report on the use of laser-Doppler flowmetry during tethered spinal cord release. *Neurosurgery* **32**, 214-217; discussion 217-218 (1993).
78. H. Westergren, M. Farooque, Y. Olsson, A. Holtz, Spinal cord blood flow changes following systemic hypothermia and spinal cord compression injury: an experimental study in the rat using Laser-Doppler flowmetry. *Spinal Cord* **39**, 74-84 (2001).
79. A. R. Baker, T. A. Collins, R. W. Porter, C. Kidd, Laser Doppler study of porcine cauda equina blood flow. The effect of electrical stimulation of the rootlets during single and double site, low pressure compression of the cauda equina. *Spine (Phila Pa 1976)* **20**, 660-664 (1995).
80. A. N. Obeid, N. J. Barnett, G. Dougherty, G. Ward, A critical review of laser Doppler flowmetry. *J Med Eng Technol* **14**, 178-181 (1990).
81. K. U. Frerichs, G. Z. Feuerstein, Laser-Doppler flowmetry. A review of its application for measuring cerebral and spinal cord blood flow. *Mol Chem Neuropathol* **12**, 55-70 (1990).
82. M. F. Swiontkowski, Surgical approaches in osteomyelitis. Use of laser Doppler flowmetry to determine nonviable bone. *Infect Dis Clin North Am* **4**, 501-512 (1990).
83. A. Jakobsson, G. E. Nilsson, Prediction of sampling depth and photon pathlength in laser Doppler flowmetry. *Med Biol Eng Comput* **31**, 301-307 (1993).
84. T. F. Cermik *et al.*, Assessment of regional blood flow in cerebral motor and sensory areas in patients with spinal cord injury. *Brain Res* **1109**, 54-59 (2006).

85. G. Duhamel *et al.*, Mouse lumbar and cervical spinal cord blood flow measurements by arterial spin labeling: sensitivity optimization and first application. *Magn Reson Med* **62**, 430-439 (2009).
86. A. L. Estrera *et al.*, Cerebrospinal fluid drainage during thoracic aortic repair: safety and current management. *Ann Thorac Surg* **88**, 9-15; discussion 15 (2009).
87. R. E. Grady, T. T. Horlocker, R. D. Brown, P. M. Maxson, D. R. Schroeder, Neurologic complications after placement of cerebrospinal fluid drainage catheters and needles in anesthetized patients: implications for regional anesthesia. Mayo Perioperative Outcomes Group. *Anesth Analg* **88**, 388-392 (1999).
88. T. T. Horlocker, M. D. Abel, J. M. Messick, Jr., D. R. Schroeder, Small risk of serious neurologic complications related to lumbar epidural catheter placement in anesthetized patients. *Anesth Analg* **96**, 1547-1552, table of contents (2003).
89. T. T. Horlocker *et al.*, Neurologic complications of 603 consecutive continuous spinal anesthetics using macrocatheter and microcatheter techniques. Perioperative Outcomes Group. *Anesth Analg* **84**, 1063-1070 (1997).
90. T. T. Horlocker, D. G. McGregor, D. K. Matsushige, D. R. Schroeder, J. A. Besse, A retrospective review of 4767 consecutive spinal anesthetics: central nervous system complications. Perioperative Outcomes Group. *Anesth Analg* **84**, 578-584 (1997).
91. R. G. Wheatley, S. A. Schug, D. Watson, Safety and efficacy of postoperative epidural analgesia. *Br J Anaesth* **87**, 47-61 (2001).
92. M. M. Wynn, M. W. Mell, G. Tefera, J. R. Hoch, C. W. Acher, Complications of spinal fluid drainage in thoracoabdominal aortic aneurysm repair: a report of 486 patients treated from 1987 to 2008. *J Vasc Surg* **49**, 29-34; discussion 34-25 (2009).
93. Y. Kawanishi *et al.*, Usefulness of transcranial motor evoked potentials during thoracoabdominal aortic surgery. *Ann Thorac Surg* **83**, 456-461 (2007).
94. L. A. Bokeriia *et al.*, Surgical methods of protecting the spinal cord during reconstructive operations on the thoracic and thoracoabdominal portions of the aorta. *Angiol Sosud Khir* **14**, 93-99 (2008).
95. A. S. Kogler *et al.*, Fiber-optic Monitoring of Spinal Cord Hemodynamics in Experimental Aortic Occlusion. *Anesthesiology* **123**, 1362-1373 (2015).
96. R. C. Mesquita *et al.*, Optical monitoring and detection of spinal cord ischemia. *PLoS One* **8**, e83370 (2013).
97. A. G. Yodh, Diffuse optics for monitoring brain hemodynamics. *Conference proceedings : ... Annual International Conference of the IEEE Engineering in Medicine and Biology Society. IEEE Engineering in Medicine and Biology Society. Annual Conference* **2009**, 1991-1993 (2009).
98. Y. Lin, L. He, Y. Shang, G. Yu, Noncontact diffuse correlation spectroscopy for noninvasive deep tissue blood flow measurement. *J Biomed Opt* **17**, 010502 (2012).
99. R. C. Mesquita *et al.*, Hemodynamic and metabolic diffuse optical monitoring in a mouse model of hindlimb ischemia. *Biomed Opt Express* **1**, 1173-1187 (2010).
100. F. F. Jo Bsis-Vandervliet, Discovery of the near-infrared window into the body and the early development of near-infrared spectroscopy. *J Biomed Opt* **4**, 392-396 (1999).
101. D. A. Boas, L. E. Campbell, A. G. Yodh, Scattering and Imaging with Diffusing Temporal Field Correlations. *Phys Rev Lett* **75**, 1855-1858 (1995).
102. G. Yu *et al.*, Validation of diffuse correlation spectroscopy for muscle blood flow with concurrent arterial spin labeled perfusion MRI. *Opt Express* **15**, 1064-1075 (2007).

103. S. R. Arridge, M. Cope, D. T. Delpy, The theoretical basis for the determination of optical pathlengths in tissue: temporal and frequency analysis. *Phys Med Biol* **37**, 1531-1560 (1992).
104. D. T. Delpy *et al.*, Estimation of optical pathlength through tissue from direct time of flight measurement. *Phys Med Biol* **33**, 1433-1442 (1988).
105. W. B. Baker *et al.*, Modified Beer-Lambert law for blood flow. *Biomed Opt Express* **5**, 4053-4075 (2014).
106. T. Durduran, R. Choe, W. B. Baker, A. G. Yodh, Diffuse Optics for Tissue Monitoring and Tomography. *Rep Prog Phys* **73**, (2010).
107. G. Strangman, M. A. Franceschini, D. A. Boas, Factors affecting the accuracy of near-infrared spectroscopy concentration calculations for focal changes in oxygenation parameters. *Neuroimage* **18**, 865-879 (2003).
108. T. Durduran *et al.*, Diffuse optical measurement of blood flow, blood oxygenation, and metabolism in a human brain during sensorimotor cortex activation. *Opt Lett* **29**, 1766-1768 (2004).
109. H. W. Wang *et al.*, Quantitative comparison of tissue oxygen and motexafin lutetium uptake by ex vivo and noninvasive in vivo techniques in patients with intraperitoneal carcinomatosis. *J Biomed Opt* **12**, 034023 (2007).
110. R. C. Mesquita *et al.*, Direct measurement of tissue blood flow and metabolism with diffuse optics. *Philos Transact A Math Phys Eng Sci* **369**, 4390-4406 (2011).
111. T. Durduran *et al.*, Optical measurement of cerebral hemodynamics and oxygen metabolism in neonates with congenital heart defects. *J Biomed Opt* **15**, 037004 (2010).
112. S. A. Carp, G. P. Dai, D. A. Boas, M. A. Franceschini, Y. R. Kim, Validation of diffuse correlation spectroscopy measurements of rodent cerebral blood flow with simultaneous arterial spin labeling MRI; towards MRI-optical continuous cerebral metabolic monitoring. *Biomed Opt Express* **1**, 553-565 (2010).
113. M. N. Kim *et al.*, Noninvasive measurement of cerebral blood flow and blood oxygenation using near-infrared and diffuse correlation spectroscopies in critically brain-injured adults. *Neurocrit Care* **12**, 173-180 (2010).
114. E. M. Buckley *et al.*, Cerebral hemodynamics in preterm infants during positional intervention measured with diffuse correlation spectroscopy and transcranial Doppler ultrasound. *Opt Express* **17**, 12571-12581 (2009).
115. N. Roche-Labarbe *et al.*, Noninvasive optical measures of CBV, StO(2), CBF index, and rCMRO(2) in human premature neonates' brains in the first six weeks of life. *Hum Brain Mapp* **31**, 341-352 (2010).
116. T. Durduran *et al.*, Transcranial optical monitoring of cerebrovascular hemodynamics in acute stroke patients. *Opt Express* **17**, 3884-3902 (2009).
117. Y. Shang, T. B. Symons, T. Durduran, A. G. Yodh, G. Yu, Effects of muscle fiber motion on diffuse correlation spectroscopy blood flow measurements during exercise. *Biomed Opt Express* **1**, 500-511 (2010).
118. G. Yu *et al.*, Intraoperative evaluation of revascularization effect on ischemic muscle hemodynamics using near-infrared diffuse optical spectroscopies. *J Biomed Opt* **16**, 027004 (2011).
119. G. Yu *et al.*, Time-dependent blood flow and oxygenation in human skeletal muscles measured with noninvasive near-infrared diffuse optical spectroscopies. *J Biomed Opt* **10**, 024027 (2005).

120. T. Durduran *et al.*, Diffuse optical measurement of blood flow in breast tumors. *Opt Lett* **30**, 2915-2917 (2005).
121. U. Sunar *et al.*, Noninvasive diffuse optical measurement of blood flow and blood oxygenation for monitoring radiation therapy in patients with head and neck tumors: a pilot study. *J Biomed Opt* **11**, 064021 (2006).
122. G. Yu *et al.*, Real-time in situ monitoring of human prostate photodynamic therapy with diffuse light. *Photochem Photobiol* **82**, 1279-1284 (2006).
123. R. C. Mesquita *et al.*, Direct measurement of tissue blood flow and metabolism with diffuse optics. *Philos Trans A Math Phys Eng Sci* **369**, 4390-4406 (2011).
124. T. Durduran, A. G. Yodh, Diffuse correlation spectroscopy for non-invasive, micro-vascular cerebral blood flow measurement. *Neuroimage* **85 Pt 1**, 51-63 (2014).
125. T. Durduran *et al.*, Diffuse optical measurement of blood flow in breast tumors. *Opt Lett* **30**, 2915-2917 (2005).
126. C. Zhou *et al.*, Diffuse optical monitoring of blood flow and oxygenation in human breast cancer during early stages of neoadjuvant chemotherapy. *J Biomed Opt* **12**, 051903 (2007).
127. Y. Shang, T. B. Symons, T. Durduran, A. G. Yodh, G. Yu, Effects of muscle fiber motion on diffuse correlation spectroscopy blood flow measurements during exercise. *Biomed Opt Express* **1**, 500-511 (2010).
128. G. Yu *et al.*, Validation of diffuse correlation spectroscopy for muscle blood flow with concurrent arterial spin labeled perfusion MRI. *Opt Express* **15**, 1064-1075 (2007).
129. R. C. Mesquita *et al.*, Hemodynamic and metabolic diffuse optical monitoring in a mouse model of hindlimb ischemia. *Biomed Opt Express* **1**, 1173-1187 (2010).
130. M. N. Kim *et al.*, Noninvasive measurement of cerebral blood flow and blood oxygenation using near-infrared and diffuse correlation spectroscopies in critically brain-injured adults. *Neurocrit Care* **12**, 173-180 (2010).
131. T. Durduran *et al.*, Diffuse optical measurement of blood flow, blood oxygenation, and metabolism in a human brain during sensorimotor cortex activation. *Opt Lett* **29**, 1766-1768 (2004).
132. E. M. Buckley *et al.*, Cerebral hemodynamics in preterm infants during positional intervention measured with diffuse correlation spectroscopy and transcranial Doppler ultrasound. *Opt Express* **17**, 12571-12581 (2009).
133. T. Durduran *et al.*, Transcranial optical monitoring of cerebrovascular hemodynamics in acute stroke patients. *Opt Express* **17**, 3884-3902 (2009).
134. S. Cutini, F. Scarpa, P. Scatturin, R. Dell'Acqua, M. Zorzi, Number-space interactions in the human parietal cortex: Enlightening the SNARC effect with functional near-infrared spectroscopy. *Cereb Cortex* **24**, 444-451 (2014).
135. A. M. Chiarelli, A. Di Vacri, G. L. Romani, A. Merla, Fast optical signal in visual cortex: Improving detection by General Linear Convolution Model. *Neuroimage* **66C**, 194-202 (2012).
136. S. D. Power, T. H. Falk, T. Chau, Classification of prefrontal activity due to mental arithmetic and music imagery using hidden Markov models and frequency domain near-infrared spectroscopy. *J Neural Eng* **7**, 26002 (2010).
137. S. P. Koch, J. Steinbrink, A. Villringer, H. Obrig, Synchronization between background activity and visually evoked potential is not mirrored by focal hyperoxygenation:

implications for the interpretation of vascular brain imaging. *J Neurosci* **26**, 4940-4948 (2006).
138. K. A. Low, E. Leaver, A. F. Kramer, M. Fabiani, G. Gratton, Fast optical imaging of frontal cortex during active and passive oddball tasks. *Psychophysiology* **43**, 127-136 (2006).
139. K. Schatzel, Accuracy of photon correlation measurements on nonergodic samples. *Appl Opt* **32**, 3880-3885 (1993).
140. M. S. Patterson, S. Andersson-Engels, B. C. Wilson, E. K. Osei, Absorption spectroscopy in tissue-simulating materials: a theoretical and experimental study of photon paths. *Applied optics* **34**, 22-30 (1995).
141. A. P. Gibson, J. C. Hebden, S. R. Arridge, Recent advances in diffuse optical imaging. *Phys Med Biol* **50**, R1-43 (2005).
142. U. Utzinger, R. R. Richards-Kortum, Fiber optic probes for biomedical optical spectroscopy. *J Biomed Opt* **8**, 121-147 (2003).
143. M. N. Helmus, D. F. Gibbons, D. Cebon, Biocompatibility: meeting a key functional requirement of next-generation medical devices. *Toxicol Pathol* **36**, 70-80 (2008).
144. R. J. Coffey, K. Miesel, T. Billstrom, Cerebrospinal fluid pressure measurement in the ovine intrathecal space: a preliminary study towards the diagnosis of intrathecal drug administration catheter dislodgement or occlusion. *Stereotact Funct Neurosurg* **88**, 337-344 (2010).
145. H. Ture *et al.*, Histopathological effects on epidural tissue of bolus or continuous infusions through an epidural catheter in ewes. *Anaesthesia* **65**, 473-477 (2010).
146. T. L. Gradert *et al.*, Safety of chronic intrathecal morphine infusion in a sheep model. *Anesthesiology* **99**, 188-198 (2003).
147. A. Ishikawa *et al.*, Epidural cooling minimizes spinal cord injury after aortic cross-clamping through induction of nitric oxide synthase. *Anesthesiology* **111**, 818-825 (2009).
148. A. Mori *et al.*, An epidural cooling catheter protects the spinal cord against ischemic injury in pigs. *Ann Thorac Surg* **80**, 1829-1833 (2005).
149. C. M. Bernards *et al.*, Epidural, cerebrospinal fluid, and plasma pharmacokinetics of epidural opioids (part 2): effect of epinephrine. *Anesthesiology* **99**, 466-475 (2003).
150. J. T. Strauch, A. Lauten, N. Zhang, T. Wahlers, R. B. Griepp, Anatomy of spinal cord blood supply in the pig. *Ann Thorac Surg* **83**, 2130-2134 (2007).
151. H. J. Wilke, A. Kettler, K. H. Wenger, L. E. Claes, Anatomy of the sheep spine and its comparison to the human spine. *Anat Rec* **247**, 542-555 (1997).
152. S. R. Sheng, X. Y. Wang, H. Z. Xu, G. Q. Zhu, Y. F. Zhou, Anatomy of large animal spines and its comparison to the human spine: a systematic review. *Eur Spine J* **19**, 46-56 (2010).
153. B. J. Kaplan, W. A. Friedman, N. Gravenstein, R. Richards, R. F. Davis, Effects of aortic occlusion on regional spinal cord blood flow and somatosensory evoked potentials in sheep. *Neurosurgery* **21**, 668-675 (1987).
154. R. M. Moomiaie *et al.*, Cooling catheter for spinal cord preservation in thoracic aortic surgery. *J Cardiovasc Surg (Torino)* **48**, 103-108 (2007).
155. J. D. Yeo, W. Payne, B. Hinwood, A. D. Kidman, The experimental contusion injury of the spinal cord in sheep. *Paraplegia* **12**, 279-298 (1975).

156. M. Meuli *et al.*, Creation of myelomeningocele in utero: a model of functional damage from spinal cord exposure in fetal sheep. *J Pediatr Surg* **30**, 1028-1032; discussion 1032-1023 (1995).
157. D. Bockler *et al.*, Spinal cord ischemia after endovascular repair of the descending thoracic aorta in a sheep model. *Eur J Vasc Endovasc Surg* **34**, 461-469 (2007).
158. S. Izumi *et al.*, Augmentation of systemic blood pressure during spinal cord ischemia to prevent postoperative paraplegia after aortic surgery in a rabbit model. *The Journal of thoracic and cardiovascular surgery* **139**, 1261-1268 (2010).
159. A. Agnoli, C. Fieschi, L. Bozzao, N. Battistini, M. Prencipe, Autoregulation of cerebral blood flow. Studies during drug-induced hypertension in normal subjects and in patients with cerebral vascular diseases. *Circulation* **38**, 800-812 (1968).
160. R. Zhang *et al.*, Autonomic neural control of dynamic cerebral autoregulation in humans. *Circulation* **106**, 1814-1820 (2002).
161. R. Hickey, M. S. Albin, L. Bunegin, J. Gelineau, Autoregulation of spinal cord blood flow: is the cord a microcosm of the brain? *Stroke* **17**, 1183-1189 (1986).
162. N. L. Martirosyan *et al.*, Blood supply and vascular reactivity of the spinal cord under normal and pathological conditions. *Journal of neurosurgery. Spine* **15**, 238-251 (2011).
163. L. A. Gillilan, The arterial blood supply of the human spinal cord. *The Journal of comparative neurology* **110**, 75-103 (1958).
164. M. J. Jacobs *et al.*, Spinal cord blood supply in patients with thoracoabdominal aortic aneurysms. *Journal of vascular surgery* **35**, 30-37 (2002).
165. M. A. Heymann, B. D. Payne, J. I. Hoffman, A. M. Rudolph, Blood flow measurements with radionuclide-labeled particles. *Prog Cardiovasc Dis* **20**, 55-79 (1977).
166. C. P. Reinhardt, S. Dalhberg, M. A. Tries, R. Marcel, J. A. Leppo, Stable labeled microspheres to measure perfusion: validation of a neutron activation assay technique. *Am J Physiol Heart Circ Physiol* **280**, H108-116 (2001).
167. E. J. Dolan, E. E. Transfeldt, C. H. Tator, E. H. Simmons, K. F. Hughes, The effect of spinal distraction on regional spinal cord blood flow in cats. *J Neurosurg* **53**, 756-764 (1980).
168. S. A. Meylaerts, M. J. Jacobs, V. van Iterson, P. De Haan, C. J. Kalkman, Comparison of transcranial motor evoked potentials and somatosensory evoked potentials during thoracoabdominal aortic aneurysm repair. *Ann Surg* **230**, 742-749 (1999).
169. M. R. Nuwer, E. Dawson, Intraoperative evoked potential monitoring of the spinal cord: enhanced stability of cortical recordings. *Electroencephalogr Clin Neurophysiol* **59**, 318-327 (1984).
170. E. B. Griepp *et al.*, The anatomy of the spinal cord collateral circulation. *Ann Cardiothorac Surg* **1**, 350-357 (2012).
171. E. B. Griepp *et al.*, The anatomy of the spinal cord collateral circulation. *Annals of cardiothoracic surgery* **1**, 350-357 (2012).
172. M. Elia, A. Kurpad, What is the blood flow to resting human muscle? *Clin Sci (Lond)* **84**, 559-563 (1993).
173. J. M. Bland, D. G. Altman, Statistical methods for assessing agreement between two methods of clinical measurement. *Lancet* **1**, 307-310 (1986).
174. D. C. Nieman, G. A. Trone, M. D. Austin, A new handheld device for measuring resting metabolic rate and oxygen consumption. *J Am Diet Assoc* **103**, 588-592 (2003).

175. J. M. Bland, D. G. Altman, Agreement between methods of measurement with multiple observations per individual. *Journal of biopharmaceutical statistics* **17**, 571-582 (2007).
176. T. J. Carroll *et al.*, Absolute quantification of cerebral blood flow with magnetic resonance, reproducibility of the method, and comparison with H2(15)O positron emission tomography. *J Cereb Blood Flow Metab* **22**, 1149-1156 (2002).
177. P. G. Popovich *et al.*, A reassessment of a classic neuroprotective combination therapy for spinal cord injured rats: LPS/pregnenolone/indomethacin. *Exp Neurol* **233**, 677-685 (2012).
178. V. J. Devlin, D. M. Schwartz, Intraoperative neurophysiologic monitoring during spinal surgery. *J Am Acad Orthop Surg* **15**, 549-560 (2007).
179. P. de Haan, C. J. Kalkman, Spinal cord monitoring: somatosensory- and motor-evoked potentials. *Anesthesiol Clin North America* **19**, 923-945 (2001).
180. D. A. Raw, J. K. Beattie, J. M. Hunter, Anaesthesia for spinal surgery in adults. *Br J Anaesth* **91**, 886-904 (2003).
181. K. Keyhani *et al.*, Analysis of motor and somatosensory evoked potentials during thoracic and thoracoabdominal aortic aneurysm repair. *Journal of vascular surgery* **49**, 36-41 (2009).
182. M. R. Nuwer, E. G. Dawson, L. G. Carlson, L. E. Kanim, J. E. Sherman, Somatosensory evoked potential spinal cord monitoring reduces neurologic deficits after scoliosis surgery: results of a large multicenter survey. *Electroencephalography and clinical neurophysiology* **96**, 6-11 (1995).
183. M. R. Nuwer *et al.*, Evidence-based guideline update: intraoperative spinal monitoring with somatosensory and transcranial electrical motor evoked potentials*. *Journal of clinical neurophysiology : official publication of the American Electroencephalographic Society* **29**, 101-108 (2012).
184. M. Seyal, B. Mull, Mechanisms of signal change during intraoperative somatosensory evoked potential monitoring of the spinal cord. *Journal of clinical neurophysiology : official publication of the American Electroencephalographic Society* **19**, 409-415 (2002).
185. M. Kakinohana *et al.*, Delayed response of transcranial myogenic motor-evoked potential monitoring to spinal cord ischemia during repair surgery for descending thoracic aortic aneurysm. *Journal of anesthesia* **22**, 304-307 (2008).
186. J. Hofmeijer, H. Franssen, L. J. van Schelven, M. J. van Putten, Why are sensory axons more vulnerable for ischemia than motor axons? *PloS one* **8**, e67113 (2013).
187. D. B. Macdonald, Intraoperative motor evoked potential monitoring: overview and update. *J Clin Monit Comput* **20**, 347-377 (2006).
188. D. M. Schwartz *et al.*, Neurophysiological detection of impending spinal cord injury during scoliosis surgery. *J Bone Joint Surg Am* **89**, 2440-2449 (2007).
189. D. D. Langeloo, A. Lelivelt, H. Louis Journee, R. Slappendel, M. de Kleuver, Transcranial electrical motor-evoked potential monitoring during surgery for spinal deformity: a study of 145 patients. *Spine* **28**, 1043-1050 (2003).